Karlsruher Institut für Technologie

DEVELOPMENT OF A MICROFLUIDIC PLATFORM FOR NMR ANALYSIS OF BIOLOGICAL SAMPLES

Nurdiana Binti Nordin

INSTITUTE OF MICROSTRUCTURE TECHNOLOGY

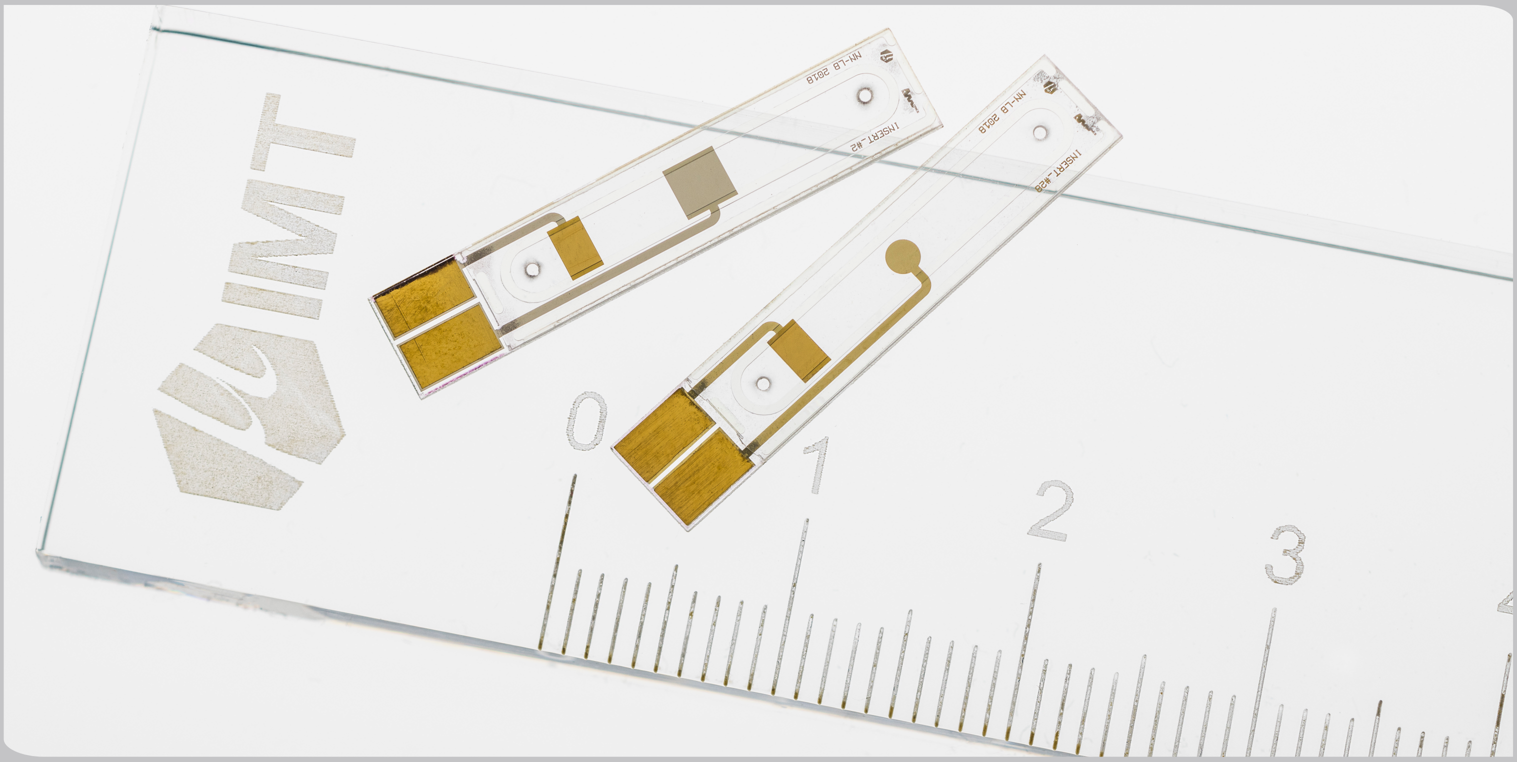
IMT
NM-LB 2018
INSERT_#2
INSERT_#20
0
1
2
3

Karlsruhe Institute of Technology

DEVELOPMENT OF A MICROFLUIDIC PLATFORM FOR NMR ANALYSIS OF BIOLOGICAL SAMPLES

Zur Erlangung des akademischen Grades einer

DOKTORIN DER INGENIEURWISSENSCHAFTEN
(Dr.-Ing.)

von der KIT-Fakultät für Maschinenbau des
Karlsruher Instituts für Technologie (KIT)
genehmigte

DISSERTATION

von

M.Sc., NURDIANA BINTI NORDIN

Tag der mündlichen Prüfung: 19.10.2020
Hauptreferent: Prof. Jan G. Korvink
Korreferentin: Prof. Christina Thiele

This document is licensed under a Creative Commons
Attribution-ShareAlike 4.0 International License (CC BY-SA 4.0):
https://creativecommons.org/licenses/by-sa/4.0/deed.en

Karlsruher Institut für Technologie
Institut für Mikrostrukturtechnik
Hermann.-v.-Helmholtz Platz 1 76344
Eggenstein-Leopoldshafen

I hereby declare that I write this work independently and that I do not use any sources other than those specified, that I have identified the literal or substantive accepted passages as such and the statutes of the Karlsruhe Institute of Technology for the protection of good scientific practice, as amended heeded.

Hiermit versichere ich, dass ich diese Arbeit selbständig verfasst und keine anderen, als die angegebenen Quellen und Hilfsmittel benutzt, die wörtlich oder inhaltlich übernommenen Stellen als solche kenntlich gemacht und die Satzung des Karlsruher Instituts für Technologie zur Sicherung guter wissenschaftlicher Praxis in der jeweils gültigen Fassung beachtet habe.

Ort, den Datum

بسم الله الرحمن الرحيم

In the name of God, most Gracious, most Compassionate

Dedicated to the loving memory
of my very dear late father,

***Nordin B. Mohd Saat**. . .*

Contents

Zusammenfassung i

Abstract iii

1 Introduction 1

1.1 Motivation 1

1.2 Literature Review 5

1.2.1 NMR Miniaturisation 5

1.2.2 Microfluidic platform compatible with a NMR microdetector 7

1.2.3 Potential Substrate for immobilisation of biological samples 8

1.2.4 Concept and Experimental Approach 11

2 Fundamentals of NMR 13

2.1 Recycle delay (d1) 13

2.2 Shimming, line widths, and line shapes 14

2.3 Sources of NMR line broadening 15

2.4 Homogeneous broadening 16

2.5 Inhomogeneous broadening 17

2.5.1 Magnetic field inhomogeneities / magnetic field gradients 18

2.5.2 Powder average broadening 18

2.5.3 Magnetic susceptibility discontinuities 18

2.6 Signal-to-noise measurements 20

2.7 Integration 22

3 Materials and Methods 23

3.1 Fabrication Process 23

3.1.1 Electrode array microfabrication 24

3.1.2 Planar electrode inside microfluidic channel compatible with the NMR microdetector 26

3.1.3 Sidewall electrode inside microfluidic channel compatible with the NMR microdetector 27
3.2 Substrate Characterization 30
3.2.1 Materials 30
3.2.2 Chitosan characterization 30
3.2.3 Modification of chitosan 30
3.2.4 Visualisation of chitosan 31
3.3 Electrodeposition (ED) of Chitosan 33
3.3.1 Setup experiment for in situ ED 33
3.3.2 NMR Data Acquisition 34
3.3.3 Nutation and MRI Experiments 36
3.3.4 NMR procedure for in situ ED 37
3.4 Application of the system: Determination of the function of enzymes 37
3.4.1 Preparation of enzymes towards substrates 37
3.4.2 Real-Time NMR Measurements 41
3.4.3 Calculation of the enzyme units when determining enzymatic activity 42

4 Result and Discussion **45**
4.1 Concept of fabrication design 45
4.2 Electrode array microfabrication 46
4.2.1 Sequential ED of Chitosan 46
4.3 Integrating with Helmholtz NMR microdetector 56
4.3.1 Criteria for the position of the working electrodes 57
4.3.2 Thickness of electrodes 60
4.3.3 Nutation experiment 61
4.3.4 MRI Imaging for B_1 and B_0 field Homogeneity 64
4.3.5 T_1 Relaxation NMR 65
4.3.6 Sensitivity 67
4.4 Monitoring in situ electrodeposition by NMR 68
4.5 Sequential ED of CS-QD for two configurations: Identifying the thickness of the hydrogel 74
4.5.1 Planar electrodes 74
4.5.2 Sidewall electrodes 74
4.6 Application: Determining the function of enzymes 76

4.6.1 History of urease (Urs) and Glucose Oxidase (GOx) . . . 77
4.6.2 Coupling CSPEG to Urs and GOx 79
4.6.3 Monitoring activity in situ first layer of CSPEG-Urs . . . 81
4.6.4 Monitoring activity of in situ of CSPEG-GOx 82
4.6.5 Monitoring activities in situ multi-layers of CSPEG-Urs, CSPEG-cat and CSPEG-GOx 85
4.6.6 Extraction of enzymes activity by using Michaelis-Menten equation 86
4.6.7 **Saddle coil** versus microdetector **Helmholtz coil** . . . 101

5 General Conclusion 105
5.1 Miniaturisation of a chitosan electrodeposition setup 105
5.2 Immobilisation of biological samples 105
5.3 Towards application in metabolomics 106

6 Limitation and Future Prospect 107
6.1 Limitation known issues affecting the ED platform 107
6.2 Known issues affecting the electrodeposited gel 108
6.3 Future Work 109

Appendices 125

A Potentiometric Titration. 127

B NMR spectroscopy. 129

C Fluorescence spectroscopy & Fluorescence microscopy 135

D Monitoring in real-time NMR 137
D.1 Measurement using Bruker's Micro 5 137
D.2 Measurement using a custom Helmholtz coil microdetector, NMR 142

E Estimation volume of hydrogels 147

Publications 149

Conferences 151

Activities 153

Acknowledgements **155**

List of abbreviations

1D	One-dimensional
2D	Two-dimensional
Au	Gold
Cat	Catalase
CdTe	Cadmium telluride
Cr	Chromium
CSI	Chemical shift imaging
CS	Chitosan
CSPEG	Chitosan coupled to PEG
CSPEG-PAMAM	CSPEG coupled to Pamam polymer
CSPEG-QD	CSPEG coupled to quantum dots
CSPEG-cat	CSPEG coupled to catalase
CSPEG-GOx	CSPEG coupled to GOx
CSPEG-Urs	CSPEG coupled to urease
Cu	Copper
CuSO4	Copper sulphate
DCl	Deuterium chloride
DIW	Deionized water
EDC	N-(3-Dimethylaminopropyl)-N′-ethylcarbodiimide hydrochloride
FA	Flip angle
FFT	Fast Fourier transform
FID	Free induction decay
FOV	Field of view
FWHM	Full-Width Half-Maximum
GOx	Glucose Oxidase
HCl	Hydrochloric acid
HH	Helmholtz coil
HMDS	hexamethyldisiloxane
IPA	Isopropanol

KOH	Potassium hydroxide
LOD	Limit of detection
MEMS	Micro electro-mechanical system
microTAS	Micro total analysis science
MR	Magnetic resonance
MRI	Magnetic resonance imaging
MW	Molecular weight
NaAc	Sodium acetate
NaOD	Sodium deuterium oxide
NaOH	Sodium hydroxide
NHS	N-hydroxysuccinimide
NHS-Fl	N-hydroxysuccinimide fluorescein
NMR	Nuclear magnetic resonance
PAMAM	Polyamidoamine dendrimers
PBS	Phosphate buffer solution
PCB	Printed circuit board
PDMS	polydimethylsiloxane
PE	polyethylene
PEB	Post exposure bake
PEG	Polyethylene glycol
PET	Polyethylene terephthalate
PGMEA	Propylene glycol monomethyl ether acetate
PLB	Post lamination bake
PMMA	Polymethyl methacrylate
ppm	Part per million
PU	Polyurethane
QD	Quantum dots
RF	Radio frequency
Si	Silicon
SNR	Signal-to-noise-ratio
TA	Total acquisition time
TR	Repetition time
TSP	Trimethysilyl propanoic acid
UV	Ultraviolet
zg	Zero Go

List of symbols

J	Current density
[ ]	concentration
µL	microlitre
µm	micrometre
nL	nanolitre
A/m^2	Ampere per square meter
a.u	Arbitrary unit
Å	angstrom
B_0	main magnetic field
B_1	radiofrequency field
K_M	substrate concentration at which the reaction rate is half of its maximal value
V_i	Initial rate of reaction
$V_{\max}$	Maximum rate of reaction
S_o	Initial concentration of substrate/product
S_{inf}	Final concentration of substrate/product
T_1	Spin-lattice (longitudinal relaxation time
T_2	Spin-spin (transverse) relaxation time
T_0	Initial time
T_f	Final time
mM/min	Millimolar per minute
µM/min	Micromolar per minute

List of Tables

3.1 Molar ratios of chitosan, PEG, and PAMAM (CS:PEG:PAMAM) 31

4.1 Molar ratios of CS, PEG, and PAMAM (CS:PEG:PAMAM) . . 52

4.2 Summary of the NMR/MRI figures of merit for performance evaluation of different inserts. 67

4.3 Summary of the kinetic activity of **Urease** using the micro-detector Helmholtz coil. *Note: The reaction of the GOx enzyme is always linked to its co-enzyme, catalase, in a 4:1 ratio. 90

4.4 Summary of the kinetic activity of **Glucose Oxidase** using the micro-detector Helmholtz coil.*Note: The reaction of the GOx enzyme is always linked to its co-enzyme, catalase, in a 4:1 ratio. 94

4.5 Summary of the kinetic activity of the multi-layered enzymes using two different geometries, planar and sidewall electrodes. Substrate solution composition was 1000 mM urea, 100 mM D-glucose (200 mM NaAc, pH 7 + 50 mM TSP) in each case. Each row reports the extracted data for the enzyme highlighted in **bold**. *Note: GOx is always prepared together with catalase in a 4:1 ratio. 100

4.6 Summary of the kinetic activity of **Urease** and **Glucose Oxidase** using using the commercial saddle coil. Kinetic parameters were extracted by fitting the consumption of urea and the production of D-gluconic acid, respectively. *Note: The reaction of the GOx enzyme is always linked to its co-enzyme, catalase, in a 4:1 ratio. 102

List of Figures

1.1 Protein Data Bank (PDB) Statistics. 2
1.2 Protein Data Bank (PDB) Statistics from NMR. 3
1.3 Chitosan electrodeposition schematic. 9
1.4 Conceptual schematics of the microfluidic for the biological samples in NMR. 11

2.1 Nuclear magnetization evolution after an RF pulse. 14
2.2 Lorentz bell curve. 15
2.3 Sources of inhomogeneous broadening. 19

3.1 Electrode array fabrication process. Each gold working electrode covers a nominal area of 1.76 mm^2 24
3.2 Planar electrodes fabrication process. 28
3.3 Sidewall electrodes fabrication process. 29
3.4 Reaction scheme for the chitosan+PEG modifications described in this work. 30
3.5 Reaction scheme for the CS-PEG+PAMAM dendrimer modifications described in this work. 31
3.6 Quantum dot labelling of chitosan polymer. 32
3.7 Experimental setup for in-situ electrodeposition. 35

4.1 Electrodes array platform. 47
4.2 Control of chitosan electrodeposition by profilometry and fluorescence imaging. 48
4.3 ^{1}H NMR spectrum of chitosan, with 75% deacetylation 49
4.4 ^{1}H NMR spectra of chitosan and its modifications 50
4.5 Titration of CS pre- and post-modification 51
4.6 Fluorescence spectra of coupled QD. 53
4.7 Schematic illustration of relevant terms entering equation 4.3 . . 54
4.8 Modified chitosan electrodeposition on an electrode array in the closed configuration. 55

4.9 Electrodeposition sample insert designs. 58
4.10 Thickness of planar working electrode. 59
4.11 Thickness of sidewall electrodes. 61
4.12 Electrodeposition platform for *in situ* NMR monitoring experiments. 62
4.13 Nutation spectra of chitosan with and without electrodes in detector. 63
4.14 B_1 field maps. 64
4.15 T_1 relaxation measurement 66
4.16 ^{1}H NMR of sucrose for five different configurations 69
4.17 NMR experiment timing diagram 70
4.18 ^{1}H NMR of sequential electrodeposition of CS and its modifications. 71
4.19 Information data from the spectra collected for in situ electrodeposition of CSPEG. 72
4.20 B_1 and B_0 field lines in different electrodes configurations 73
4.21 Sequential deposition of CS-QD and gel height estimation in the case of a planar electrode. 75
4.22 Sequential deposition of CS-QD and gel height estimation in the case of sidewall electrodes. 76
4.23 A setup for the multiplex reaction. 77
4.24 Hydrolysis of urea to yield ammonia and carbonic acid. 78
4.25 Dissociation of carbonic acid proton and the equilibration of protonated ammonia and water. 78
4.26 Representation of hydrolysis of urea to yield ammonia and carbonic acid. 78
4.27 UV absorption spectra of Urs and GOx. 80
4.28 NMR results of urea depletion from urease with and without CS polymer. 82
4.29 pH calibration for enzymatic reactions with and without polymer 83
4.30 Concentration time series for D-Glucose and D-Gluconic acid during reaction with GOx. 83
4.31 Multi-layer hydrogel and Urs + GOx reaction monitoring on a planar electrode. 86
4.32 Multi-layer hydrogel and Urs+GOx reaction monitoring on a sidewall electrode. 97

4.33 Fraction of active units for two different enzymes using two different NMR detectors, Bruker's Micro 5 and a custom Helmholtz microcoil 104

A.1 Titration of pre and post-modified CS 128

B.1 ^{1}H NMR spectrum of CS-PEG-PAMAM (molar ratio 1:1:1) . . . 130
B.2 ^{1}H NMR spectrum of CS-PEG-PAMAM (molar ratio 1:2:2) . . . 131
B.3 ^{1}H NMR spectrum of CS-PEG-PAMAM (molar ratio 1:1:0.5) . . 132
B.4 ^{1}H NMR spectrum of CS-PEG-PAMAM (molar ratio 1:1:2) . . . 133
B.5 ^{1}H NMR spectrum of CS-PEG-PAMAM (molar ratio 1:0.5:0.5) . 134

C.1 Fluorescence emission spectra of Quantum dots (QDs) 135
C.2 Fluorescence emission profiles of multi-layered CS 136

D.1 ^{1}H NMR spectra of 1000 mM of urea using Bruker's Micro 5 . . 137
D.2 ^{1}H NMR spectra of the reaction of Urs + Urea using using Bruker's Micro 5 138
D.3 ^{1}H NMR spectra of 100 mM of D-Glucose using Bruker's Micro 5 138
D.4 ^{1}H NMR spectra of the reaction of GOx + D-Glucose using Bruker's Micro 5 139
D.5 ^{1}H NMR spectra of the reaction of GOx with polymer, CSPEG + D-Glucose using Bruker's Micro 5 139
D.6 ^{1}H NMR spectra of 100 mM of D-Glucose + 1000 mM of Urea using Bruker's Micro 5 140
D.7 ^{1}H NMR spectra of the reaction of multiplex Urs/GOx + urea/D-Glucose using Bruker's Micro 5 140
D.8 ^{1}H NMR spectra of the reaction of multiplex CSPEG-Urs/CSPEG-GOx + urea/D-Glucose using Bruker's Micro 5 141
D.9 ^{1}H NMR spectra of 1000 mM of urea using custom Helmholtz detector 142
D.10 ^{1}H NMR spectra of the reaction of Urs + Urea using using custom Helmholtz detector 142
D.11 ^{1}H NMR spectra of 100 mM of D-Glucose using Bruker's Micro 5 143
D.12 ^{1}H NMR spectra of the reaction of GOx + D-Glucose using custom Helmholtz microdetector 143
D.13 ^{1}H NMR spectra of D-Glucose + Urea using custom Helmholtz microdetector 144

D.14 ^{1}H NMR spectra of the reaction of multiplex Urs/GOx + urea/D-Glucose using custom Helmholtz microdetector 144
D.15 ^{1}H NMR spectra of the reaction of multiplex CSPEG-Urs/CSPEG-GOx + urea/D-Glucose using custom Helmholtz microdetector . 145

E.1 Schematic of the hydrogel layers for individual enzyme deposition and multiplex deposition conditions using (a) planar electrode geometry and (b) sidewall electrode geometry 147

Entwicklung einer mikrofluidischen Plattform für die NMR-analyse von biologischen Proben

Zusammenfassung

In dieser Arbeit wird die Entwicklung einer mikrofluidischen Plattform für die galvanische Abscheidung von Chitosan-Hydrogel vorgestellt. Die Plattform ist kompatibel mit einem NMR-Mikrodetektor, einer Helmholtz-NMR-Mikrospule, und war für die Bestimmung der Funktion verschiedener Enzyme in Echtzeit vorgesehen. Die experimentellen Verfahren wurden ausführlich beschrieben, einschließlich der Herstellung des mit verschiedenen Elektrodengeometrien integrierten Mikrofluidikkanals, des Protokolls für die Vorbereitung der Vor- und Nachbearbeitung von Chitosan als Substrat, der Einrichtung der Elektroabscheidung von vor- und nachbearbeitetem Chitosan unter Verwendung der verschiedenen Elektrodenkonfigurationen und des Protokolls für die NMR-Analyse zur Überwachung der Funktion verschiedener immobilisierter Enzyme.

Der erste Teil der Dissertation stellt im Detail die Technologie hinter der Realisierung biofunktionaler Array-Sites mit programmierbarer Zusammensetzungskontrolle in allen drei räumlichen Dimensionen vor. Die Technologie basiert auf der sequentiellen galvanischen Abscheidung von Chitosan. Aufgrund des sequentiellen Charakters dieses Verfahrens kann jede Schicht einzeln chemisch funktionalisiert werden, während gleichzeitig eine molekulare Kommunikation zwischen den Schichten über das poröse Netzwerk im gesamten fertigen Komposit-Hydrogel ermöglicht wird.

Der zweite Teil der Arbeit befasst sich mit der Integration zusätzlicher Funktionalitäten in mikrofluidische Geräte, wobei die Aufrechterhaltung qualitativ hochwertiger NMR-Spektren eine große Herausforderung darstellt. Die entwickelte NMR-Plattform besteht aus einem Fluidikkanal mit verschiedenen Konfigurationen von integrierten Elektroden, die für die in-situ-Elektrodenabscheidung von vor- und nachmodifiziertem Chitosan verwendet wurden.

Schließlich wird im dritten Teil der Arbeit als Proof-of-Concept-Anwendung die Bestimmung der Funktion von immobilisierten Enzymen mit Hilfe der Elektroplattformen diskutiert. Drei Schichten Chitosan-Gel, gekoppelt an verschiedene Enzyme, wurden gestapelt; anschließend wurde die Reaktion der Enzyme mit ihren jeweiligen Substraten in Echtzeit mit NMR überwacht. Die enzymatische Ak-

tivität wurde im Rahmen eines Michaelis-Menten-Modells analysiert.

Diese Plattform demonstriert die Fähigkeit der entwickelten Plattform, NMR-Analysen von bioaktiven komplexen Molekülen in einer kleinen Massenmenge durchzuführen, was neue Möglichkeiten für Fortgeschrittene Elektrochemie- und Metabolomikstudien eröffnet.

Development of a microfluidic platform for NMR analysis of biological samples

Abstract

This thesis presents the development of a microfluidic platform for electrodeposition of chitosan hydrogel. The platform is compatible with an NMR microdetector, a Helmholtz NMR micro-coil, and was intended for determining the function of various enzymes in real time. The experimental procedures have been described in detail, including the fabrication of the microfluidic channel integrated with different electrode geometries, the protocol for the preparation of pre- and post-processing of chitosan as a substrate, the setup of the electrodeposition of pre- and post-processed chitosan using the different electrode configurations and the protocol for NMR analysis to monitor the function of different immobilized enzymes.

The first part of the dissertation presents in detail the technology behind the realization of biofunctional array sites with programmable composition control in all three spatial dimensions. The technology is based on the sequential electrodeposition of chitosan. Due to the sequential nature of this process, each layer can be individually chemically functionalized, while at the same time allowing for molecular communication between the layers via the porous network throughout the completed composite hydrogel.

The second part of the thesis deals with the integration of additional functionalities into microfluidic devices, where the maintenance of high-quality NMR spectra is a major challenge. The developed NMR platform consists of a fluidic channel with different configurations of integrated electrodes, which were used for in situ electrode deposition of pre- and post-modified chitosan.

Finally, as a proof of concept application, the third part of the thesis discusses the determination of the function of immobilised enzymes using the electrodeposition platforms. Three layers of chitosan gel coupled to different enzymes were stacked; then the reaction of the enzymes with their respective substrates was monitored in real-time with NMR. The enzymatic activity was analysed in the framework of a Michaelis-Menten model.

This platform demonstrates the ability of the developed platform to perform NMR analysis of bioactive complex molecules in a small mass amount, opening

new opportunities in advanced electrochemistry and metabolomics studies.

Chapter 1

Introduction

1.1 Motivation

According to the Protein Data Bank (PDB)[1], as of 2020 more than 100 million unique protein sequences have been deposited (Figure 1.1) in the bank database. The volume of protein sequence information is increasing rapidly, creating a large gap between the total number of sequences stored in public databases and the number of structurally and functionally characterized proteins. The knowledge gap assumes even bigger proportions when one includes structural and/or functional changes of proteins that lead to dysfunctional signals, metabolism, etc. into the set of protein configurations that would be important from a medical standpoint. For example, a single amino acid substitution in an element of an isocitrate-dehydrogenase homodimer complex leads to a significant metabolic shift. The resulting altered metabolism is considered to be the cause of a class of gliomas[2, 3] and plays a role in leukaemia[4, 5]. Therefore, there is a critical need for a methodology that allows both structural and functional characterization of proteins. Closing the gap created by the availability of large quantities of raw data is a task that has been currently taken over by sophisticated calculation methods for protein function prediction[6]. Nevertheless, experimental high-throughput analysis, parallel and combinatorial protein analysis remain an under-developed potential complementary solution to this problem. In this thesis, we detail a solution for the immobilisation of biological samples on a suitable solid substrate viable for real-time, parallel analysis of protein function. To this end, we leverage microstructure technology for efficient sample handling and powerful analytical tools, such as the NMR spectroscopy, for precise investigation were presented.

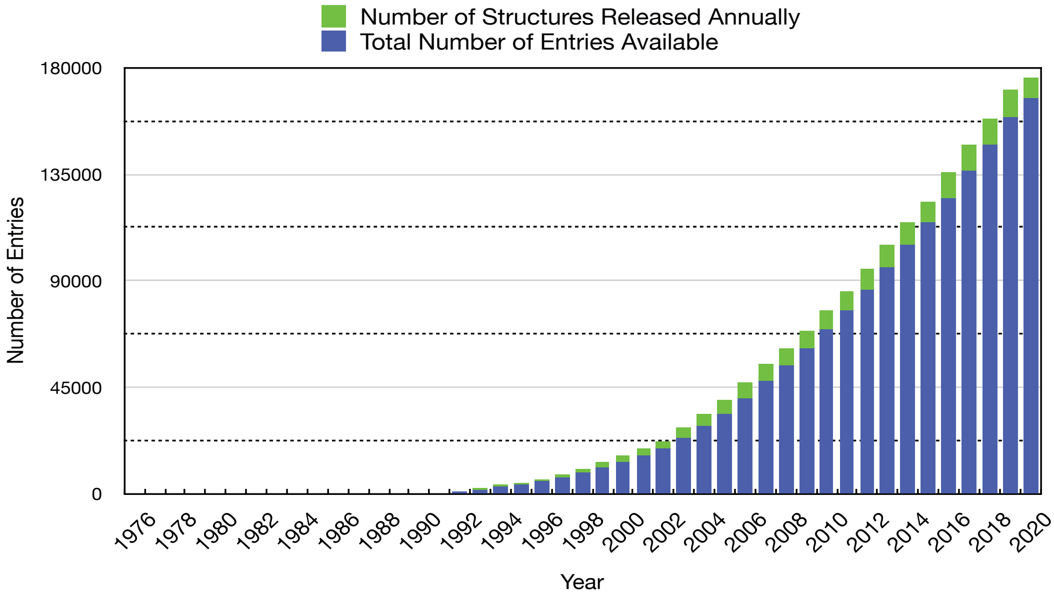

Figure 1.1 – PDB Statistics: Overall growth of released structures per year [1]

Nuclear Magnetic Resonance (NMR) has established itself as one of the methods of choice for determining the structure of proteins. NMR is a convenient method of investigation for biological systems, as it is non-destructive, intrinsically specific and universal. Advances in NMR spectroscopy, e.g. as an analytical tool for mapping complex biomolecular structures[7, 8] or for monitoring molecular dynamics[9, 10] have certainly boosted and promoted the growth of the protein research field.

NMR is also well suited for studies on protein function, where the word function is meant to refer to activity of a protein in the context of metabolic processes (as opposed to structural proteins, etc.). NMR spectral sensitivity to chemical structure allows to observe the transformation of a substrate into one or more products through enzymatic processes. NMR played a key role in the field of metabolomics where metabolite profiles are monitored for medical diagnosis, for example depending on the progression of a metabolic disease[11, 12]. This is possible because the onset of the disease is typically associated with the disruption of several metabolic pathways necessary to support the dysfunctional phenotype. One method of identifying the protein(s) involved in the metabolic dysfunction is to study the metabolite profile and map the pathways that may contribute to the observed up/down regulated metabolism. Given the large amount of both interconnecting metabolic pathways and proteins involved

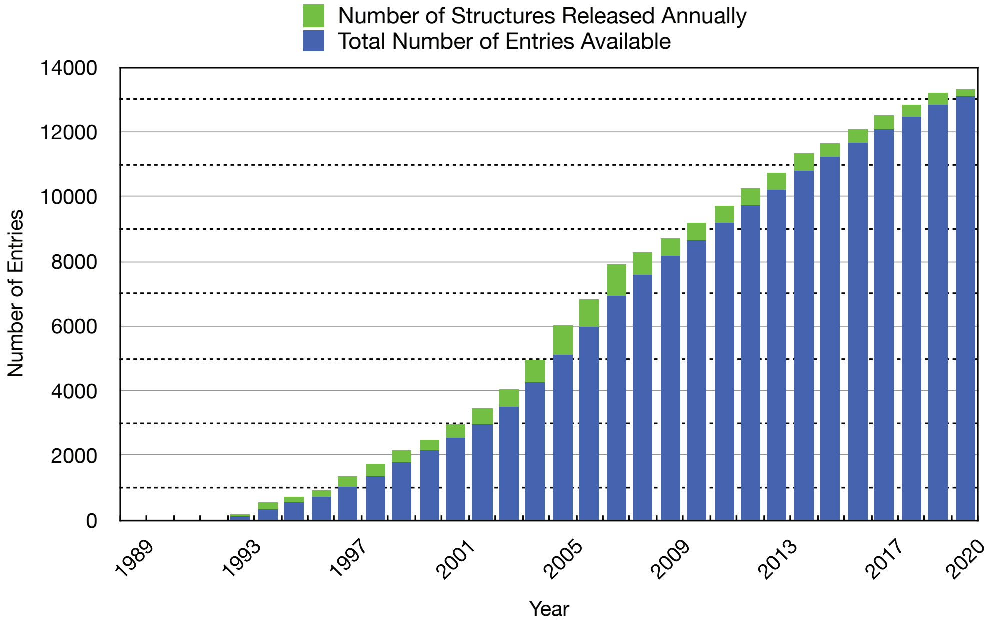

Figure 1.2 – PDB Statistics: Growth of structures from NMR experiments released per year [1]

therein, a systematic study of individual proteins identified in metabolite profile mapping and their functions as dependant on substrate, co-factors and potential treatment regimens is highly desirable. Such a study would help both in elucidating the mechanism of dysfunctions and in the intelligent design of therapies. The constraints of working at physiologically relevant concentration levels, short measurement times and small sample volumes for high-throughput studies put additional pressure on an analytical method (NMR) that, despite its versatility and specificity, is inherently insensitive. Figure 1.2 shows the statistics associated with the growing number of structures from NMR experiments published per year. Statistics show that the range of structures released per year is less than a thousand structures. However, the number of available entries (which can be examined by NMR spectroscopy) is more than ten thousand. Furthermore, the known protein functions are still far less than the number of known protein structures. Therefore, the question arises on how we can close this gap and at the same time improve the performance of NMR and thus increase the statistics of annually released structures/functions. As shown in this thesis, one way to address the problem is performing NMR on microscopic samples [13, 14].

To create a "biological environment" inside the magnet, a suitable platform compatible with the NMR microdetector is required. A standard NMR experiment requires a large amount of protein sample to obtain a good resolution of the NMR spectra. However, the extraction of proteins usually results in a small available amount for experiments, which leads to a low concentration of proteins that is difficult to detect under standard NMR experimental conditions. The development of a hydrogel-based immobilisation platform compatible with an NMR microdetector is expected to increase the mass sensitivity of NMR, since the hydrogel allows to increase the local concentration of interesting biological targets (e.g. proteins) in the active volume of the NMR sensor.

Out of the various classes of gels, hydrogels are particularly interesting from both a biological and technological perspective. Fundamentally, a hydrogel is a three-dimensional polymer network in which water fills the voids between the polymer chains. The polymer network, which may be the result of physically or chemically cross-linked polymer chains[15–18], is at least moderately hydrophilic in order to accommodate the high water content (in the range 85-90 wt %). Hydrogels may be classified on the basis of their constituent polymer origins. Naturally derived polymers capable of hydrogel formation include collagen and gelatine (protein-based), and polysaccharides including chitosan, alginate, and agarose. These polymers are particularly interesting due to their low toxicity, superior biocompatibility, and their ability to support cellular activities[19, 20]. Synthetically derived polymers are often synthesized from monomers including vinyl acetate, various acrylamides, ethylene glycol, and lactic acid. Synthetic polymers benefit from the tunability of hydrogel chemo-physical properties (e.g. stimuli responsiveness), often accomplished by tuning the composition of the synthesized polymer. Taking a hybrid approach, genetic engineering and biosynthetic methods have also been used to create unique hydrogel materials [21], [22]. Polymers of both natural and synthetic origins offer a chemical diversity that is directly reflected in the diversity of applications, the collection of which is in constant expansion[23].

Particularly interesting for the work presented in this thesis is the subclass of hydrogels that are capable of reversible gelation. In reversible hydrogels, the polymer network is maintained by physical interactions between polymer chains including van der Waals, electrostatic, and hydrogen bonding forces, the variety of which contribute to the large variety of gels belonging to this subclass[24]. Importantly, these interactions may be easily disrupted to form a homogeneous solution of individual polymer chains. Application of an appropriate stimulus drives either the sol-gel phase transition (cross-linking) or its reverse counter-part, the gel-sol phase transition (de-cross-linking). These transitions are often sensitive to even minute environmental changes in the appropriate stimulus and, as such, reversible hydrogels are often referred to as “smart” hydrogels[25]. A number of environmental stimuli are able to trigger the gel-sol phase transition, stemming from the variety of physical interactions available to, and dependent on, the chemical composition of the hydrogel. Stimuli include pH, temperature, ionic strength, solvent composition, pressure, electrical potential, radiation, and chemical and biological analytes. Reversible hydrogels may be classified according to sensitivity to a particular stimulus as photo-, chemo-, electro-, or mechano-sensitive[26–32]. Example applications of reversible hydrogels include smart films[33, 34], sensors[35, 36], electrooptic devices[37], microfluidic devices[38], pulsatile drug release or delivery systems[39–44], bio-adhesions mediators[45, 46], and actuators[47]. It is often assumed that stimulus changes occur in the bulk solution of the polymer, leading to a homogeneous phase transition to the hydrogel state[48]. Micro manufacturing technologies enable the precise design and implementation of local ”stimulus actuators” with functional resolutions down to sub-mm[49], thereby achieving fine spatial control of the sol-gel transition.

This work investigates the potential of combining reversible, biocompatible hydrogels with devices based on microelectrochemical systems (MEMS) technologies. First, a subset of polymers that meet the following requirements needs to be identified: **(i) hydrogel formation is possible; (ii) hydrogel formation is triggered by a controllable external stimulus; (iii) sol-gel transition is reversible; (iv) hydrogel is biocompatible.** Once the nature of the stimulus responsible for the sol-gel transition of selected biopolymers is known, a matching microtechnological solution such as microfluidic platform compatible with NMR microdetector is selected to provide such a stimulus.

1.2 Literature Review

1.2.1 NMR Miniaturisation

NMR is an analytical technique that has developed into a widespread research instrument covering all states of matter, a wide temperature ranges from sub-Kelvin to several hundred Kelvin and a multitude of applications in physics, chemistry, materials science, pharmacy, biology, medicine and technology. What makes NMR powerful is that nuclei are very sensitive probes of the local magnetic environment. Molecular processes mostly involve electrostatic forces and nuclear magnetism only constitutes a small perturbation. The energies involved in NMR are much lower than those involved in chemical bonding and chemical reactions, for instance[14]. That is why molecular processes are not disturbed by NMR or nuclear magnetism in general.

The NMR signal is detected by a voltage that is Faraday induced by the prepared nuclear magnetization of the sample in a radio frequency (RF) coil resonator. The NMR is sensitive to the number of spins. The fewer the number of spins, the less sensitive the NMR is. This is also expressed as differences in the ensemble population. The concentration of the sample determines the total population of spins, and the Boltzmann statistics determines the equilibrium population difference of the spins (parallel or antiparallel). However, the disadvantage of low sensitivity is significantly mitigated by downscaling the NMR detector to small target samples[50, 51]. A wide range of miniaturised designs with significant improvements in sensitivity have been reported. Magnetic microcoil detectors have become popular[52–54], taking advantage of the fact that the signal to noise ratio is inversely proportional to the size of the NMR detector[52–55]. For instance, the stripline probes for NMR[56–58] combine high mass sensitivity with low susceptibility broadening and high power efficiency in a simple geometry. A planar microslot waveguide NMR probe[59] reduces the required sample volume by several orders of magnitude while providing excellent sensitivity and spectral resolution.

The NMR microdetector that has been used extensively in this thesis is a microfabricated Helmholtz-pair coil. The Helmholtz topology offers a highly homogeneous RF field profile across the excitation volume covered by the coil[60]. The quality of the RF field homogeneity for a Helmholtz coil is comparable to that of solenoid, birdcage and saddle coil NMR detectors. However, the chosen geometry offers an outstanding compromise between tight control over homogeneous excitation of sub-volumes inside the detector and flexibility in the regular use of the detector itself. The fact that the two expansions of the Helmholtz pair are separated by a gap which is roughly as wide as one radius of the coil allows to easily position a specialised sample insert in-between the two expansions[61].

1.2.2 Microfluidic platform compatible with a NMR microdetector

The processing techniques and materials used to produce miniaturised sensors and systems for biological applications are very demanding and generally incompatible with the integration of sensitive biological components. Several materials and processes have been developed to facilitate the functionalisation of micro devices with biomolecules such as DNA, enzymes or antibodies that confer specificity and sensitivity. Polysaccharide hydrogels such as chitosan and alginate have recently been found to respond to stimuli such as chemical and pH gradients[62–65].

For polymer like chitosan, a current signal transmitted by an electrode determines a local pH increase and thus triggers a sol-gel transition of the chitosan close to the location of the stimulus. The thickness of the hydrogel deposition can be controlled by adjusting the current density. The limitation of the gel growth mainly depends on the layout and dimensions of the microfluidic system. [66].

The unique properties of the proposed method for immobilisation of biomolecules inside the volume of the NMR microdetector are:

- Hydrogel layer formation is controlled with high spatial-temporal resolution via electrical signals by addressable electrodes defined by UV lithography. The gel formation is a reversible mechanism, therefore the electrode used for deposition can be washed and reused.

- The target biomolecules can be mounted at predefined locations on the hydrogel assembly for precise investigation of complex interacting biosystems.

- Hydrogel formation and biomolecules arrangement can be performed in closed microfluidics, i.e. in the optimal detection range of already manufactured NMR detectors. This approach requires no exposed or plane surfaces, and no direct or visual access to the target site.

1.2.3 Potential Substrate for immobilisation of biological samples

Polymers with the ability to transition from a solution to hydrated gel state reversibly after application of a particular signal are highly attractive “intelligent” materials. Since the sol-gel transition stimulus can be localized in both space and time, many new opportunities arise in terms of, for example, chemical control. To determine suitability of a certain polymer for a specific application, these points are usually considered:

- Is biocompatibility essential?
- Is the stimulus necessary to drive the gelation detrimental to the application?
- Is there a need to chemically modify the resulting hydrogel?

In this thesis, we would like to draw attention to the ability to control the sol-gel transition through microtechnological approaches. This brings additional degrees of freedom to experimental control:

- The sol-gel phase transition can be triggered with high spatial precision. Standard photolithographic techniques can produce structures with feature sizes on the order of tens of micrometers.
- The phase transition can be triggered with high temporal precision. Since the size of the active structures is small, the hydrogel response is expected to be fast[67].
- Devices can be produced in an arrayed format. The small dimensions of the active structures mean several such structures can be produced in a single device. For example, a device consisting of active structures with diameter 500 µm spaced with a pitch of 500 µm will have 100 active structures within $1\,\mathrm{cm}^2$. In principle, each active element could control a unique experiment.

In order to guide the selection of an appropriate polymer, we have chosen a classification scheme based on water content, compliant elasticity, facile diffusion of biomacromolecules, physical and chemical crosslinking, proliferation and migration of encapsulated biomolecules.

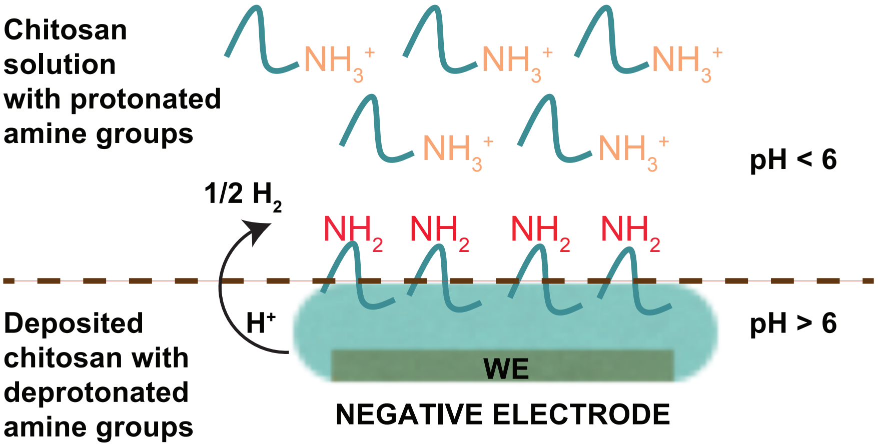
Chitosan solution with protonated amine groups
NH3+
NH3+
NH3+
NH3+
NH3+
pH < 6
1/2 H2
NH2
NH2
NH2
NH2
H+
Deposited chitosan with deprotonated amine groups
WE
NEGATIVE ELECTRODE
pH > 6

Figure 1.3 – The mechanism of electrodeposition of chitosan is illustrated.

pH sensitive polymers are normally produced by adding pendant acidic or basic functional groups to the polymer backbone[68]. There are three main categories of pH-responsive polymers; polyelectrolytes, cellulose esters and polyvinyl derivatives. In polyelectrolytes, the functional groups responsible for activity are either acidic (for example: carboxylic and sulfonic groups) or basic amino groups. Functional groups of carboxylic, sulfonate and primary or tertiary amino groups exhibit a change in ionization states as a function of pH. The behaviour of pH sensitive polymers upon changes in pH during a soluble-insoluble phase transition (for instance: swelling- shrinking changes or conformational changes) depend on the degree of the ionization of the ionizable groups in the polymer, on polymer compositions, on ionic strength and on the hydrophobicity of the polymer backbone[19, 20, 67, 69, 70].

Polysaccharide chitosan is a polyelectrolyte that undergoes pH-dependant hydrogel formation. When chitosan is immersed in an acidic solution, it experiences strong pH-dependent swelling[71, 72]. The plentiful hydrophilic functional groups (such as hydroxyl- and amino-) in the backbones of chitosan, qualify chitosan as promising material for highly absorbent hydrogels systems. Chitosan polymer is used in a variety of applications, including controlled drug release, scaffolds for tissue engineering and semipermeable membranes[73–79]. Nearly 10 years ago, chitosan was the first bio-polymer discovered to undergo electrodeposition by a cathodic neutralization mechanism[80–83]. Figure 1.3 illustrates the electrodeposition mechanism of chitosan. When current is applied, a cathode electrode (negative terminal) produces a local pH gradient which in turn neutralizes the acidic solution of chitosan, resulting in a neutral hydrogel on the surface of the electrode. The hydrogel can later be dissolved again with an acidic solution.

The biocompatible polysaccharide chitosan was chosen as the material to interface biological elements with the micro-scaled NMR instrumentation. The following unique properties of chitosan made it attractive for use within microfluidic devices:

1. **Chitosan has a pH-dependent solubility** and thus forms stable layers on different surfaces under neutral and basic pH conditions.
2. **Chitosan has amine groups** that are used for the covalent binding of biomolecules.
3. **Chitosan can be combined with biological samples**, e.g. with enzymes and proteins, due to its biocompatibility and ease of functionalisation.

Covalent binding is a robust method for binding biomolecules to the chitosan amine (NH_2) groups. Various chemicals are available for this purpose, such as glutaraldehyde and tyrinose. Glutaraldehyde has two reactive aldehyde groups at both ends of the molecule, which covalently bind to the amine groups of chitosan to form an imide bond, and to the biomolecules labelled with amines. Alternatively, if the biomolecules of interest are labelled with tyrosine, binding to chitosan can be achieved by activation with tyrosinase. The enzyme tyrosinase converts the tyrosine residue into a reactive o-quinone that binds to the chitosan amine groups[84–87]. The biomolecules of interest can either be covalently bound to chitosan after electrodeposition, which only leads to surface adhesion of biomolecules, or the biomolecules can be bound to the chitosan chains in solution followed by electrodeposition, whereby biomolecules are homogenously distributed throughout the entire bio-gel film volume.

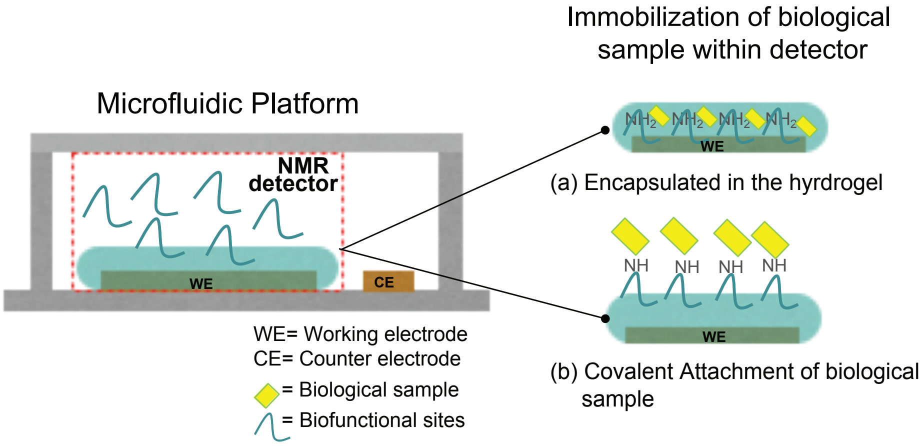
Microfluidic Platform
NMR detector
WE
CE
WE= Working electrode
CE= Counter electrode
= Biological sample
= Biofunctional sites
Immobilization of biological sample within detector
NH2 NH2 NH2 NH2
WE
(a) Encapsulated in the hyrdrogel
NH NH NH NH
WE
(b) Covalent Attachment of biological sample

Figure 1.4 – Conceptual schematics of the microfluidic for the biological samples in NMR. a) Side view of the proposed structure that links the microfluidic environment to the metallisation for NMR detection unit and spatial-temporal controllable protein electrode addressing. (a), the electrodes are connected via a covalent mounting of biological samples to the primary amine groups of the electrodeposited bio-functional sites backbone; (b) biological samples are embedded in the polysaccharide hydrogel film to subsequently perform NMR analyses in the biological samples.

1.2.4 Concept and Experimental Approach

This work addresses the **development of a robust tool that enables the NMR investigation of enzymes at work in a biocompatibility environment**. The main objective was to develop an environmental microfluidics platform that enables on-demand biological sample immobilisation with high spatial and temporal resolution at electro-addressable sites within the platform. The platform was integrated into a NMR microdetector for high-resolution investigation of the immobilised target at previously defined sites.

Figure 1.4 illustrates how the proposed goal can be achieved. In this work, a combination of bio- and micro-manufacturing techniques were used to develop a bioMEMS environmental platform, a miniaturized system with applicability to biological samples in NMR. This research was confronted with the challenge of integrating biological elements into miniaturised systems.

State-of-the-art results exemplify the combination of the top-down approaches specific to microfabrication with the bottom-up approach specific to the assembly of biological components, in the present case the electrodeposition of chitosan hydrogel[78, 88–91]. Metal electrodes integrated into the platform and defined using standard microfabrication techniques (such as: metallization, UV lithography, etching) provide the spatial resolution for subsequent bio-assembly. The electrical signals delivered via these electrodes promote the selective electrodeposition of hydrogels at precise locations within the platform. Biological samples are either covalently bound to amine groups or embedded into the hydrogel matrix by co-deposition. The primary amine of glucose amine residues gives chitosan its sought-after chemical properties. For the covalent binding of enzymes, the glucosamine residues represent the connection points to the chitosan skeleton. The nucleophilic properties of the amine groups enable covalent bonding over a broad spectrum of coupling chemicals. One of the main concerns when dealing with a biologically active molecule is the freedom of the molecule to tumble in solution. This is achieved by varying the linker length, e.g. by using a chemistry based on polyethylene glycol (PEG).

The designed platform takes into account the following necessities:

1. the hydrogel material must be placed in the active area of the NMR detector or directly close by
2. the analytes of interests must be able to reach the active regions (e.g. metabolic substrates)

In addition, the removal of carrier media and metabolic waste shall be taken into account. Since miniaturisation itself entails further design restrictions and design freedom in the micro range is significantly compromised, it was necessary to optimise these parameters with regard to the final goal of the platform: biological samples analysis by NMR. Taking all these limitations into account, a numerical optimisation of the device layout was performed. Particular attention was given to the magnetic susceptibility values of a relatively large number of different materials (structural materials of the platform, buffer media, samples) packed in the small volume of the biological environmental platform.

Chapter 2

Fundamentals of NMR

In this chapter, an introduction to the basic NMR concepts required for this thesis is provided. The implicit and functional concepts for the operation of a modern NMR spectrometer are described, if necessary, with generic illustrations.

2.1 Recycle delay (d1)

After the RF pulse, the nuclear spins do not instantly return to equilibrium; rather, they each relax according to a time constant called T_1 (longitudinal relaxation time, which parameterizes an approximation of the time necessary for the magnetization to recover along the z-axis). Individual T_1 time constants are dependent on many factors including nuclear environment, temperature, and solvent. T_1 times for carbon atoms are typically much longer than T_1 times for hydrogen atoms. Since each nucleus in a molecule is immersed in a different magnetic environment, their T_1 will not be the same. Not allowing enough time for relaxation between pulses will cause varied attenuation of the signals and inaccurate integration. When a 90° pulse is used to excite the spins (Figure 2.1a), a total time (TT) between pulses of $5 * T_1$ is necessary in order to have nearly complete relaxation. (z-magnetization $= 1 - e^{-\text{elapsed time}/T_1}$, where $1 - e^{-5} \simeq 0.99326$). If a pulse width less than 90° is used, the total time can be proportionally less, and intensity distortions due to relaxation effects can be minimized. This is one reason why the standard pulse width for ^{1}D ^{1}H NMR experiments are in the range of 25° to 45°.

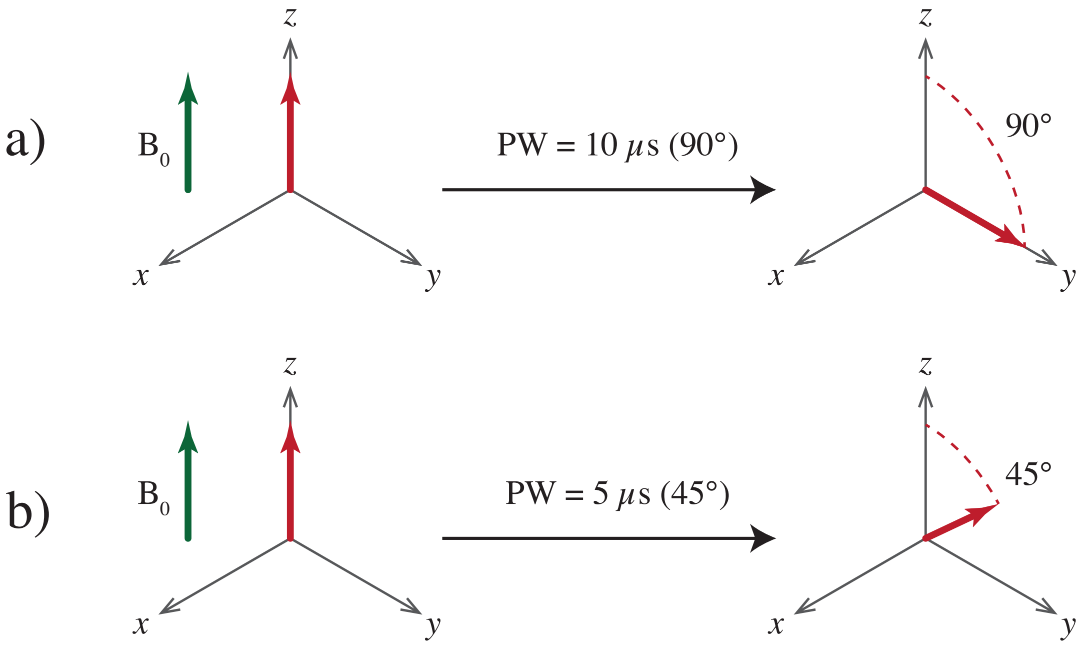

Figure 2.1 – The bulk nuclear spin magnetization (bold arrow) for an NMR sample placed in a magnetic field aligned along the z-axis before and after application of a pulse.

2.2 Shimming, line widths, and line shapes

In order to obtain the most homogeneous field possible over the sample, the pole faces of the magnet had to be perfectly aligned. To achieve this, small pieces of wood or ”shims” were hammered into the magnet holder to physically move the poles relative to each other. Today, shimming is achieved by changing the applied current for a specific set of coils surrounding the probe. This applied current generates small magnetic fields in the area of the probe, which either amplify or counteract the local gradient of the static magnetic field. The aim is to counteract small imperfections in an otherwise homogeneous magnetic field in order to obtain a magnetic field as homogeneous as possible over the sample, which is usually observed as an increase in FID length.

NMR peaks have a shape that is called Lorentzian. A Lorentzian line can be expressed mathematically with three parameters: amplitude $[A]$, full width at half height in Hz $[\mathrm{LW}_{1/2}]$ and centreline position, in Hz $[X_0]$. An example of a Lorentzian line with $\mathrm{LW}_{1/2} = 0.25\,\mathrm{Hz}$ is shown in Figure 2.2.

From the mathematical equation for a Lorentzian line (see Figure 2.2), the line width at 0.55% height is calculated to be 13.5 times $\mathrm{LW}_{1/2}$, while the line

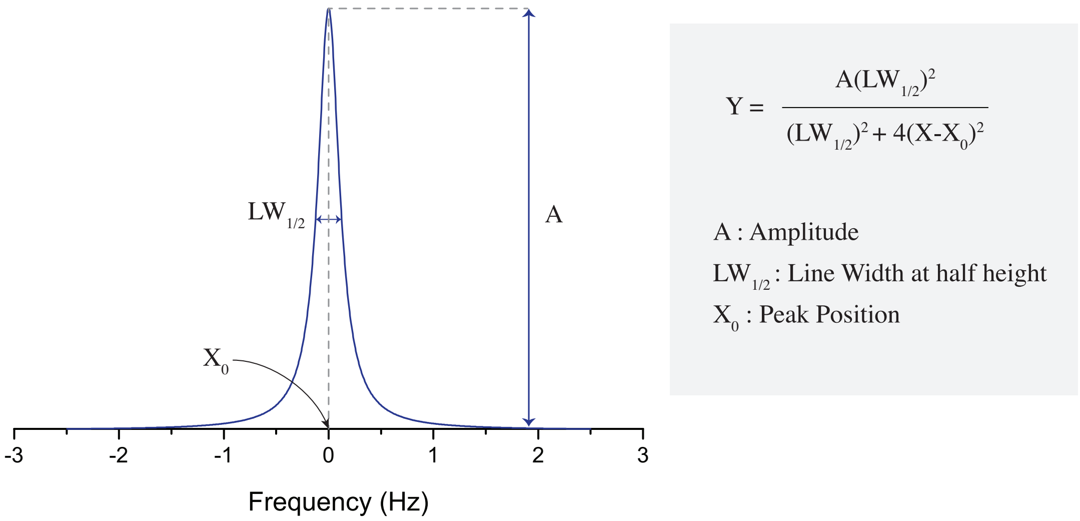

Figure 2.2 – Lorentzian line with $LW_{1/2} = 0.25$ Hz.

width at 0.11% height is calculated to be 30 times the $LW_{1/2}$. So, if the peak width at half-height is 0.30 Hz, the calculated values are 4.0 Hz Hz at 0.55% and 9.0 Hz at 0.11%. These values are larger than the theoretical values because the line widths at 0.55% and 0.11% height are very sensitive to shimming[92]. Other factors that influence line shape include the quality of the NMR tube, sample spinning, sample concentration, dissolved oxygen, and paramagnetic impurities. The latter three will lead to an overall broadening of the lines.

2.3 Sources of NMR line broadening

Several physical phenomena have an influence on both the shape and the position of an NMR spectral component. Generally speaking, the NMR line width is intimately related to the correlation times of magnetic interactions with the nuclear spins. Intuitively, the longer in time the FID signal is, the narrower the associated spectral component will be after applying the Fourier transform to the FID signal.

We can distinguish between homogeneous and inhomogeneous broadening of the line width. Both kinds of broadening are relevant to this thesis due to the different phases involved in chitosan deposition experiments. When performing experiments in solution, the spin system is under motional narrowing conditions and some inhomogeneous sources of broadening can be disregarded. However, in the gel phase, the polymer is solid or semi-solid. Therefore, dipolar interactions, as well as powder distribution effects, become relevant.

2.4 Homogeneous broadening

The most important contribution to the homogeneous broadening originates from the dipolar nuclear-nuclear and electron-nuclear spins interactions. The Hamiltonian of a spin-spin dipolar interaction can be written as:

$$H^{\mathrm{DD}} = -\frac{\mu_0}{4\pi}\frac{\gamma_1\gamma_2\hbar}{r_{12}^3}\left(3\cos^2\Theta_{12}-1\right) I_{1z}I_{2z} \tag{2.1}$$

where γ_1 and γ_2 are gyromagnetic ratios associated with nuclear spins I_1 and I_2, r_{12}^3 and Θ_{12} are the distance between spins 1 and 2 and the orientation of the segment joining those spins with respect to the magnetic field B_0. I_{1z} and I_{1z} are the components of spin 1 and 2 along the direction of B_0. Only the secular part of the dipolar Hamiltonian has been considered here since in high-magnetic fields, such as those used for NMR, the non-secular terms are negligible in comparison and may be discarded. The Hamiltonian H^{DD} can be considered as a perturbation of the Zeeman Hamiltonian describing the interaction of the nuclear spins with the static magnetic field at the nuclear positions. In liquid phase, the perturbation is time dependent since the angle Θ_{12} will vary as the molecule rotate and thumble in solution. In case of inter-molecular dipolar interactions, the value of r_{12} will also be time-dependent. It is also important to note that the Hamiltonian H^{DD} vanishes for $\Theta_{12} = \mathrm{atan}\sqrt{2} \simeq 54.74^\circ$, that is the angle that solves the equation $3\cos^2\Theta_{magic} - 1 = 0$.

In general, all microscopic fluctuations of the local magnetic field, will create a corresponding fluctuation of the NMR frequency for a certain nucleus. It can be shown that in the case of a gaussian distribution for fluctuations with mean square amplitude $\langle\omega^2\rangle$, the FID signal can be expressed as [93]:

$$G(t) = G(0)\exp\left[-\langle\omega^2\rangle\int_0^t (t-\tau)g(\tau)\mathrm{d}\tau\right] \tag{2.2}$$

where

$$g(\tau) = \frac{\langle\Delta\omega(t+\tau)\Delta\omega(t)\rangle}{\langle\Delta\omega^2\rangle} \tag{2.3}$$

is the correlation function describing the fluctuations of the resonance frequency ω.

It can be shown that for characteristic decay times (correlation times) for the fluctuations $\tau_c \ll t$, where t is the time scale of the NMR acquisition, the FID is given by

$$G(t) \simeq G(0)\exp\left(-\langle\Delta\omega^2\rangle t\tau_c\right) = G(0)\exp\frac{-t}{T_2'} \tag{2.4}$$

So, the relaxation rate of the FID signal is given by

$$\frac{1}{T_2'} = \langle\Delta\omega^2\rangle\tau_c \tag{2.5}$$

Since the FID decay is exponential, the corresponding line is Lorentzian, and $1/T_2'$ represents the full width at half maximum of the Lorentzian curve. In general, the total transverse relaxation rate ($1/T_2^*$) will be a combination of relaxation effects due to spin-spin interaction ($1/T_2$) and inhomogeneities in the static local magnetic environment ($1/T_{2i}$). If all these relaxation effects are independent, the total relaxation rate is the following sum:

$$\frac{1}{T_2^*} = \frac{1}{T_2} + \frac{1}{T_{2i}} \tag{2.6}$$

2.5 Inhomogeneous broadening

Inhomogeneous broadening of the line width can be traced back to spatial distributions of the local magnetic field and can have either microscopic or macroscopic origin. These effects contribute to both a dephasing of the transversal components of the nuclear spins and to the spread in frequency of the NMR absorption spectrum. Inhomogeneous broadening is a static ensemble averaging effect which usually superimpose over the homogenous linewidth and masks out the related dynamics.

We can point out the following the most realistic sources of inhomogeneous broadening in the specific case of the hardware used in this thesis: a “powder” average broadening for the solid part of the chitosan polymer, e.g. in the hydrogel phase; a field gradient experienced by the NMR microdetector due to imperfect alignment to the centre of the shim-coils axis; effects of eddy currents induced in metallic components of the sample inserts, especially in the case of the planar electrodes, where eddy currents and magnetic susceptibility optimizations were not taken into account; magnetic susceptibility discontinuities along the transverse directions to the B_0 field axis, due to the presence of a non-negligible amount of materials with different magnetic susceptibilities in proximity of the NMR detector. All these effects are graphically summarized in Figure 2.3 and briefly described in the next subsections.

2.5.1 Magnetic field inhomogeneities / magnetic field gradients

A static distribution of frequency can be generated by the presence of one or more superimposing gradients and distortions of the magnetic field within the sample volume. The severity of this effect largely depends on the strength of the gradients experienced by the sample. The resulting broadening is inhomogeneous and it is a consequence of the ensemble average across the full sample volume. In figure 2.3a and 2.3b we see a simple example of such gradients. Notably, the unwanted generation of a field gradient might originate from an incorrect placement of the detector itself on the NMR probe head. Even a small offset from the centre of the shim coils set would produce a non-curable distortion of the magnetic field.

2.5.2 Powder average broadening

A static distribution of molecular orientations can also lead to a line broadening effect. This is what is commonly referred to as “powder average”: when molecules do not have the ability and degrees of freedom to quickly reorient in space, such as in the case of deposited chitosan gel, the chemical shift for a certain NMR line will be distributed because the shift associated with each copy of the molecule would be slightly different, as the electronic cloud remains aligned to the chemical bonds. The result is an inhomogeneously broadened spectrum called a “powder spectrum”, a broad superposition of sharp resonance peaks whose amplitudes depend on the molecule orientations with respect to the static magnetic field. In crystalline powder material the spectrum assumes the characteristic shape illustrated in Figure 2.3d and it can be either a symmetric or an asymmetric distortion of the NMR line depending on value of the chemical shift tensor associated with the chemical bond.

2.5.3 Magnetic susceptibility discontinuities

When materials with different magnetic susceptibilities occupy the NMR coil volume, a jump in the static magnetic field would occur at the materials interfaces. The effect on the NMR linewidth originate from those discontinuities in the geometry and the associated susceptibility profiles in those cases where the interface plane is not parallel to the static magnetic field.

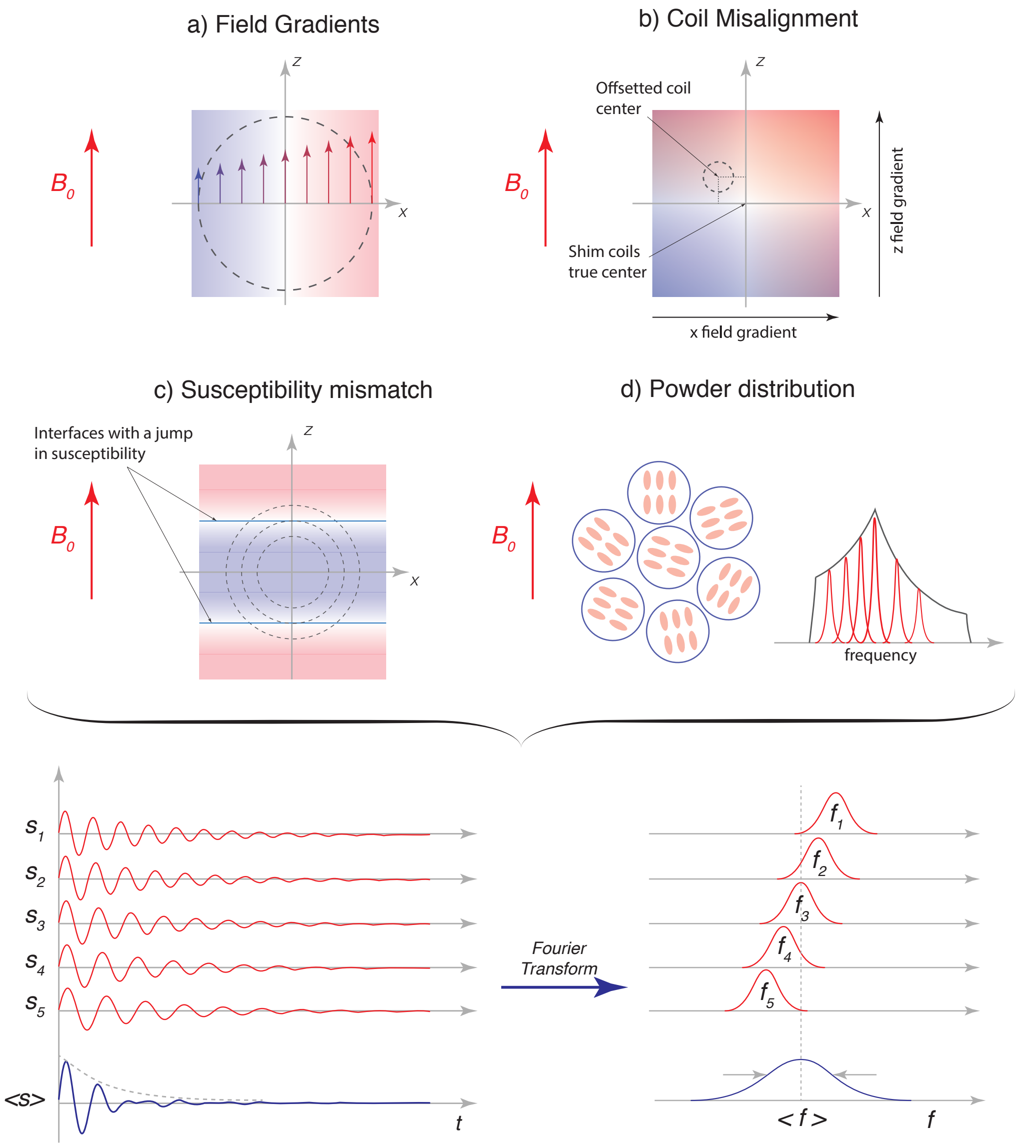
a) Field Gradients
b) Coil Misalignment
c) Susceptibility mismatch
d) Powder distribution
B_0
z
x
Offsetted coil center
Shim coils true center
z field gradient
x field gradient
Interfaces with a jump in susceptibility
frequency
s_1
s_2
s_3
s_4
s_5
<s>
t
Fourier Transform
f_1
f_2
f_3
f_4
f_5
< f >
f

Figure 2.3 – Sources of inhomogeneous broadening. The field gradient distributions are displayed as a colormap gradient going from red to blue. a) linear gradient along the x-direction within the volume defined by the NMR detector (dashed grey line). b) Coil misalignment effect. Two linear shim coil gradients along x- and z- directions are here represented to illustrate how a small offset of the NMR detector can lead to the introduction of undesirable inhomogeneities. c) a susceptibility mismatch generates a field gradient in proximity of the susceptibility jump at the material interface. The severity of this effect depends on the size of the NMR detector with respect to the structure producing the field distortion. d) a microcrystalline powder may lead to an asymmetric broadening of the line width.

The field generated by the magnetic dipoles induced in the different materials is usually a demagnetizing field, since most fabrication materials and most NMR solvents are diamagnetic. This effect is qualitatively illustrated in figure 2.3c, where a jump in susceptibility has been introduced, corresponding to the hypothetical presence of microstructured interfaces that are perpendicular to the direction of the B_0 field. Depending on the size of the detector and the number of such structures in proximity of the active volume, the distortion or broadening caused to the NMR line will be more or less severe.

2.6 Signal-to-noise measurements

Signal-to-noise measurement, or SNR, is an important criterion for accurate integrations and also one of the best ways to determine the sensitivity of an NMR spectrometer. In general, a higher S/N specification means that the instrument is more sensitive. It is also useful to roughly determine the time required for an experiment. It is important that the spectrum is recorded under the following standard conditions:

- Use a 90° pulse.
- Line Broadening of 1.0 Hz.
- Spectral Width of 15 to 5 ppm.
- A sufficient relaxation delay (at least $5 * T_1$).
- A sufficient digital resolution (less than 0.5 Hz/point).
- One transient.

Optimum signal-to-noise ratio for any sample is defined as that which occurs when using a line-broadening equal to the peak width at half height. When this line broadening is applied, the peak width at half-height doubles, i.e., it is the sum of the natural peak width at one-half height plus the line broadening applied. The equation used for calculating SNR is:

$$\frac{S}{N} = \frac{2.5A}{N_{\mathrm{pp}}} \tag{2.7}$$

where A is the amplitude of the chosen peak and N_{pp} is the peak-to-peak noise.

The signal-to-noise ratio of a given signal increases as the square root of the number of acquisitions; therefore, to double the signal-to-noise ratio, it takes four times as many acquisitions. Furthermore, the SNR is inversely proportional to the limit of detection (LOD), the lower detectable quantity, which has been loosely defined for an SNR value of 3[52]. As the SNR scales by the square root of the total acquisition time $\sqrt{t_{\text{acq}}}$, the normalised mass LOD has been defined as

$$\text{nLODm} = \frac{3n\sqrt{t_{\text{acq}}}}{\text{SNR}} \tag{2.8}$$

where n corresponds to the molar fraction within the fraction of the sample volume observed by the coil [94], and the normalised mass sensitivity (S_m) is obtained by taking the reciprocal value nLODm, multiplied by a factor of three. The SNR may be increased either by raising amplitude of the signal or by lowering the contribution of the noise.

2.7 Integration

The accuracy of the obtained integrals for most routine spectra is usually about 10-20%. This accuracy is usually sufficient, especially if the compound is already known. However, this accuracy is sometimes not sufficient to determine the exact number of hydrogen atoms contributing to a given peak, nor is it sufficient for quantitative applications (such as kinetic experiments or assays of product mixtures) where an accuracy of 1-2% is required. An accuracy of 1-2% can be achieved, but it is important to be aware of the factors that influence the integrations. These are as follows:

- The spectral width should be such that no peak is within 10% of the ends of the spectrum. This is because the spectrometer uses filters to filter out frequencies outside the spectral width. Unfortunately, the filters also tend to reduce the intensity of peaks near the ends of the spectrum.

- The recycle time + the acquisition time = total time (TT) should be at least five times T_l. Data should be collected under conditions which ensure that all the nuclei can fully relax before the next FID is sampled. The most challenging aspect of this criterion results from these experimental variables.

- The same area should be included or excluded for all peaks. For example, all peak integrals should be measured ±5 Hz around each peak, not ±20 Hz around one peak, ±10 Hz around a second peak, etc. Spinning sidebands are included in this category, and should consistently be either included or excluded.

Chapter 3

Materials and Methods

3.1 Fabrication Process

In this study, three different microfluidic platforms have been designed for the purpose of implementing a variety of experiments related to electrodeposition of chitosan. In the following I briefly illustrate the purpose of each platform.

First, we designed and fabricated a microfluidic platform hosting an array of planar electrodes, to perform parallel sequential electrodeposition of chitosan and demonstrate hydrogel stack addressability. With this platform, we investigated the possibility of tuning parameters of modification of chitosan with functionalized quantum dots, we performed a qualitative analysis of the multilayer deposition and a quantitative estimation of the amount of amine ($-NH_2$) groups exposed by the chitosan hydrogel. This platform was not designed to be compatible with a NMR microdetector and it only served the purpose of carrying out preliminary characterization experiments necessary for achieving satisfactory command over the electrodeposition technique. Further details about this design are listed in section 3.1.1.

The second platform consists of a microfluidic channel and a planar electrodes pair; in this case, the platform was designed taking into account compatibility to the NMR microdetector: we used 100 µm thick glass as substrate material on which gold working electrodes of different thickness, 15 nm and 30 nm, were grown. The thickness of the planar electrode plays a role in determining both the homogeneity of the RF field at the sample position. Further details are described in section 3.1.2.

The third version of the platform is a similar design as the second version, except for a different positioning the electrodeposition surfaces: a pair of elec-

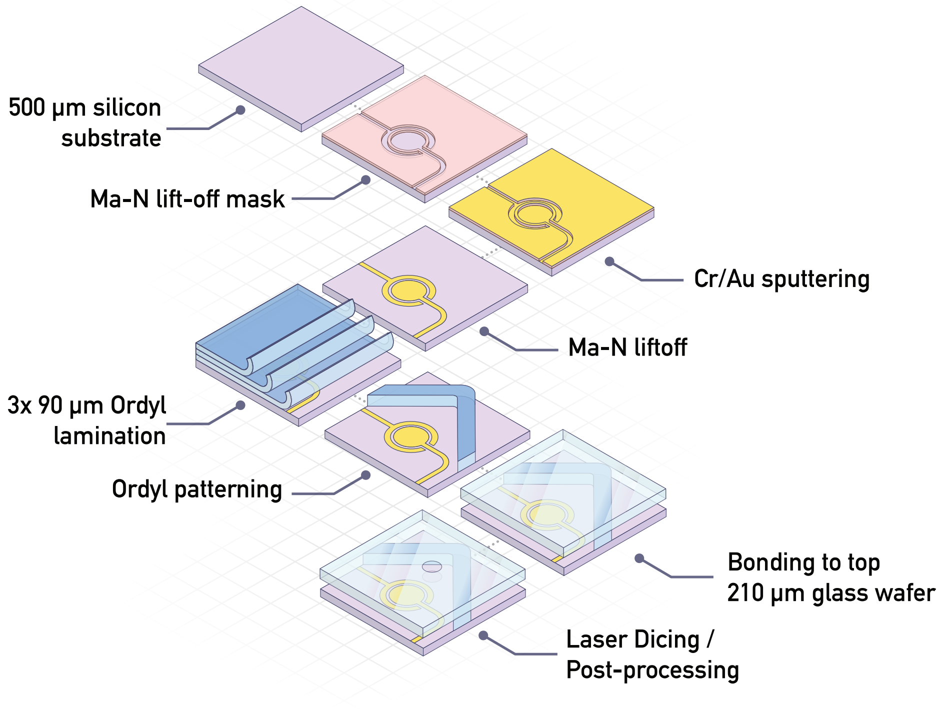
500 µm silicon substrate
Ma-N lift-off mask
Cr/Au sputtering
Ma-N liftoff
3x 90 µm Ordyl lamination
Ordyl patterning
Bonding to top 210 µm glass wafer
Laser Dicing / Post-processing

Figure 3.1 – Electrode array fabrication process. Each gold working electrode covers a nominal area of 1.76 mm^2

trodes were fabricated along the side walls of the fluidic channels instead of having a pair of planar of electrodes in the middle of the channel. This configuration goes under the name of "sidewall electrodes" in the present work. Two versions of the microfluidic channel with integrated sidewall electrodes were fabricated, namely a wide channel and a narrow channel. We used 100 µm thick glass as substrates, and then electroplated gold working electrodes on the side walls of the channel up to a thickness of 60 µm. A description of the fabrication process for sidewall electrodes sample inserts is provided in detail in section 3.1.3.

3.1.1 Electrode array microfabrication

The manufacturing of the electrodes array proceeded as follows: fabrication started with a 500 µm thick, 4-inch diameter silicon wafer. The substrate was cleaned using a sequence of acetone, isopropanol (IPA), and deionized water (DI) baths. An O_2 plasma treatment helped to improve wetting of the silicon surface by polar photoresists during spin coating. The wafer was further dry-baked on a hotplate at 100 °C for at least 2 minutes. After baking, the substrate was treated with the silanizing agent hexamethyldisiloxane (HMDS), to promote adhesion between the SiO_2 surface and the layer of ma-N1420 positive photoresist, which was spin coated immediately after. The wafer was spun at 3000 RPM for 30 seconds and underwent soft-baking for 2 minutes at 100 °C. The dry ma-N coating was exposed using an I-line mask aligner (MA6, Karl Süs, Germany) with a dose of $825\,\mathrm{mJ/cm^2}$ @ 375 nm under hard contact, followed by development in ma-D 533/S developer for 110 seconds to achieve the desired undercut. The wafer was rinsed thoroughly with DI water, dried and put in an oven at 200 °C for 2 hours to stabilize the resist prior to metal deposition. A 10/100 nm chromium (Cr)/gold (Au) seed layer was evaporated on the substrate by physical vapor deposition. Then, the ma-N 1420 layer was stripped in a megasonic acetone bath and the substrate was cleaned in IPA and DI water and dried under nitrogen flow. Ordyl SY390 (Elga Europe s.r.l., Italy) dry film resist was used to define the fluidic channel side walls[95]. The surface of the wafer was first activated in an O_2-plasma cleaner at 0.3 mbar, 40 °C and 20 W at 40 kHz to improve the adhesion of the first laminated layer. Four fresh layers of Ordyl were laminated onto the silicon substrate using a standard lamination device (Mylam 12, GMP) at 85 °C and roll speed 1 cm/s, resulting in a total nominal resist thickness of 360 µm. A 1-minute post-lamination bake was performed at 85 °C on a hotplate. The Ordyl stack was then exposed to UV light for a total dose of $180\,\mathrm{mJ/cm^2}$ @ 375 nm. A post exposure bake was performed for 1 minute at 85 °C. The Ordyl patterns were developed for 7 minutes in Ordyl developer under ultrasonic agitation. The developed structures were rinsed in IPA and DI water and dried under nitrogen flow.

At this stage, two versions of the device were fabricated. Fabrication of the first version, referred to as the “open configuration”, was completed at this step. The second version, referred to as the “closed configuration”, continued the fabrication with bonding to a top glass wafer using a hot embossing device (EVG 510HE) with an applied pressure of ~6 bar at a temperature of 95 °C for 30 minutes. Inlet and outlet holes were drilled into the top glass wafers before bonding, by machining the thin glass with a nanosecond UV laser (Trumpf TruMark 5000) pulsed at 30 kHz. The whole fabrication process is schematically shown in Figure 3.1.

3.1.2 Planar electrode inside microfluidic channel compatible with the NMR microdetector

The fabrication procedure for the electrodeposition platform compatible with the NMR detector differs from the protocol illustrated in section 3.1.1 in the definition of the planar electrodes. A Au/Cr etching strategy was here selected to achieve a higher adhesion of the metal layer onto the substrate, solving occasion peel-off issues encountered with the lift-off fabrication process. Encapsulation with Ordyl was performed identically to the procedure in section 3.1.1.

A 4-inch 210 µm thick glass wafer (SCHOTT DS263T-ECO) was cleaned with a sequence of acetone-IPA-DI water baths, rinsed and dried under nitrogen flow. The wafer was prepared for Cr/Au PVD sputtering by oxidizing the glass surface with oxygen plasma at 150 W RF power, 0.6 bar oxygen pressure for 5 minutes. Then the wafer was baked in a standard oven at 200 °C for 2 hours prior to sputtering of either 10/15 nm or 10/30 nm Cr/Au layer using physical vapor deposition. SU-8 was used to define the gold electroplating mask: the wafer was again cleaned in acetone-IPA-DIW baths and the surface was once again oxidised with oxygen plasma at 100 W RF power, 0.6 bar oxygen pressure for 10 minutes. A layer of SU-8 3025 was spin-coated onto the metal layer with the following coating protocol: 1) 0 → 500 RPM @ 100 RPM/s for 5s, 500 → 2000 RPM @ 300 RPM/s for 60 s, 2000 → 0 RPM @ 100 RPM/s for 5 s. The achieved target thickness for the SU8 layer was 20 µm. The wafer was soft baked at 95 °C for 12 minutes and exposed under a SVG 620 mask aligner for a total dose of 400 mJ/cm^2@365 nm UV light. After exposure the wafer was baked again at 95 °C for 4 minutes. The SU-8 structures were developed in a PGMA bath for 20 minutes, followed by a rinsing step in IPA for an additional 10 minutes. The wafer was dried with a nitrogen gun and further baked at 30 °C for 2 hours to remove excess moisture.

Additional metal gold was grown on the counter-electrode and the contact pads by electroplating the wafer in a Au plating bath at 20 A/m^2 current density for 40 minutes to achieve a target Au thickness of 5 µm. The SU-8 mask was then stripped using an R3T microwave plasma etcher for 30 minutes. The wafer was then cleaned in successive Acetone-IPA-DIW ultrasonic baths at 50 °C.

A Cr/Au etching mask was defined using ma-N 1410 and metal etching was performed with the following procedure: the wafer surface was oxidised with oxygen plasma at 100 W RF power, 0.6 bar oxygen pressure for 5 minutes. A ma-N 1410 resist layer was spin-coated at 3000 RPM for 30 s to achieve a thickness of 1 µm. The wafer was then baked on a hot plate at 100 °C for 90 s. The ma-N later was exposed under a SVG 620 mask aligner for a total dose of 475 mJ/cm^2 @ 365 nm UV light. ma-N patterns were developed in a ma-D 533S developer bath for 35 s. The wafer was then rinsed with DIW and dried with a nitrogen gun.

The gold layer was then etched by immersion in a gold etchant bath for 20 s and the wafer was then rinsed in DI water. The chromium layer was etched in a chromium etching bath for 1 minute, then the wafer was rinsed in DI water. Finally, the ma-N masked was removed by immersion in an acetone bath under agitation for 20 seconds.

A 90 µm Ordyl layer was laminated and patterend using the same procedure as in section 3.1.1 to define the microfluidic channel. Fabrication terminated with encapsulation by bonding to a top 210 µm glass wafer. Inlet and outlet holes were defined onto the top glass wafers after bonding, by machining the thin glass with a nanosecond UV laser (Trumpf TruMark 5000) pulsed at 30 kHz. The same laser was also used to dice the whole wafer. The whole fabrication process is illustrated in Figure 3.2.

3.1.3 Sidewall electrode inside microfluidic channel compatible with the NMR microdetector

The insert consists of a microfluidics channel sandwiched between two 210 µm-thick glass supports. In order to form high aspect-ratio side-walls as deposition sites together with the planar structures such as access tracks, pads, and counter-electrodes, two steps for metal deposition were performed. A 4-inch substrate, covered by the seed layer, was cleaned, and dehydrated. For the first mould, SU-8 3025 was patterned on the substrate as discussed elsewhere[96, 97].

Then, gold was plated on the accessible pads for the height of 10 µm. In the next step, the second mould was fabricated using SU-8 3025 for the total height of 100 µm. As the height of SU-8 is comparable to the thickness of the substrate and in order to reduce the stress, the baking processes was done at 65 °C for 90 minutes. The dose of the UV exposure also has been adjusted to 150 mJ/cm^2–225 mJ/cm^2.

Next, the high aspect-ratio side-walls were electroplated to achieve a 60 µm height. The mould structures were then etched followed by seed layer etching.

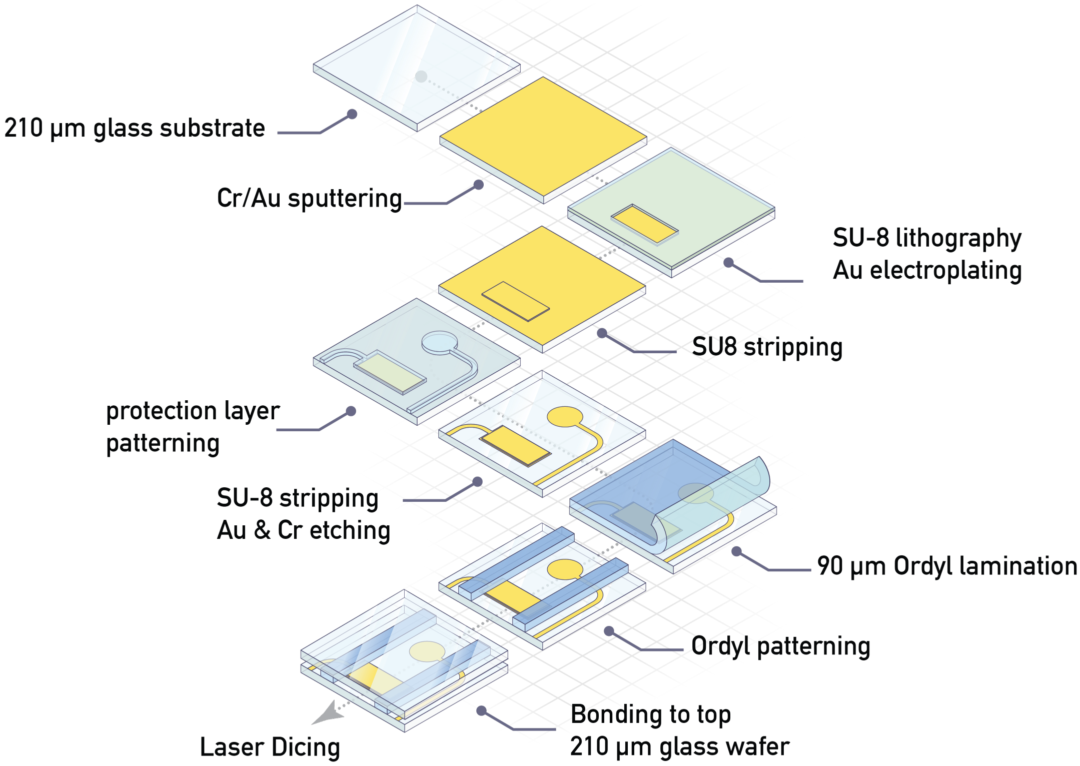
210 µm glass substrate
Cr/Au sputtering
SU-8 lithography
Au electroplating
SU8 stripping
protection layer
patterning
SU-8 stripping
Au & Cr etching
90 µm Ordyl lamination
Ordyl patterning
Bonding to top
210 µm glass wafer
Laser Dicing

Figure 3.2 – Illustration of the fabrication process for the planar electrode microfluidic platform with two different thicknesses of the working electrode, 15 nm and 30 nm Au. Each gold working electrode covers a nominal area of 1.76 mm^2.

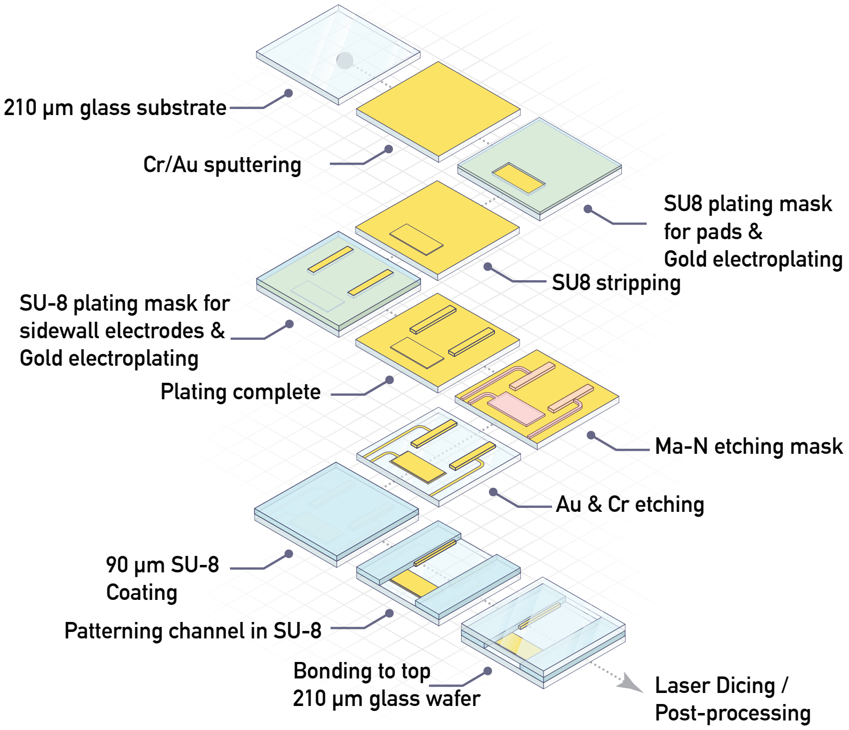
210 µm glass substrate
Cr/Au sputtering
SU8 plating mask for pads & Gold electroplating
SU8 stripping
SU-8 plating mask for sidewall electrodes & Gold electroplating
Plating complete
Ma-N etching mask
Au & Cr etching
90 µm SU-8 Coating
Patterning channel in SU-8
Bonding to top 210 µm glass wafer
Laser Dicing / Post-processing

Figure 3.3 – Main steps in the fabrication process for the sidewall electrodes microfluidic chip compatible with the NMR Helmholtz microcoil. Each gold working electrode covers a nominal area of 0.42 mm^2.

After that, a 180 µm SU-8 3025 was spin-coated for both encapsulation of the electrodes and structuring the channel. Similar to the previous step, SU-8 3025 was baked in lower temperature for a longer time before exposure. The unexposed SU-8 3025 was developed by PGMEA developer and the channel was formed.

In order to facilitate the bonding of the wafer to the top glass, a 20 µm-thick layer of Ordyl SY390 was laminated on top of the SU-8 structures. The Ordyl layer was then structured using UV exposure and development. Just after Ordyl development, the bonding to the top glass wafer was performed using a hot embossing machine. The access to the microfluidics was provided through inlet and outlet holes, drilled through the top glass with a nanosecond pulsed laser. The fabrication process for this the device is illustrated in Figure 3.3.

3.2 Substrate Characterization

3.2.1 Materials

The following chemicals were purchased from Sigma Aldrich: chitosan from crab shells (85% deacetylation, 200 kDa), poly(ethylene glycol) bis(carboxymethyl) ether (average M_n 250, PEG), poly(amidoamine) dendrimers G0 PAMAM (20 wt% solution in methanol), N-(3-(dimethylamino)propyl)-N-ethylcarbodiimide hydrochloride (EDC) 99%, N-hydroxy-succinimide (NHS) 97%, 0.01 M of phosphate buffer solution (PBS) of pH 7.4 was made with PBS tablets in deionized (DI) water, ethanol 99.8%, and Cadmium Telluride (CdTe) carboxylic acid functionalized. Water was deionized with Millipore SUPER-Q water system until final resistivity $\sim$>18 MΩ cm was reached.

3.2.2 Chitosan characterization

Chitosan (CS) modification was always performed in solution (i.e. pH 5.5). After each modification, the resulting polymer was purified by precipitation with sodium hydroxide (NaOH) and dialysis against phosphate buffer saline (PBS, at pH 7.4) (3 fold by volume) for at least one day before either the next coupling reaction, chemical analysis, or electrodeposition.

3.2.3 Modification of chitosan

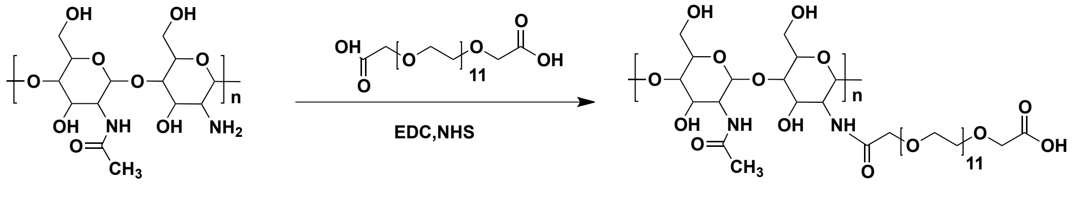

Figure 3.4 – Reaction scheme for the chitosan+PEG modifications described in this work.

Polyethylene glycol (PEG) coupling: Chitosan was coupled with PEG featuring diacid functionality. PEG (11 mg/mL) was activated with EDC (2 mg/mL) and NHS (1 mg/mL) in 20 mL of deionized water for 30 minutes at 24 °C. The PEG:EDC:NHS ratio was 1:0.5:0.5. This solution was then added to a 1% w/v chitosan solution containing the appropriate quantity of amine reaction centres

Table 3.1 – Molar ratios of chitosan, PEG, and PAMAM (CS:PEG:PAMAM)

Theoretical	Experimental	
	^{1}H NMR	Titration
1 : 1 : 1	1 : 0.81 : 0.11	1 : 0.75 : 0.09
1 : 2 : 2	1 : 0.74 : 0.06	1 : 0.61 : 0.06
1 : 1 : 0.5	1 : 0.78 : 0.13	1 : 0.70 : 0.09
1 : 1 : 2	1 : 0.76 : 0.20	1 : 0.75 : 0.13
1 : 0.5 : 0.5	1 : 0.53 : 0.03	1 : 0.43 : 0.05

(molar ratios presented in Table 3.1). The reaction was allowed to proceed for 3 hours at 24 °C before purification.

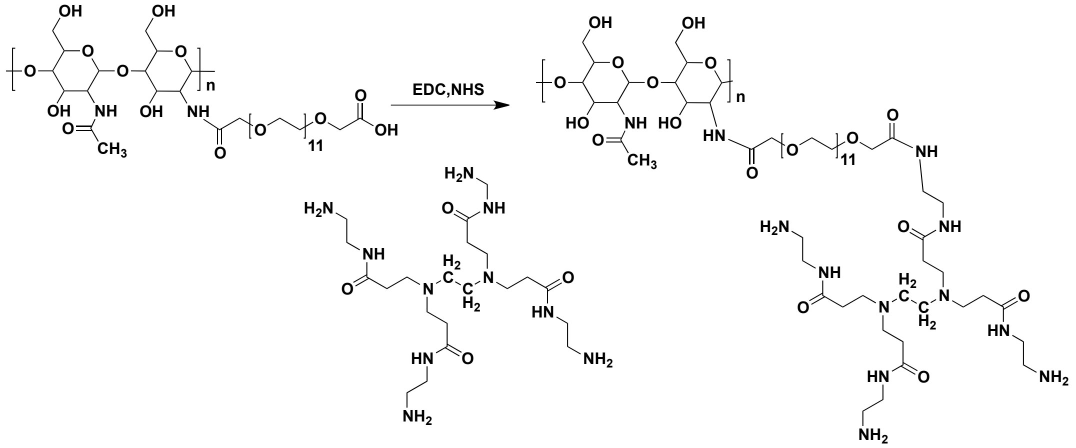

Figure 3.5 – Reaction scheme for the CS-PEG+PAMAM dendrimer modifications described in this work.

Poly(amidoamide) (PAMAM) coupling: PEG functionalized chitosan was activated with EDC and NHS for 30 hours at 24 °C. To this solution, a PAMAM solution (diluted in MQ water, pH adjusted to 5.0) was added dropwise and allowed to react for approximately 16 hours at 24 °C before purification (molar ratios presented in Table 3.1).

3.2.4 Visualisation of chitosan

Quantum dot labelling: Carboxyl-functionalized quantum dots (QD) were activated by preparing a solution of 0.1 µmol/mL of QDs together with 1 mg/mL of NHS and 10 mg/mL of EDC in PBS at pH 7. The QD:EDC:NHS ratio was 1:10^4:10^4. QD solubility was assisted by bath sonication. The reaction mixture was stored for 2 to 4 hours at room temperature, and then stored at 4 °C

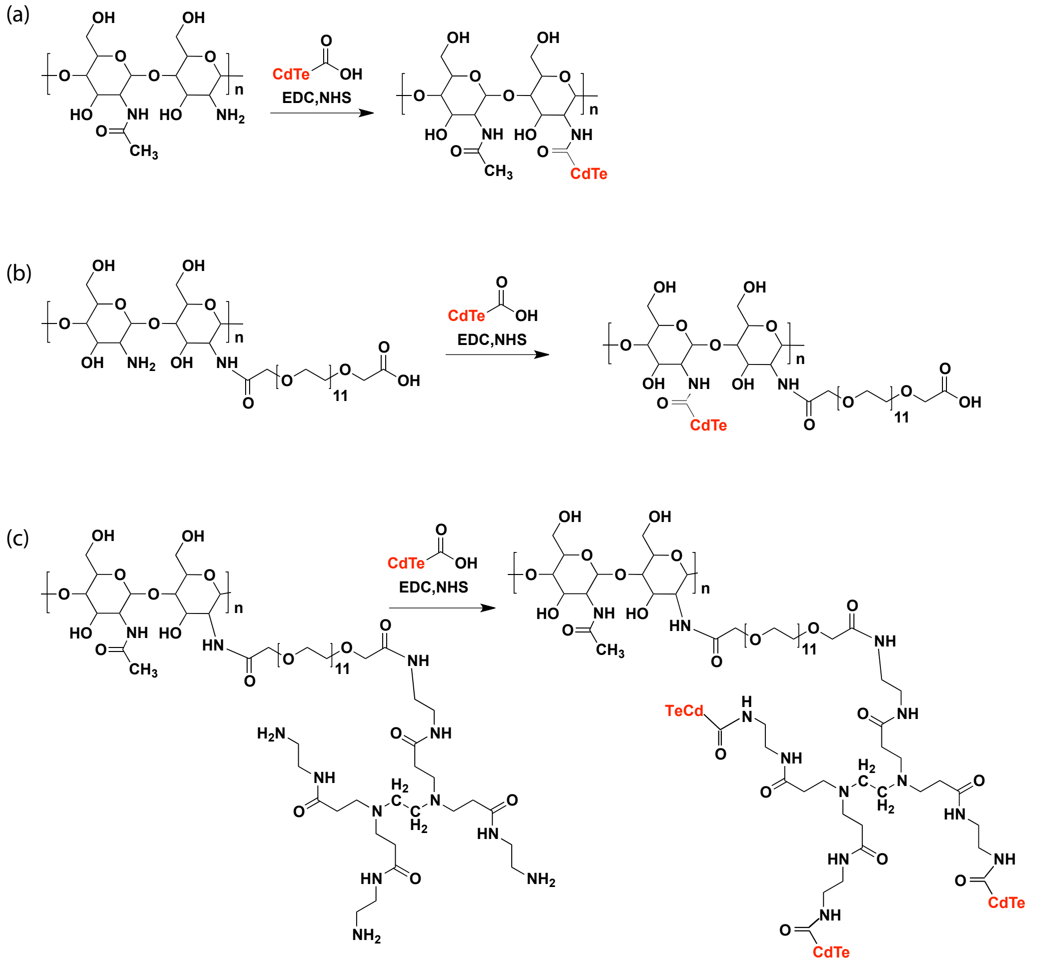

Figure 3.6 – Quantum dot labelling (CdTe) of (a) CS, (b) CS-PEG, and (c) CS-PEG-PAMAM was performed in order to visualize the electrodeposited materials. Quantum dots with different emission wavelengths were selected to visualize the different layers of deposited materials.

overnight[98]. From a solution of activated QDs, aliquots were taken and mixed with 1 % w/v of chitosan solutions which were allowed to react for 2-4 hours at room temperature to complete the coupling. The reaction mixture was dialyzed on a membrane with a MWCO of 10000 against pH 7.0 PBS buffer and stored at 4 °C.

Coupling quantification: Purified functionalized chitosan was subjected to both nuclear magnetic resonance (NMR) and potentiometric titration analyses to estimate the coupling yields. For NMR, a known quantity of the modified gel (typically 500 mg) was dissolved in D_2O and the pH adjusted using deuterated hydrochloric acid (DCl). Spectra of all reagents were also measured by preparing solutions at 60 mg/mL in acidic D_2O. NMR spectra were collected on a Bruker

AVANCE system operating at a ^{1}H Larmor frequency of 400.13 MHz (credits to Institute of Biology (IBG), KIT). Each spectrum was the result of 16 scans, each containing 64 K data points over a spectral width of 20 ppm. The resulting FID was zero-filled by a factor of 2 and multiplied by an exponential function equivalent to 0.3 Hz linewidth prior to Fourier transform. For potentiometric titration, a known quantity of gel was dissolved in acidic water adjusted with a known quantity of HCl. Titration was performed with 1 : NaOH, with sufficient time allowed for the pH to stabilize before each addition.

3.3 Electrodeposition (ED) of Chitosan

A chitosan solution (1 % w/v, pH 5.5) was prepared by dissolving chitosan in a diluted HCl 0.2 M solution as previously described[99]. The solution was filtered through a 5 µm syringe filter before use. Gold electrodes were first cleaned with ethanol and washed thoroughly with DI water, followed by drying under nitrogen stream. We performed electrodeposition of chitosan in an open and a closed configuration. In the open configuration, the electrode array was exposed directly to the chitosan solution, whereas in the closed system the chitosan solution was injected into the fluidic channel enclosing the electrode array. The electrodes were connected to a precision current source using the on-chip gold metal pads. The height of the electrodeposited chitosan (open configuration) was measured by mechanical profilometry utilizing a Dektax II profilometer. Profilometry data were exported and processed using MatLab R2017b. A PID-stabilized current density of 3 A/m^2 was run through the chosen electrode pair for a certain time to obtain a deposited layer of desired height. After electrodeposition, the chitosan solution was flushed and the deposited assembly was rinsed with DI water.

3.3.1 Setup experiment for in situ ED

A specialised probe head insert (Figure 3.7a), compatible both with a commercial Bruker Micro 5 NMR probe and custom NMR probes available at IMT-KIT, was designed and fabricated to accommodate the requirements for an in situ chitosan electrodeposition experiment integrated with NMR detection via a micro-coil. The support structure of the insert was fabricated in PMMA. The base of the insert includes RF female connectors to interface to the RF lines exposed on the probe heads. The NMR Helmholtz microcoil is mounted on top of a PCB, hosting electrical tracks for both RF signal transcieving (^{1}H channel) and chitosan electrodeposition. The top side of the insert features the electrical connections for electrodeposition and the fluidics connectors to the outside of the NMR magnet. A 4-channel PCB header was selected to allow for connection to the electrodeposition lines and other on-board sensors, such as a temperature sensor to monitor reaction temperatures close to the NMR detectors (not implemented in this work). This multi-purpose connector slides through the open top end of the micro gradient sleeve and exposes electrical and fluidic interfaces to the outside, even in such instances where *ad hoc* modifications to the NMR probe are not possible, such as the case of commercial Bruker probes. Connections from the PCB electrodeposition lines to the gold pads on the microfluidic chip rely on manual soldering of tin-plated copper wires, as shown in Figure 3.7c.

The fluidic pathway consists of two inlet/outlet soft silicone tubing segments embedded into the top side of the probe insert, connecting to polyethylene tubings on the insert side and to brass tubings to the outside. The microfluidic chip is fluidically interfaced to the tubings via two custom connectors consisting of a machined Teflon body bonded to a glass slide and a soft PDMS pad, to adapt the connector to any wedge defects when mounting it on top of the microfluidic chip (Figure 3.7b).

After the assembly was completed and installed in the probe, chitosan solution was flushed into the tubings connected to the microfluidic channel (see Figure 3.7). Then a DC microcurrent was applied to the poles of the ED electrodes for 5 minutes. The current was then switched off and an NMR spectrum was collected on a Bruker AVANCE system operating at a ^{1}H Larmor frequency of 500.13 MHz.

3.3.2 NMR Data Acquisition

The detector was a 1.2 mm diameter Helmholtz coil similar to the one reported by Spengler *et al.*,[60] tuned to 500 MHz (^{1}H Larmor frequency at 11.74 T) and matched to 50 Ω. The microfluidic devices containing the different electrode configurations were slid into a slot between the two windings of the Helmholtz pair. The microfluidic channels were designed so that the electrochemical sites are located inside or in close proximity to the field of view (FOV) of the Helmholtz

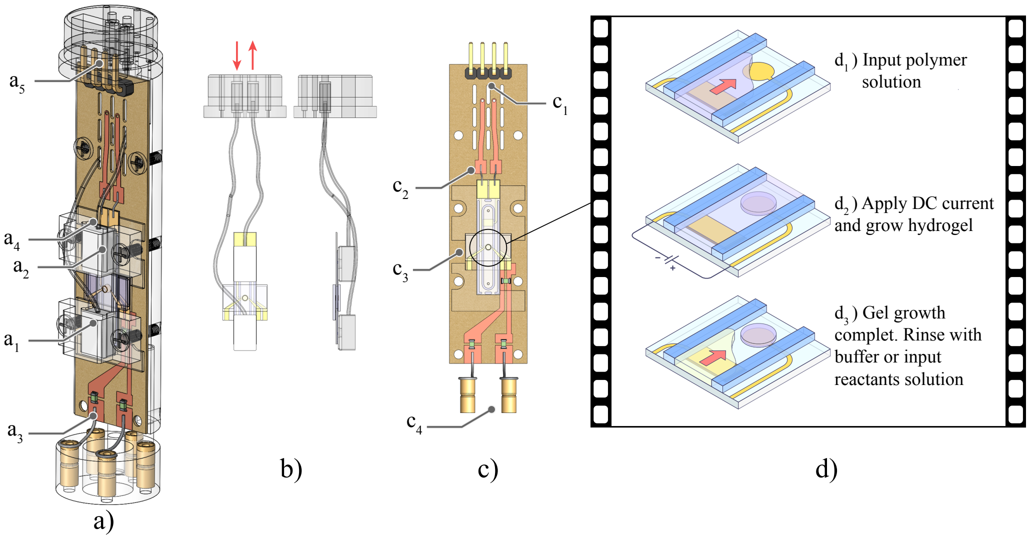
a_5
a_4
a_2
a_1
a_3
a)
b)
c_1
c_2
c_3
c_4
c)
d_1) Input polymer solution
d_2) Apply DC current and grow hydrogel
d_3) Gel growth complet. Rinse with buffer or input reactants solution
d)

Figure 3.7 – Experimental setup for *in-situ* electrodeposition of pre- and post- modified chitosan inside the microfluidic chip. a) overview of the NMR probe head insert used in this work, showing the main elements of the device: a1) PCB hosting RF tracks, tuning and matching fixed capacitors, the electrodeposition tracks and the NMR microcoil, a2) the microfluidic insert mounted inside the Helmholtz pair microcoil, a3) insert base with RF female connectors, a4) microfluidic connectors and connectors clamps, a5) topside connector supporting both electrical and fluidic connections to the outside. b) highlighted fluidics components, left side view and top view. c) highlighted electrical components: c1) electrodeposition lines and PCB header connector, c2) tin-plated copper connections between PCB and microfluidic insert, c3) microcoil NMR detector, c4) ^{1}H NMR RF lines. d) schematic illustration of the in-situ electrodeposition process: d1) loading the microfluidic channel with the polymer solution, d2) Applying a DC bias to the electrode pair to initiate electrodeposition, d3) rinsing with a buffer and/or loading the channel with a reagent solution.

coil. The entire setup consisting of the Helmholtz coil with the tuning and matching capacitors and the microfluidic structure was adapted to the commercial probe. This design aligned the middle axis of the microfluidic channel to the z-axis of the magnet, which is also the direction of the static magnetic field (B_0), while the Helmholtz coil generated the excitation RF field along the nominally-axis of the magnet frame of reference (B_1).

For the experiment, a one-dimensional NMR experiment was performed on the sucrose sample at 30 °C to observe the resolution spectra for planar and sidewall electrode configurations as a test measurement. The applied power was 0.8 W and shimming was performed manually up to the second order parameters. Each spectrum represents 64 scans. 18000 data points were collected for each scan over a spectral width of 20 ppm, the relaxation delay being set to 10 s. The resulting signal was Fourier transformed after multiplication with an exponential function equivalent to 0.3 Hz line broadening. The full width at half maximum of the TSP peak was calculated as a measure for the spectral resolution.

3.3.3 Nutation and MRI Experiments

Nutation. ^{1}H NMR experiments were performed using TopSpin 3.5, the operating and processing software for Bruker NMR spectrometers. A one-dimensional NMR experiment was carried out on the sucrose sample at 30 °C. The applied power was 0.8 W and shimming was performed manually up to the second order parameters. Each spectrum represents 64 scans. 18000 data points were collected for each scan over a spectral width of 20 ppm, the relaxation delay being set to 5 s. The resulting signal was Fourier transformed after multiplication with an exponential function equivalent to 0.3 Hz line broadening. The full width at half maximum of the TSP peak was calculated as a measure for the spectral resolution. A nutation experiment was performed in order to determine the B_1 field homogeneity. The nutation spectrum consists of 300 single scans using 0.8 W applied power with an increment of 1 µs. A relaxation delay of 10 s was set between two consecutive scans. Each data point in the nutation spectrum, represented by a single NMR peak, was integrated and plotted as part of a continuous curve to facilitate comparison with the simulated experiments.

MRI. B_1 distributions for inserts with different electrode configurations were studied through MRI experiments (ParaVision 6.0.1) using a sucrose sample. The experimental parameters of the *Flash* sequence were set as follows: TR/TE - 200 ms/4 ms, slice thickness - 100 µm along the y-axis, in-plane resolution - 40×40 µm, Tscan - 53 min, FOV 2×2 mm^2, bandwidth - 10 kHz, and 512 averages. The duration of the excitation pulse was fixed at 1.1 ms and its power level was adjusted to achieve different flip angles. *FieldMap* sequences were performed to study B_0 distribution experimentally, at the detection zone. The *FieldMap* sequence applies a 3D double gradient-echo image sequence with two different echo times, and based on the phase and magnitude differences between the echos, it calculates the B_0 distribution.[100] The experimental parameters of the *FieldMap* sequence were set as follows: TR - 35 ms, TE1/TE2 - 1.31 ms/7.03 ms, isotropic voxel size - 90 µm, Tscan - 76 min, FOV $2.9 \times 2.9 \times 2.9$ mm^3, bandwidth

- 30 kHz, number of averages - 128, flip angle - 50°. SNR threshold was set to 5 for data collection to minimise noise-induced image distortions. The slice which corresponds to the sample position in the zx-plane has been considered for representation and analysis. The standard deviation of the collected map was calculated and studied as a measure for the B_0 homogeneity. For this purpose, the outermost pixels of the acquired image were filtered out to further reduce the noise contribution.

3.3.4 NMR procedure for in situ ED

A reference one-dimensional NMR experiment was initially performed on the sample containing only the CS solution at 30 °C, to identify the chitosan signal at ~3.3 ppm (singlet,^{1}H). Electrodeposition was monitored by collecting a series of ^{1}H NMR spectra as a function of time. The current input for the electrodeposition was left on during NMR acquisition. Each NMR spectrum was a result of 200 scans, each containing 34000 data-points over a spectral width of 20 ppm, the relaxation delay being set to 1 s. The resulting signals were multiplied by an exponential function equivalent to 0.3 Hz line broadening prior to Fourier transform.

3.4 Application of the system: Determination of the function of enzymes

The in situ electrodeposition platform was used in a proof-of-concept application to determine the function of the enzymes. Taking advantage of biocompatibility of the chitosan hydrogel, the enzymes were bound to chitosan polymeric chains in solution using a suitable molar ratio, as described in section 3.4.1. Then the enzymatic reaction was studied using this platform in a real-time measurement by NMR spectroscopy.

3.4.1 Preparation of enzymes towards substrates

Materials

Enzymes: Urease (from Canavalia ensiformis (Jack bean)) with a specific activity of 100000 u/(g of enzyme) (pH 7.6, 303 K), glucose oxidase (from Aspergillus

Niger) with a specific activity of ≥100,000 u/(g of enzyme) (E. C. 1.1.3.4, type X-S, pH 7.6, 303 K) and catalase (from Bovine liver) with a specific activity of lyophilized powder, 2,000-5,000 u/mg protein were purchased from Sigma-Aldrich.

Substrates: Urea (powder, BioReagent, for molecular biology, suitable for cell culture), D-glucose (≥99.5% (GC)) and glucono-δ-lactone (≥99.0%) were purchased from Sigma-Aldrich. NMR solvents: Deuterium oxide D_2O (99.9 atom % D), and 3-(trimethylsilyl)- propionic-2,2,3,3-d_4 acid sodium salt (99.9 atom % D, contains 0.05 wt. % TSP), deuterium chloride (99 atom % D DCl), and deuterium sodium oxide (99 atom %NaOD),

Polymers: chitosan from crab shells (85% deacetylation, 200kDa), poly(ethylene glycol) bis(carboxymethyl) ether (average MW= 250, PEG),
Coupling reagents: N-(3-(dimethylamino)propyl)-N-ethylcarbodiimide hydrochloride (EDC) 99%, N-hydroxy-succinimide (NHS) 97% were purchased from Sigma-Aldrich.
Buffers: 10 mM of phosphate buffer solution (PBS) of pH 7.0 was made with PBS tablets, and 200 mM of sodium acetate (NaAc) of pH 5.5 was made with NaAc tablets in deionized deuterated (D_2O) water. The pH was adjusted with deuterium chloride (DCl), and deuterium sodium oxide (NaOD). (All solutions and dilutions will use this stock buffer to maintain the same pH 6.5-7.0 and the same concentration of TSP (50 mM) throughout.

Experimental Procedures

(i) *Experiments with enzymes using a 5 mm Bruker insert, **saddle coil**:*

Enzymes in a solution: Two different samples were used in a standard 5 mm NMR tube. The first sample, containing only the substrate, was prepared in an Eppendorf vial starting from a 1000 mM stock solution for Urea and a 200 mM stock solution for D-Glucose in total final aliquots of 200 mM NaAc buffer at pH 7.0. For urea samples the stock was divided into 1000 mM, 500 mM, 250 mM and 100 mM aliquots with a final volume of 1 mL each. For D-glucose samples, the stock solution was diluted down to 100 mM, 50 mM, 30 mM and 10 mM aliquots with a final volume of 1 mL each. A 500 µL volume was taken from the aliquots and transferred to a 5 mm NMR tube. This first kind of sample was used to adjust the NMR parameters.

The second sample was dedicated to the kinetic experiments and contained 1000 mM urea and 2.0 mg/mL urease. The second sample was prepared by transferring 1 mL of the 1000 mM urea stock solution into an Eppendorf vial loaded with 2 mg dry stock enzyme. 500 µL of the so-obtained solution were transferred to an NMR tube for acquisition. A timer was started right after mixing the stock solution with the dry enzyme to track the intertime between the start of the enzymatic reaction and the acquisition of the first usable NMR spectrum. We labelled this intertime as t_0. The same procedure was used for the kinetic study of the GOx enzyme. In this case a stock solution with 100 mM D-Glucose was prepared and 1mL of the stock were mixed with 4 mg/mL dry GOx and 1 mg/mL catalase in an Eppendorf vial.

Enzymes coupled to chitosan polymer, CSPEG: Preparation of CSPEG is described in section 3.2.3. After dialysis of CSPEG, 0.6 g CSPEG hydrogel were weighed. This amount was chosen because of its good solubility. The CSPEG was activated with EDC and NHS in 1 mL deionized water for 30 minutes at 24 °C. The ratio CSPEG:EDC:NHS was set to 1:0.5:0.5. Then each enzyme (urease: 2 mg; GOx: 4 mg; catalase: 1 mg) was added to this solution in a separate vial. The reaction was carried out at 24 °C for 3 hours before a purification step. Purification was performed by dialysis of the solution with PBS, overnight. For the kinetic study involving Urs, 0.6 g of the enzyme-bound CSPEG hydrogel (CSPEG-Urs) was weighed. The final sample was prepared by transferring 1 mL of the 1000 mM urea stock solution into an Eppendorf vial containing the CSPEG-Urs hydrogel. 500 µL of the obtained solution were transferred into an NMR tube. A timer was started at this point to track the intertime t_0 between start of the reaction and acquisition of the first NMR spectrum. The same procedure was followed for kinetic studies of the GOx enzyme, mixing 0.6 g (CSPEG-GOx, CSPEG-cat) hydrogel with 1 mL 100 mM D-Glucose stock solution.

(ii) *Experiments with Enzymes using a **Helmholtz** pair microcoil:*

To ensure consistency in experimental conditions, the preparation of solution containing the enzymes and either coupling or not coupling to the CSPEG polymer were carried out according to the same protocol as in (i), except for the final target sample volume. In this case the sample volume is defined by the fluidic channel on board of the microfluidic sample insert, that is 3.2 µL for planar electrode and wide channel sidewall electrode, meanwhile the volume of narrow channel of sidewall electrode is 2.5 µL .

Preparation of the enzyme's solutions:

- Solution A: 1000 mM Urea;
- Solution B: 100 mM D-Glucose;
- *Solution C: 35 µM CSPEG-Urs (15 u in 10 µL);
- *Solution D: 20 µM CSPEG-cat (1 u in 10 µL);
- *Solution E: 32 µM CSPEG-GOx (10 u in 10 µL)

(*Note:This is the expected number of units assuming 100% coupling yield)

200 mM NaAc buffer at pH 7, and 50 mM TSP as NMR internal reference were added to solution A and B to stabilise the pH and to set an NMR chemical shift reference at 0 ppm, respectively. Solutions C, D and E were filtered through a 5 µL polycarbonate filter, filled into three separate syringes.

Electrodeposition of the first layer of CSPEG-Urs: Solution C was injected into the microfluidic channel, then electrodeposition was carried out for 15 minutes by running a PID-stabilized DC-current (current density of $3\,\mathrm{A/m^2}$) through the chosen electrode pair to obtain a deposited layer of desired height 15 µm–20 µm. After electrodeposition, the enzyme solution was flushed and the channel was rinsed with D_2O water. Then solution A with 50 mM TSP in 200 mM NaAc at pH 5.5 was injected and the inlet and outlet were immediately sealed. The sample insert was then mounted on the probe and the probe was transferred to the NMR magnet for real-time monitoring. The same procedure was followed by for deposition of solutions D and E.

Electrodeposition of multi-layered chitosan gels: solutions were injected in the microfluidic chip in the following order: 1) solution C, 2) electrodeposition, 3) solution D, 3) electrodeposition, 4) solution E, 5) electrodeposition. Each deposition step was carried out for 15 minutes with the same current density (3 A/m^2) to obtain a deposited multilayer of the desired height 15 µm–20 µm). After electrodeposition, the leftover polymer+enzyme solution was flushed out and the deposited hydrogel assembly was rinsed with D_2O water. Then the substrates (500 mM urea and 100 mM D-glucose with 50 mM TSP in 200 mM NaAc buffer at pH 7) were injected into the microfluidic chip and the inlet and outlet were immediately sealed. The sample insert was then mounted on the probe and the probe was transferred to the NMR magnet for real-time monitoring. The time required to prepare the sample outside the magnet until the time of the first measurement was about 80 minutes (including the total time of the electrodeposition + shimming process). The procedure was performed outside the magnet, as the thickness of the hydrogel layers can be estimated by optical microscopy to calculate the initial unit of enzymes within the hydrogel. Nevertheless, the process can also be performed inside the magnet if the correlation of the thickness of the hydrogel with the deposition over time can be estimated earlier.

3.4.2 Real-Time NMR Measurements

The experiments were performed with two different NMR coils. As a reference, a control experiment for the kinetic reaction was performed using a standard NMR saddle coil and a 5 mm NMR tube. The data were collected for a certain interval of time. Then chitosan hydrogel coupled to the enzymes was electrodeposited within the microfluidic NMR insert. To study the electrodeposition process itself, electrodeposition was performed inside the magnet, i.e. in situ, as described in section 3.3.1. To determine the function of the enzymes, the electrodeposition of chitosan coupled to the enzymes was performed outside the magnet, as described in section 3.4.1 (using Helmholtz coil) and the whole platform was then transferred inside the magnet. The data were collected for a certain interval time, in the range 100-1000 minutes, to ensure conclusion of the enzymatic reaction.

A one-dimensional NMR experiment was performed on the first sample containing only urea at 30 °C to identify the signal of the urea at 5.8 ppm (broad, ^{1}H). A standard pulse calibration sequence (nutation sequence) was performed to determine the 90° pulse. All chemical shifts are expressed in units of parts per million (ppm) with respect to TSP's Larmor frequency. Each one-dimensional NMR spectrum was collected on a Bruker 500 MHz NMR spectrometer with a spectral width of 18.93 ppm (9469.70 Hz) over 34000 acquisition points for a total FID measurement time of 1.80 s. A relaxation delay of 1 s was used between the scans and 8 scans (for saddle coil) and 64 scans (for Helmholtz coil) were signal averaged and saved for further processing. This experiment was arrayed to collect FIDs continuously one after another and a total of 156 such experiments (for Helmholtz coil: 156×1.92 min $= 300$ min) were performed. The relaxation delay was set to 1 s, to ensure that as many intermediate spectra as possible could be recorded before the complete enzymatic conversion of urea into the products. The experiment was set up to collect FIDs continuously, in order to follow the reaction. A delay of 10-20 minutes was added between NMR acquisitions, to allow for a reasonable time resolution, considering the characteristic time of the reaction (10-100 minutes), and to limit the amount of data points (spectra) to be post-processed. NMR data were processed using the TopSpin (Operating and processing software for NMR spectrometers), Matlab2016b and Origin 2016.

3.4.3 Calculation of the enzyme units when determining enzymatic activity

The following protocols were used to quantify enzymatic activity:

Theoretical unit Urs in solution

$$U_{\text{Urs, theoretical}} = \frac{200\text{unit}}{1\text{mL}} \times \text{volume of microfluidic channel}$$

Active unit Urs based on V_{max}

One mole of urea produces two moles of ammonia. The extracted V_{max} of the reaction gives M_{urea}/min, which corresponds to M_{NH_3}/min $\times 0.5$. Then the active unit can be estimated by multiplication with the microfluidic channel volume of the reaction (3.5 µL for the planar electrode and 2.5 µL for the narrow channel sidewall electrode).

$$U_{\text{Urs, active}} = (V_{\text{max}} \times 2)\frac{M_{\text{NH}_3}}{min} \times \text{Volume of reaction}$$

Active unit GOx based on V_{max}

One mole of glucose produces one mole of gluconic acid. V_{max} of the reaction yields $M_{\text{gluconic acid}}/\text{min}$, which corresponds to a of one mole of $M_{\text{gluconic acid}}/\text{min}$. Therefore it is directly calculable to estimate the active unit by multiplying the reaction volume.

Theoretical unit CS-enzymes in hydrogel

$$U_{\text{theoretical}} = \frac{\text{initial theoretical units in channel} \times \text{coupling efficiency}}{\text{volume of hydrogel}}$$

Active units of CS-enzymes in hydrogel gel based on V_{max}

$$U_{\text{CS}-\text{Urs, active}} = (V_{\text{max}} \times 2)\frac{M_{\text{NH}_3}}{\text{min}} \times \text{Volume of hydrogel}$$

$$U_{\text{CS-GOx, active}} = (V_{\text{max}})\frac{M_{gluconicacid}}{\text{min}} \times \text{Volume of hydrogel}$$

Fraction of active units

$$\frac{\text{active unit}}{\text{initial unit}} \times 100\%$$

Chapter 4

Result and Discussion

4.1 Concept of fabrication design

To perform electrodeposition of chitosan, a pair of electrodes is required to inject a current into the polymer solution and trigger the gelation process. Therefore, the integration of electrodes into the microfluidic channel is the first step to be considered.

An electrodes array was manufactured to demonstrate the electrodeposition of chitosan in parallel. The platform was manufactured on a silicon substrate. The dimension of this platform is not compatible with the target NMR microdetector, as the platform is primarily intended for an exploration of chitosan hydrogel electrodeposition parameters and their fine tuning. Further details for the preparation of such experiments are clarified in section 3.4.1.

After establishing the optimal parameters for electrodeposition using the array, integrated electrodes within a single microfluidic channel were produced, which are compatible with the NMR microdetector. NMR is a sensitive tool, especially when metal elements are introduced into the magnet. The additional functionalities in the fabricated system pose a challenge to achieve a high resolution of the signals. To perform electrodeposition, a two-electrode system in contact with the chitosan solution is required to generate a local increase in pH with an applied current, thereby causing local deposition of the chitosan hydrogel. This relatively simple process is a convenient test platform for exploring electrode integration into NMR-compatible fluidics: both the change in solution pH and the gel deposition itself can be monitored by NMR spectroscopy. The challenge of obtaining high quality spectra whilst metal electrodes are within the sensitive NMR detection volume can then be addressed, including the effect on both NMR static and excitation magnetic field homogeneities, as well as the insertion of additional noise to the signal. The details for experiments setup are given in section 3.3.

4.2 Electrode array microfabrication

Electrodeposition (ED) is a powerful method with which one can control the assembly of a chitosan hydrogel with spatio temporal control. A multi-layered assembly of chitosan based on temporal variation of the applied current has been demonstrated in bulk solution[101–103]; here, the assembly is demonstrated on a lithographically defined electrode with the additional flexibility that each layer can possess a unique chemical identity. Chitosan is a polymer with several desirable properties, two of which were exploited in this work. The first is the broad variety of chemical functionalisation opportunities that exist[104, 105] and the second is the reversible gelation driven by control over the solution pH. Taken together and using a multi-step interrupted gelation methodology[106], chitosan layers of different chemical identity were assembled with spatial control by ED. Sequential ED was performed using electrode array microfabrication as shown in Figure 4.1, which shows (a) the dimensions of the array electrodes and (b) the visualization of the deposition of labelled chitosan with and without fluorescent emission light.

4.2.1 Sequential ED of Chitosan

Pre-modified Chitosan: As shown in Figure 4.2a and b, the hydrogel thickness was observed to linearly increase as a function of the number of deposition steps, up to 10 µm in 10 steps, each step lasting 60 seconds. This is in agreement with the result of Yan *et al.* who demonstrated linear gel growth up to 50 depositions steps[101]. The thickness of a single deposition can be controlled down to 0.5 µm although this measurement was at the limit of the mechanical profilometer resolution. Importantly, the in-plane resolution of the deposited film is limited only by the definition provided by the photolithographic process used to fabricate the electrodes.

Figure 4.2d plots the fluorescence intensity as a function of chitosan gel thickness after each of 5 deposition steps (Figure 4.2c). Film thickness linearly correlates to the fluorescence intensity of dye-labelled chitosan hydrogels.

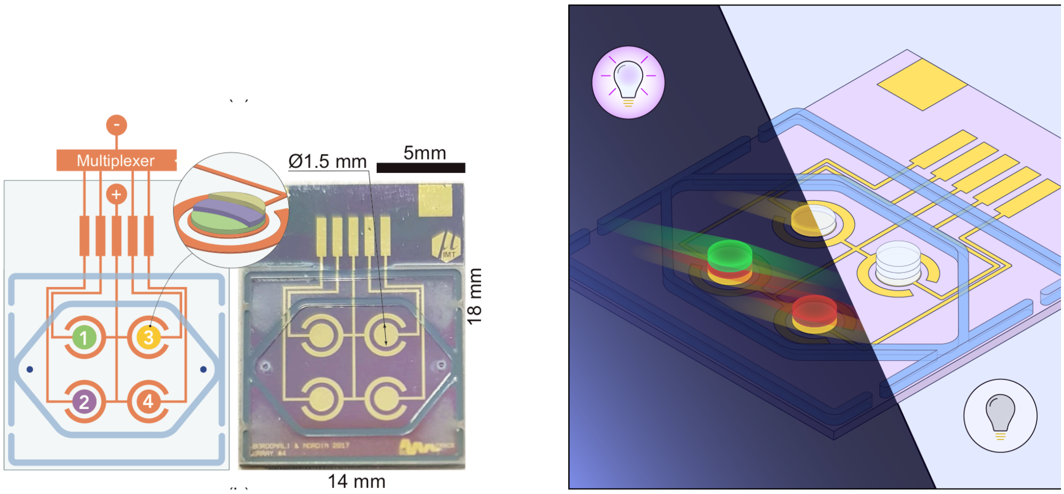

(a)

(b)

Figure 4.1 – (a) The dimensions of the 2 × 2 electrodes array (Reprinted with permission from [107] with a license number 4854671375573) and (b) the visualisation of the independent electrodeposition of chitosan functionalised with QDs (with and without fluorescent emission).

With this correlation, the thickness of deposited stack can be estimated without physically accessing the hydrogel.

Post-modified Chitosan: The first step in the chemical modification protocol was to determine the degree of deacetylation (DA) of chitosan. This was done using the ^{1}H NMR method reported by Hirai *et al.* [108], with the resulting DA = 0.75 (NMR spectrum in Figure 4.3). We note that this is in contrast to the stated DA = 0.85 given by the supplier, and thus suggest that the DA should always be experimentally determined for each chitosan batch before use. A series of chemical modifications were performed using a dicarboxylic acid functionalised PEG and the generation 0 (G0) dendrimer PAMAM. The specific molar ratios tested are given in Table 4.1. All coupling chemistry was done via carbodiimide/N-hydroxysuccinimide (EDC/NHS) activation of the necessary carboxylic acid in a solution of 10 mM PBS buffer at pH 5.5. The EDC/NHS coupling chemistry was chosen for two reasons: first, all reactions were done in the aqueous phase; and second uncontrolled cross-linking could be avoided by limiting the EDC/NHS molar equivalents.

1. Coupling to PEG: In the first step, one of the two carboxylic acid groups (COOH-PEG-COOH) of the PEG molecule were activated by using 0.5 molar equivalents of EDC/NHS relative to PEG, which was then added to

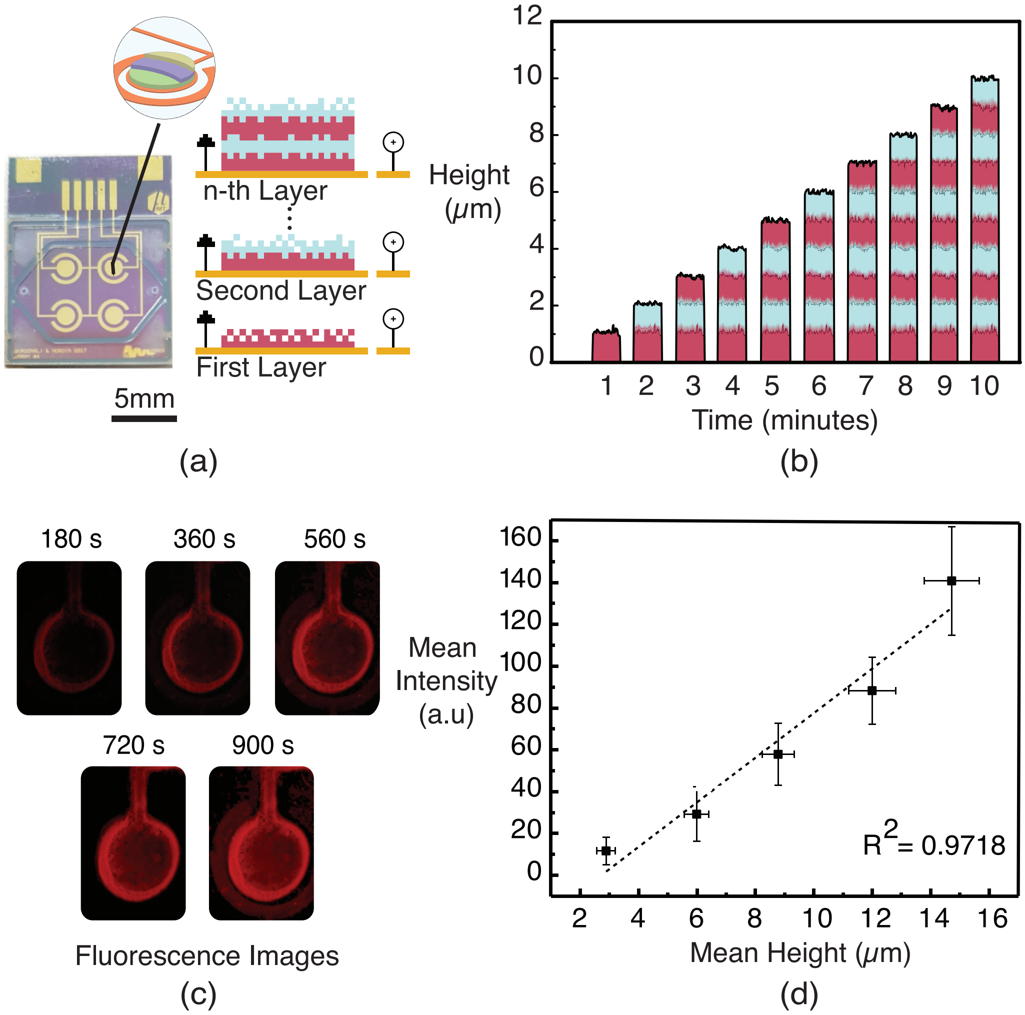

Figure 4.2 – (a) Left: Electrodes array. Right: Schematic drawing of sequential electrodeposition of chitosan. (b) profile plot for a 10-step sequential electrodeposition of chitosan over a 10 minutes total deposition time. Colour is meant to highlight the fact that each layer is added on top of the previous layer. (c) Fluorescence images and (d) Mean fluorescence intensity over the electrode area versus gel height as measured by profilometry. A total of five hydrogel layers of QD-labelled chitosan ($\lambda_{emission} = 645\,\text{nm}$) were assembled. (Reprinted with permission from [107] with a license number 4854671375573).

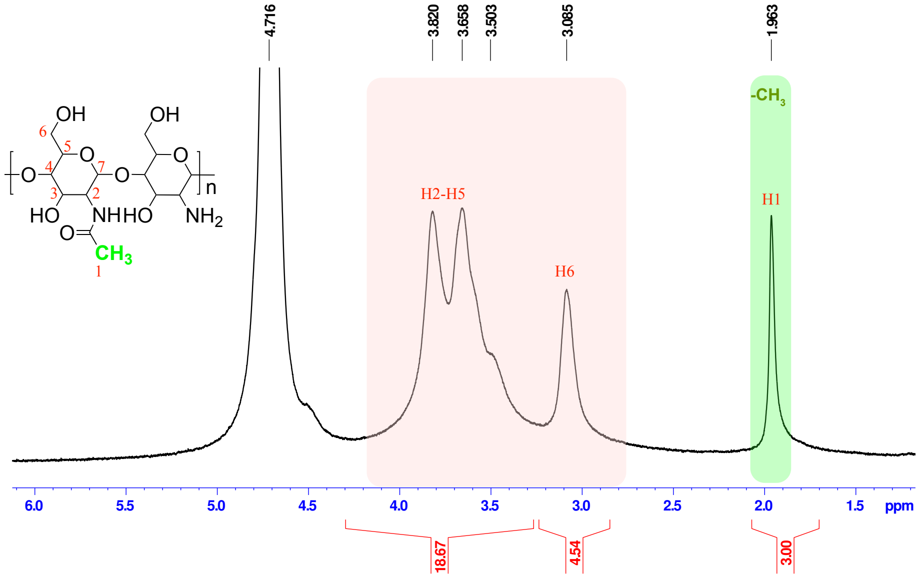

Figure 4.3 – ^{1}H NMR spectrum of chitosan, with 75% deacetylation. (Reprinted with permission from [107] with a license number 4854671375573).

the chitosan solution to generate CSPEG. After purification, CSPEG was then activated prior to adding the required molar equivalent of PAMAM to generate CSPEG-PAMAM. The resulting degree of substitutions (DS), as determined by ^{1}H NMR and potentiometric titration, are given in Table 4.1. An exemplary ^{1}H NMR spectrum and titration plot are given in Figure 4.4 and Figure 4.5, while data for all molar ratios are provided in the Appendix (titrations:Appendix A Figure A.1, NMR spectra: Appendix B Figure B.1 - Figure B.5).

Integration of the ^{1}H NMR signal intensities and identification of the potentiometric inflection points for the chitosan pre- and post-modification permitted orthogonal measures of the DS. As revealed in Table 4.1, the DS agreed very well for all molar ratios tested as measured by the two methods. When the PEG molar ratio was ≥ 1, the DS was 0.77 ± 0.03 and 0.70 ± 0.07 as determined by NMR and titration, respectively. The calculated molar ratios from NMR spectroscopy may be slightly overestimated due to a broad signal contribution to the integrated intensities. The PEG DS could be controlled as observed in the 1:0.5 molar ratio case; in all cases, the coupling yield was on the order of 70-75% of either the total available chitosan amine group (NH_2) in the case of PEG molar excess, or of the added PEG in the case of submolar quantities.

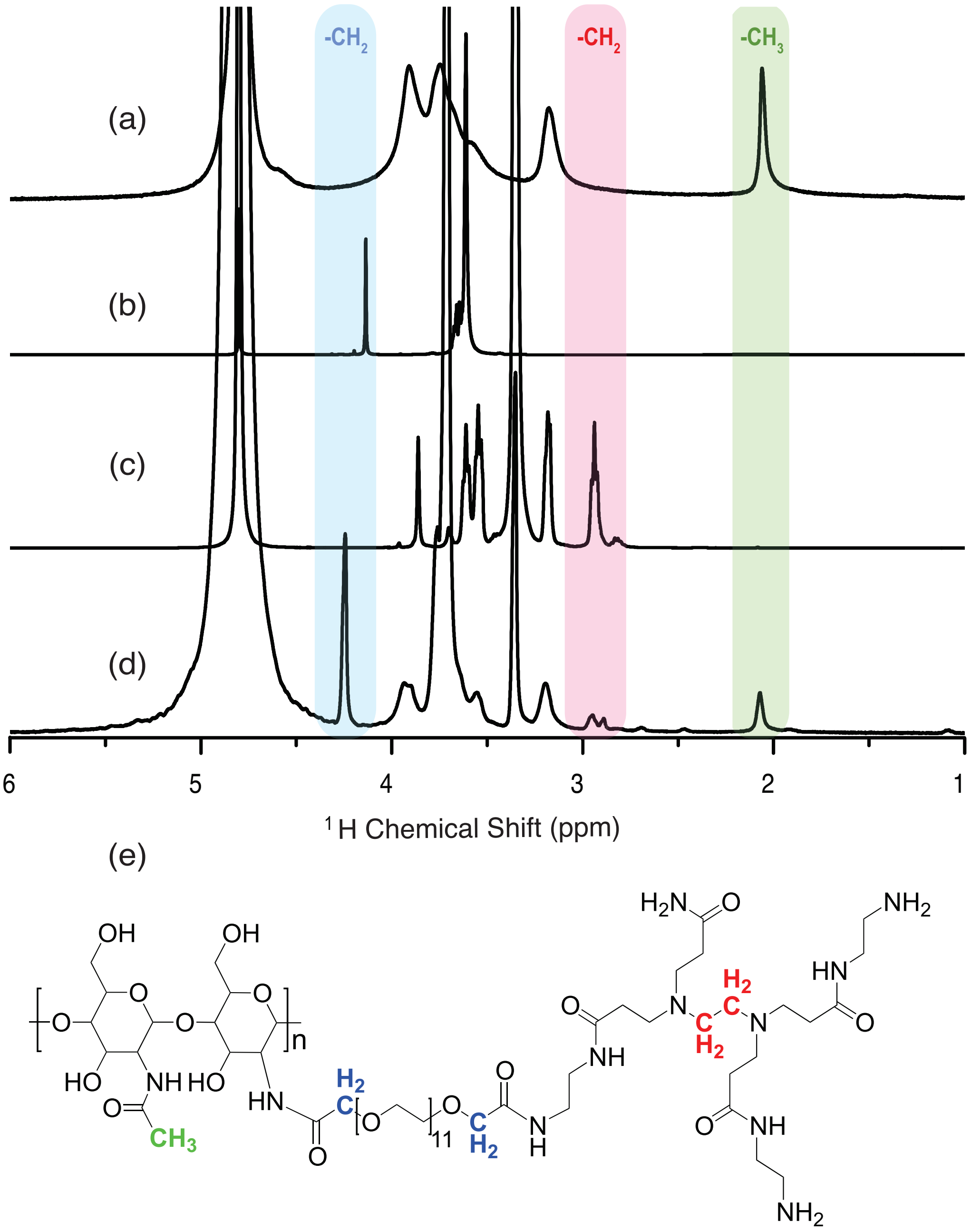

Figure 4.4 – ^{1}H NMR spectra. From top to bottom: chitosan (a), PEG (b), PAMAM (c), and an example spectrum of product CSPEG-PAMAM for the reaction condition 1:1:1 (d). The assigned signals used for quantification are highlighted by the coloured bands, with corresponding chemical assignment given in (e). Quantified reaction yields are given in Table 4.1. Spectra for the additional reaction conditions can be found in the Appendix B (B.1-B.5). (Reprinted with permission from [107] with a license number 4854671375573).

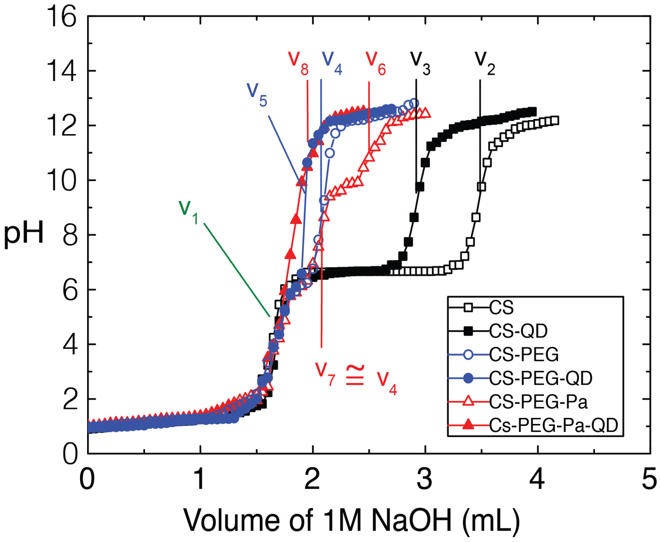

Figure 4.5 – Titration of CS pre- and post-modification (molar ratio 1:1:1 CS:PEG:PAMAM). Analysis of the inflection points permits estimation of QD coupling efficiencies. The titration was performed for individual components. (Reprinted with permission from [107] with a license number 4854671375573).

2. Coupling to PAMAM Dendrimer: It was observed that the DS for PAMAM coupling was always significantly lower than that for PEG. The PAMAM DS was comparable to results obtained for G5 PAMAM[109], or G1-3 PAMAM[110] depending on the coupling chemistry used. It is expected that with smaller generations, DS should increase[109, 110]. The decreased yield can be explained by the pH-dependence of the EDC/NHS chemistry - it is the amine group that couples to the NHS-activated carboxylic acid. The pKa's for the NH_2 from CS and PAMAM are 6.3 and 9.2[111], respectively, meaning that at pH 5 (the pH at which all reactions were performed) the population of NH_2 vs. NH_3^+ was 3 orders of magnitude greater for chitosan than PAMAM. It should be noted that the DS of PAMAM can be improved by exploring alternative coupling chemistries[112, 113]. The final chemical modification that was applied to chitosan and its modified variants was QD labelling. Titration results revealed that the DS was 30% for chitosan pre-modification, and for CS:PEG:Pa (molar ratio 1:1:1, Figure 4.5). Quantum dots (QD) coupling efficiency could be estimated by taking fluorescence intensity ratios of the modified and unmodified chitosan 4.1,

$$\frac{I'}{I} = \frac{\epsilon' A_{\text{CS-PEG-PAMAM}} + \epsilon'' A_{\text{CS-PEG}}}{\epsilon A_{\text{CS}}} \tag{4.1}$$

Theoretical	Experimental	
	^{1}H NMR	Titration
1:1:1	1:0.81:0.11	1:0.75:0.09
1:2:2	1:0.74:0.06	1:0.61:0.06
1:1:0.5	1:0.78:0.13	1:0.70:0.09
1:1:2	1:0.76:0.20	1:0.75:0.13
1:0.5:0.5	1:0.53:0.03	1:0.43:0.05

Table 4.1 – Molar ratios of CS, PEG, and PAMAM (CS:PEG:PAMAM)

where I' is the intensity obtained for a sample of CS-PEG-PAMAM-QD taking into account QD coupling to both PAMAM and unreacted CS-NH$_2$ groups, I is the intensity obtained for CS-QD, and ϵ and ϵ' are the QD coupling efficiencies to CS and modified CS, respectively; ϵ'' is the QD coupling efficiencies to unreacted CS-NH$_2$ groups. The coupling efficiencies are defined as:

$$\begin{aligned} \epsilon &= \tfrac{A_{\text{CS}}-A_{\text{CS-QD}}}{A_{\text{CS}}} \\ \epsilon' &= \tfrac{A_{\text{CS-PEG-PAMAM}}-A_{\text{CS-PEG-PAMAM-QD}}}{A_{\text{CS-PEG-PAMAM}}} \\ \epsilon'' &= \tfrac{A_{\text{CS-PEG}}-A_{\text{CS-PEG-QD}}}{A_{\text{CS-PEG}}} \end{aligned} \tag{4.2}$$

where

$$\begin{aligned} A_{\text{CS}} &= v_2 - v_1 \\ A_{\text{CS-QD}} &= v_3 - v_1 \\ A_{\text{CS-PEG}} &= v_4 - v_1 \\ A_{\text{CS-PEG-QD}} &= v_5 - v_1 \\ A_{\text{CS-PEG-PAMAM}} &= v_6 - v_7 \\ A_{\text{CS-PEG-PAMAM-QD}} &= v_8 - v_5 \end{aligned}$$

using the labelling scheme provided in Figure4.5 for the volumes v_i. A first approximation assumes the coupling efficiencies to be equal, yielding $I'/I = 0.49$.

The I'/I value as determined by fluorescence spectroscopy was 1.570 ± 0.002 (Figure 4.6) From this, the calculated coupling efficiencies were $\epsilon = 30\%$ and $\epsilon' = 85\%$. ϵ'' can be estimated by the fluorescence intensity ratio between CS-QD and CS-PEG-QD, which is 1.75, and noticing that

$$\frac{I_{\text{CS-QD}}}{I_{\text{CS-PEG-QD}}} = \frac{\epsilon}{\epsilon''(1 - \text{DS}_{\text{CS-PEG}})} \tag{4.3}$$

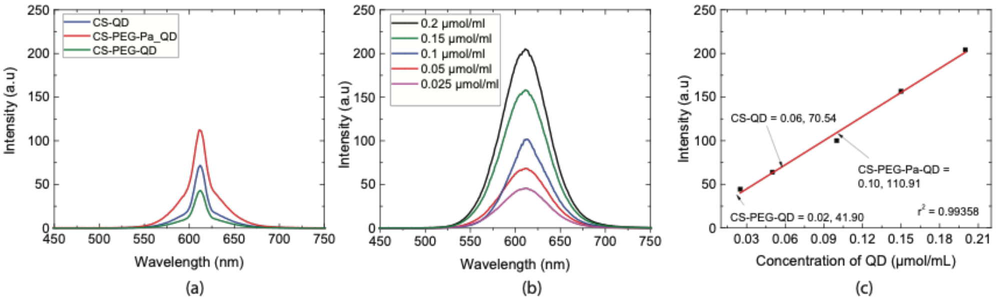

Figure 4.6 – (a) Fluorescence spectra of QD after coupling to both CS and its modified variants (CS:PEG:PAMAM molar ratio 1:1:1); (b) spectra and (c) mean intensities of five calibration solutions of QD prepared at the concentrations given in the legend. QD emission wavelength was 610 nm and the excitation wavelength 310 nm in all cases. (Reprinted with permission from [107] with a license number 4854671375573).

where we used the DS as obtained by titration for $DS_{\text{CS-PEG}}$. Solving for ϵ'', equation 4.3 yields $\epsilon'' = 69 \pm 3\%$. See Figure 4.7 for a pictorial representation of coupling efficiencies. These values correspond well with the coupling efficiencies calculated directly from the titration data ($\epsilon = 31 \pm 2\%$ and $\epsilon' = 86 \pm 6\%$ $\epsilon'' = 61 \pm 6\%$). Plugging the values for efficiency factors into Eq. 4.1 we made a conservative estimate of the expected fluorescence intensity ratio, 1.20.

Interestingly, the coupling efficiency to the modified CS was higher than for the unmodified CS. This could be attributed to the first chemical modification, PEG coupling. By introducing the highly soluble, flexible PEG moiety to the chitosan backbone, the accessibility to the NH_2 groups could have increased and thus react with the activated QD.

In Figure 4.8a, four deposition experiments were conducted, one on each of the independent electrodes. Visualisation of the resulting hydrogel was possible by using QD-labelled chitosan except in one case (electrode 3), on which unlabelled chitosan was deposited to act as a background fluorescence control. For each deposition, the following process was performed: the electrode array was exposed to a 1.0 wt% chitosan (or QD-chitosan) solution, electrodeposition was performed by applying 3 A/m^2 current applied for 300 s on the target electrode (as previously described [114–116] and finally excess chitosan was removed by thoroughly flushing the system first with PBS buffer and then with DIW. After the entire assembly was completed, fluorescence microscopy was performed after the excess DI water was removed by gently flushing the channel with N_2 gas.

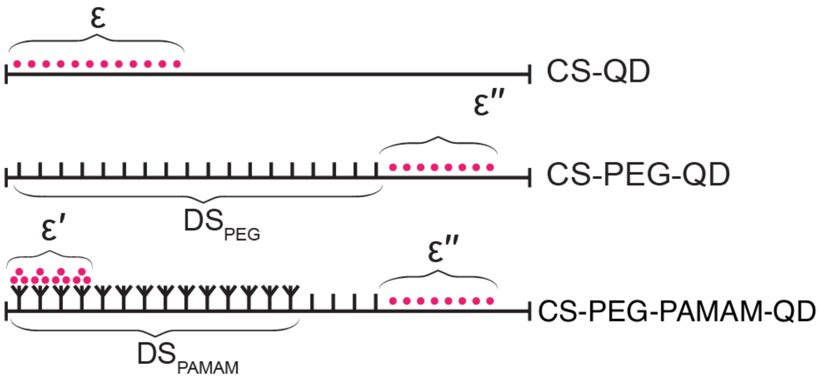

Figure 4.7 – Schematic illustration of relevant terms entering equation 4.3. QD coupling efficiency is represented by the red dots populating part of a full CS chain. PEG substitution is indicated with vertical lines. PAMAM-functionalized PEG sites are represented by branching trees. The scheme is a realistic representation of coupling efficiencies for a solution of modified CS with a 1:1:1 CS:PEG:PAMAM molar ratio, but not of the modification distributions along the CS chain. (Reprinted with permission from [107] with a license number 4854671375573).

By this sequential deposition method, the composition of the hydrogel on each electrode could be controlled individually. Specifically, a single CS-QD$_{red,\lambda=645\,\mathrm{nm}}$ layer was deposited on Electrodes 1, 2 and 4, an additional layer of CS-QD$_{orange,\lambda=576\,\mathrm{nm}}$ was deposited on Electrodes 2 and 4, and a final layer of CS-QD$_{green,\lambda=525\,\mathrm{nm}}$ was deposited on Electrode 4. The electrodeposition parameters were identical in all cases, and thus the height of each layer is equivalent. In the absence of emission filters, it was observed that the total fluorescence intensity increased with each deposited layer (Figure 4.8a). The three emission wavelengths originating from the three individually labelled chitosan layers could be clearly visualized by using quasi-ideal transmission band-pass filters centred at 532 nm, 560 nm, and 700 nm, respectively.

ED of QD labelled CS, CSPEG, and CSPEG-PAMAM was performed (Figure 4.8b). Two important points could be identified from this experiment. First, the electrodeposition time required to achieve the same hydrogel thickness decreased by ~50% for CSPEG and CSPEG-PAMAM relative to CS. This result is in agreement with the electrochemically driven neutralization mechanism for hydrogel deposition[117]. The depletion of NH_2 groups in chitosan after coupling to PEG results in an equivalent decrease in the required OH^-, and therefore e^-, to generate a hydrogel of equivalent thickness in comparison with the unmodified chitosan. Second, the decrease in QD coupling to CSPEG could

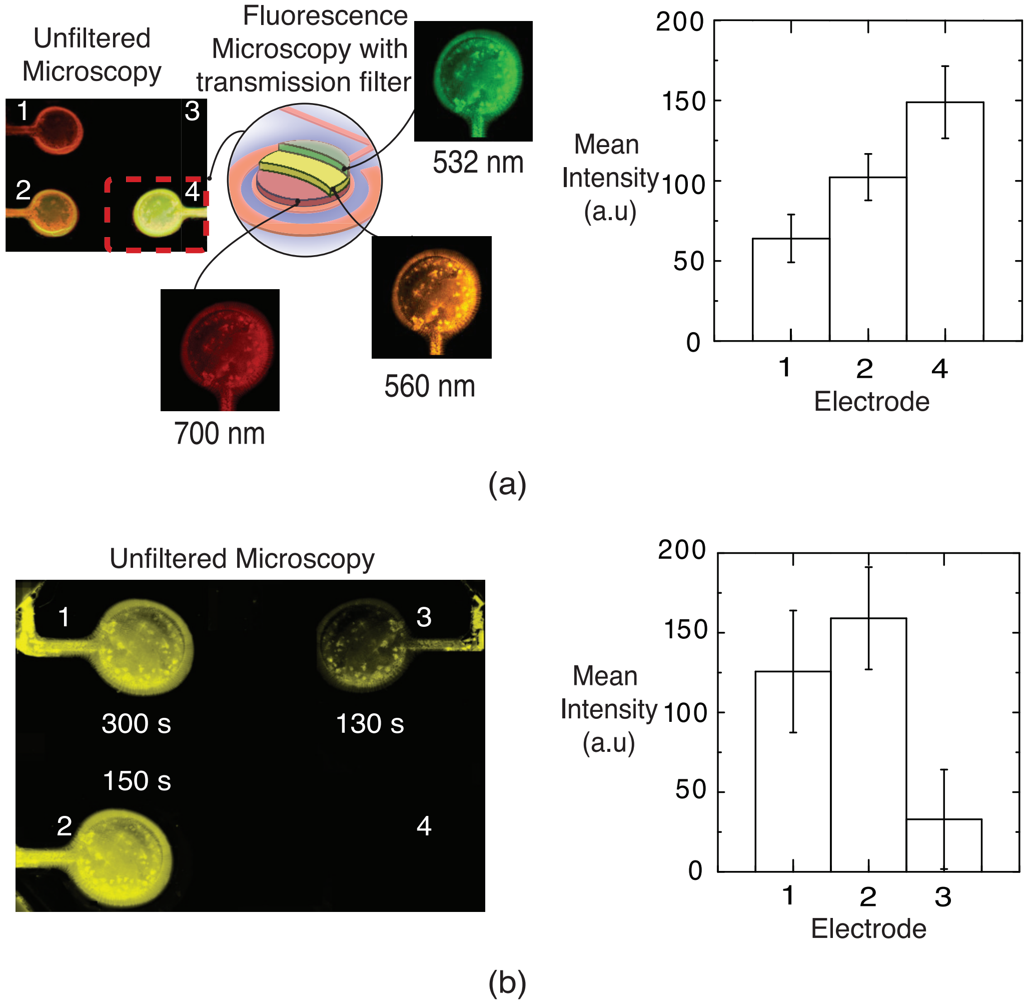

Figure 4.8 – Modified chitosan ED on an electrode array in the closed configuration.(a) Fluorescence intensity for sequential ED of chitosan on a set of electrodes in a microfluidic channel: Electrode 1 = 60 ± 10, Electrode 2 = 100 ± 10 and Electrode 4 = 150 ± 20, respectively mean fluorescence intensity ± standard deviation. Using the appropriate transmission filter, the three chitosan layers deposited on Electrode 4 can be individually identified. Coupling chemistry with CdTe QDs allows to visualize the hydrogel layers. [Chitosan] = 1.0 %w/v, current density = $3\,\mathrm{A/m^2}$, deposition time / layer = 180 s. Each data point represents the mean value, with the standard deviations for intensity and height given by the error bars and (b) Fluorescence intensity for a single electrodeposition of CS (electrode 1 = 130 ± 35), CSPEG-PAMAM (electrode 2 = 160 ± 30) and CSPEG (electrode 3 = 35 ± 30) coupled to QD (molar ratio 1:1:1). The deposition time for the various samples was adjusted to give the same thicknesses of deposited hydrogel within the range 4 µm–4.5 µm. (Reprinted with permission from [107] with a license number 4854671375573).

be recovered after further PAMAM modification as observed by the recovery in fluorescence intensity. Indeed, the $I'I$ ratio can be calculated to be 1.3 ± 0.4, agreeing qualitatively with the expected coupling efficiencies discovered from titration and spectroscopy data.

4.3 Integrating with Helmholtz NMR microdetector

With a similar workflow as the previously manufactured electrode, an array of elecrtodes was developed and used as a platform that to tested and fine-tune parameters for the immobilisation of substrates, allowing us to identify and quantify the active functional groups involved in the process of formation of the hydrogel. The dimensions of the platform do not fit the NMR microdetector. Therefore, a programmable microdevice integrated into the NMR microdetector is required to perform a pre-test under the NMR spectrometer. A pair of planar electrodes integrated into the microfluidic channel was produced using glass as the upper and lower wafers. Glass was chosen because the material does not generate a background signal from the NMR. The materials used to manufacture the microfluidic channel insert have a good value of magnetic susceptibility, close to that of water, such as Ordyl, glass and SU-8[118, 119]. As an electrode material, copper would have been a better choice than gold due to its relative magnetic susceptibility with respect to water. Nevertheless, gold was chosen as electrode material for the following reasons: i) the value of the standard electrode potential (SEP) of gold is higher than that of copper, i.e., 1.69 V for gold and 0.339 V for copper;[120, 121] ii) copper oxidation limits the lifetime of the electrodes, especially with thin film electrodes; iii) in the case of chitosan deposition, copper ion migration leads to metal particles trapping in the gel[122].

The effect of the metal electrodes on the static field B_0, the RF field B_1 and on the resistance dominated detector noise was investigated. The parameters were processed to derive estimates of RF field homogeneity, sensitivity and spectral resolution of the signal. For this purpose, two electrode configurations were considered and all results were compared to a reference insert without electrodes.

The electrode-free reference insert is a simple microfluidic channel defined in SU-8 photoresist. The channel height was 90 µm and was sandwiched between two glass wafers, each having a thickness of 210 µm. Starting from this basic microfluidic channel structure, various electrode configurations were chosen with respect to the direction of the B_1 field. From a fabrication perspective, planar disk electrodes in the zx-plane were the easiest to introduce in the microfluidic channel. A working electrode was positioned within the field of view of the Helmholtz detector, and the counter electrode was placed 5 mm away within the microfluidic channel. The thickness of the working electrode determined the current induced inside the electrode, and hence also the magnetic field perturbation and the dissipated RF power.

Two proposals for the design of the electrode geometry were made. The first design, a planar electrode with a thickness of up to 30 nm, was proposed in which the hydrogel grows vertically according to the time of deposition. The second design was proposed to have sidewall electrodes where the hydrogel grew horizontally. It was chosen because it minimises the total electrode surface being intercepted by the B_1 RF field. Two high aspect-ratio metallic walls were designed as the active electrodes in the sidewalls of the microfluidic channel, i.e., along the yz-plane. The width of the electrodes was set to 30 µm to ensure their mechanical stability, while minimising the cross-section to the B_1 wave front. Further details are described in next section.

4.3.1 Criteria for the position of the working electrodes

A pair of electrodes is required for the ED of chitosan. The aim of this study is to bring this platform together with the deposited substrate into the magnet so that a high signal resolution is achieved. Therefore, some criteria regarding the position of the immobilised samples need to be considered:

1. The position of the electrode may be either inside or outside the detector - spectral resolution may be affected by the presence of the electrode in the detection volume.

2. The thickness of the metal electrode when it overlaps with the detector should be as low as possible, to ensure that the B_1 field is homogeneous, to achieve homogeneous excitation of the sample.

3. The area of the working electrode should be as large as possible, to deposit enough sample to overcome the limit of detection of the NMR sensor. This limit is set at $\sim 10^{13}$ molecules.

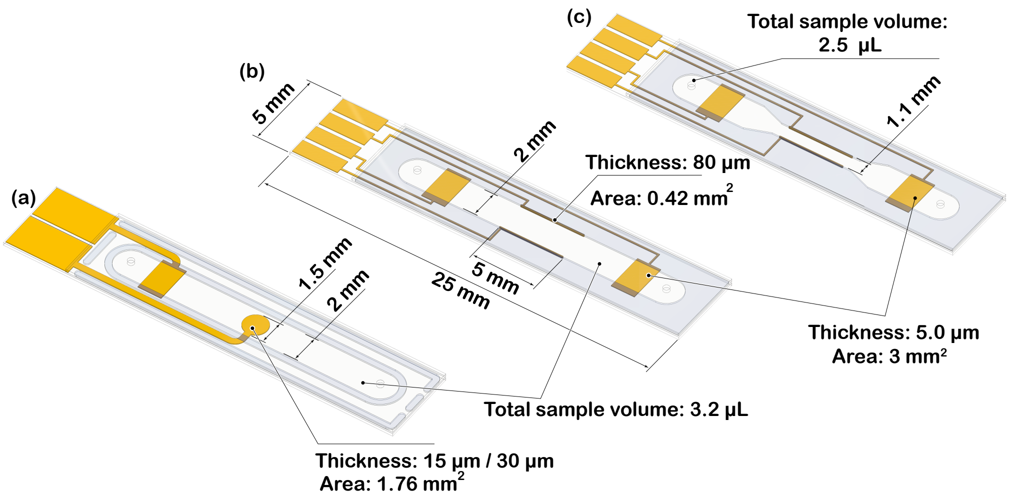

Figure 4.9 – Proposed design (a) planar, (b) and (c) sidewalls with wide and narrow channel of electrodes integrated in the microfluidic channel compatible with the NMR microdetector.

Two different electrodes integrated into the microfluidic channel were proposed and the details are as follows:

(1) Planar electrode: The specification of the electrodes has been designed so that the distance between cathode and working electrode is greater. This distance should ensure that no hydrogen gas bubbles are trapped in the hydrogel during the immersion of the electrode. During the process of immersion of the electrode in chitosan, the working electrode generates a pH gradient at which a chitosan hydrogel is formed on the surface of the electrode and hydrogen gas is generated at the same time[123, 124]. The formation of hydrogen gas bubbles would affect the magnetic field homogeneity of the deposited gel, which deteriorates the resolution of the spectra. The electrochemical reactions that occur during electrodeposition are given below:[125]:

$$\text{cathode (WE):} \qquad 2\,H_2O + 2\,e^- \longrightarrow H_2 + 2\,OH^- \tag{4.4}$$

$$\text{anode (CE):} \qquad 2\,H_2O \longrightarrow O_2 + 4\,H^+ + 4\,e^- \tag{4.5}$$

The surface area of the working electrode (WE) is $1.76\,mm^2$ with a diameter of 1.5 mm. The total sample volume is 3.2 μL, but within the detector the sample detection volume is smaller than this value because the NMR-detector only covers a part of the area of WE. There are two different thicknesses of the electrode that have been sputtered. The details are discussed in section 4.3.2.

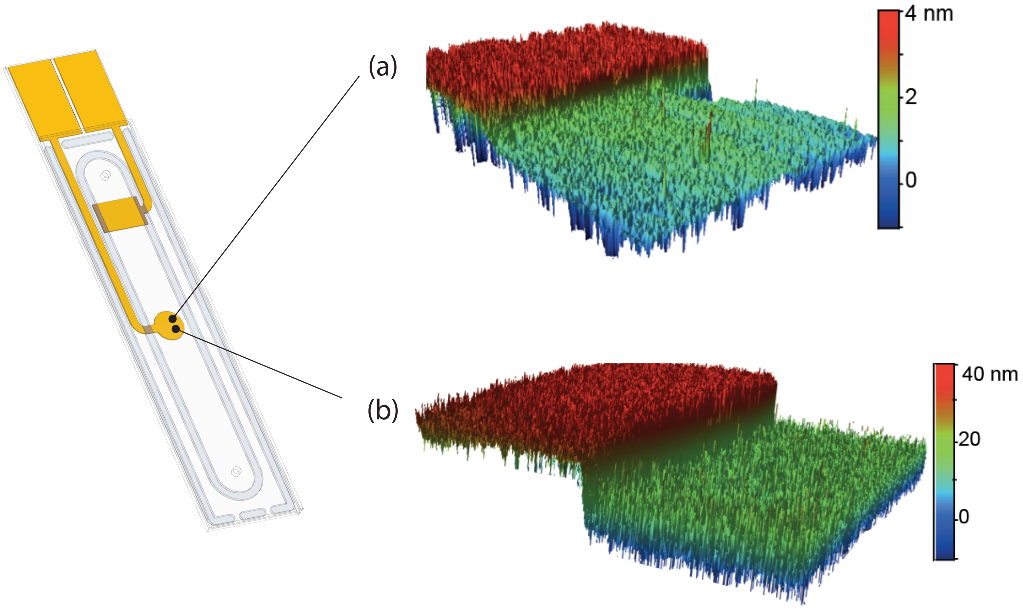

Figure 4.10 – Electrodes geometry: Profiles of (a) the 3 nm-thick planar electrode and of (b) the 30 nm-thick planar electrode, measured using white-light interferometry, showing two steps corresponding to chromium and gold PVD layers.

(2) Sidewall electrode: Two different channels were designed, a narrow channel and a wide channel. The wide channel has a total sample volume corresponding to that of the planar electrode channel, i.e. 3.2 µL and with the area of the side wall 0.42 mm^2 each. The narrow channel has a total sample volume of 2.5 µL. The purpose of having two differently sized channels is to observe the different B_1 homogeneity of the electrode when placed inside the magnet, as described in criteria number 1. A wide channel would have the same B_1 homogeneity because no electrode is placed inside the detector, while the sample area for the narrow channel inside the detector has a different B_1 homogeneity (refer to section 4.3.3 for homogeneity discussion). The distance between the side walls is 1.1 mm for narrow channels and 2 mm for wide channels. Two additional electrodes have been designed at the top and bottom of the channel to increase the electric field when two side walls of the electrodes are used as working electrodes to generate more hydrogel during the electrodeposition process.

4.3.2 Thickness of electrodes

(1) Planar electrode: The selection of the correct geometry for the working electrode is particularly critical for both the ED process and NMR spectroscopy. When performing ED of chitosan, a concurrent deposition process may intervene. Even at small current densities, the ED process can damage the electrode surfaces by migrating gold ions from the anode to the cathode. Since experiments with chitosan gel are performed under cathodic ED conditions, the anode gold electrode was grown to the thickness of 5 µm, ensuring that the surface of the anode would not be eroded within the time span of an ED experiment (max ^{1}H). No additional gold was grown on the cathode, and the thickness of the gold layer remained that of the gold seed layer evaporated on the substrate during fabrication. For fabrication details refer to section 3.1.2. A significantly thin metal layer is beneficial to the NMR measurement because the RF field is able to penetrate metal when its thickness is well below the RF skin depth for that particular material. In the case of gold, the skin depth at 500 MHz is roughly 3.4 µm. Figure 4.10a shows that the thickness of the working electrode measured with a white light interferometer has two steps corresponding to the PVD layers of chromium and gold, which give 3 nm instead of 15 nm. However, another version of the thickness in Figure 4.10b shows that 30 nm thickness was sputtered. By manufacturing sample inserts with two gold layer thicknesses for the cathode, nominally 3 nm and 30 nm, we guaranteed a minimum amount of RF penetration through the metal layer, with the goal of preserving the homogeneity of the B_1 field at the position of the chitosan hydrogel.

(2) Sidewall electrode: these designs are naturally not affected by the electroplating issue illustrated in the previous paragraph. In this case the geometry of the electrodes was chosen so that an acceptable quality of the electrodes themselves could be achieved during fabrication. Each sidewall electrode has a width of 30 µm and a height of 80 µm (Figure 4.11). These values amount to an aspect ratio of ~ 2.6, which is a low enough ratio to be able to fabricate the electrodes using common photolithographic and electroplating methods. The height of the electrodes was set to 80 µm, which is 10 µm short of the nominal channel thickness. This design choice was formulated in order to ensure that the electrode would not get contaminated by the adhesive material necessary for encapsulation during the bonding process. For fabrication details refer to section 3.1.3. Although the absence of metal structures in the detector volume

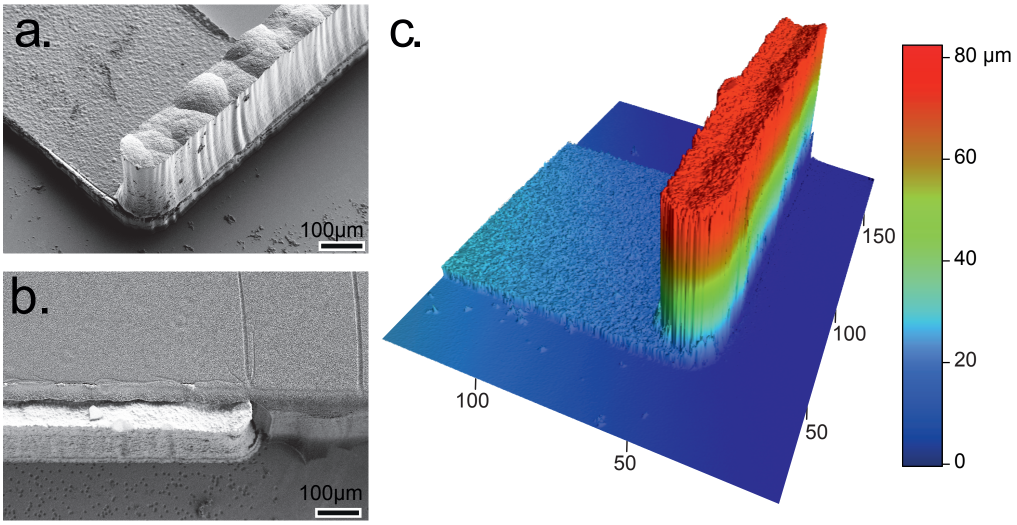

Figure 4.11 – Electrodes geometry:(a) SEM image of a sidewall electrode and its corresponding track fabricated by gold electroplating; (b) SEM image of a sidewall electrode encapsulated by SU-8, forming the channel; (c) Profile of a sidewall electrode and its corresponding track, measured using white-light interferometry.

is a drastic design improvement with respect to the planar electrodes design, the proximity of metal electrodes to the NMR detector may induce distortions in the B_1 field. For this reason, the distance between the electrodes was optimized, to take advantage of the induced eddy currents inside the electrodes, and improve the B_1 field homogeneity, as described in the following subsection.

4.3.3 Nutation experiment

The purpose of performing a nutation experiment is to determine the quality of the B_1 field, that is its homogeneity, produced at the sample position. Figure 4.12 shows the electrode configurations and their position with respect to the detection area of the NMR microdetector. In a nutation experiment, a simple one-pulse sequence is used to read out the NMR signal and the length of the single pulse is progressively increased to rotate the nuclear magnetization by an accordingly increasing tip angle. If the B_1 field is completely homogeneous, and disregarding relaxation phenomena on the time scale of the NMR experiment, the result of the experiment would be a perfect sinusoid maxing out at pulse lengths corresponding to $90°(4n+1)$, where n is a positive integer number. Therefore, for a perfectly homogenous B_1 field, we expect a unit ra-

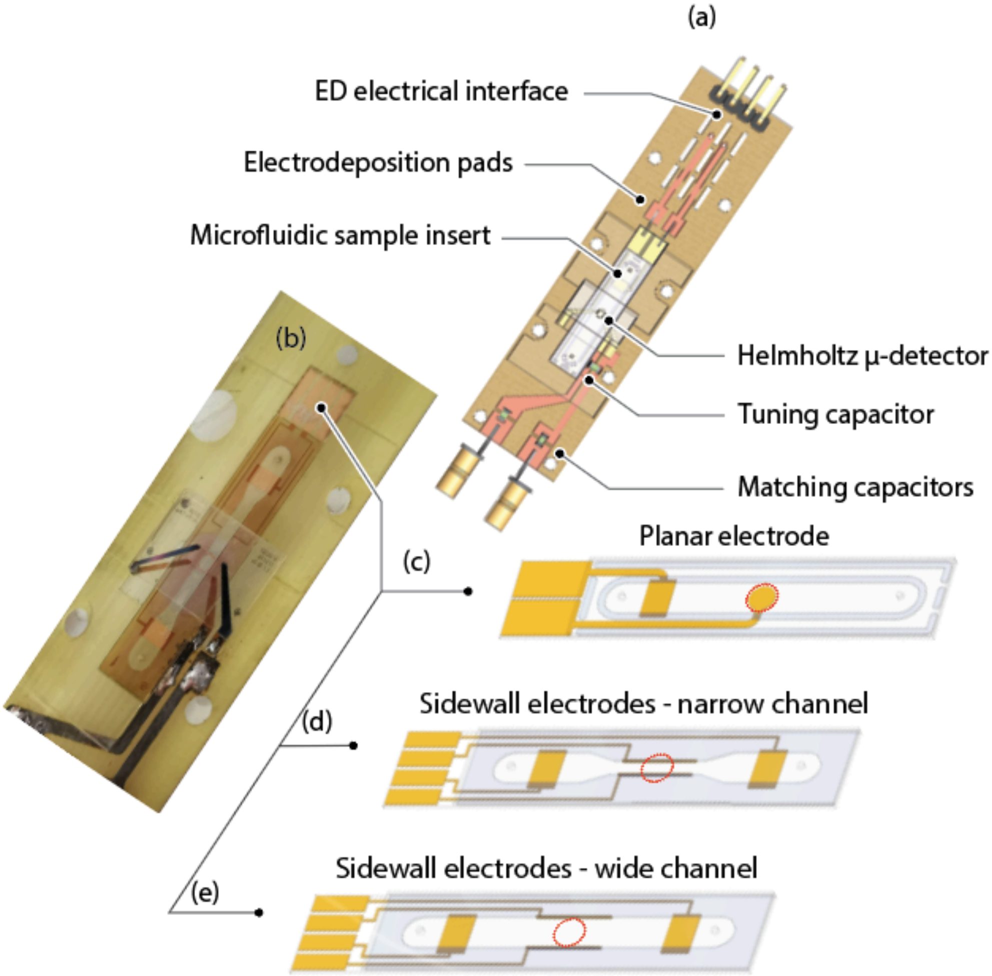
(a)
ED electrical interface
Electrodeposition pads
Microfluidic sample insert
Helmholtz μ-detector
Tuning capacitor
Matching capacitors
(b)
(c)
Planar electrode
(d)
Sidewall electrodes - narrow channel
(e)
Sidewall electrodes - wide channel

Figure 4.12 – (a) Image of a platform compatible with the NMR microdetector; (b) photograph of the insert featuring different electrode configurations, i.e. (c) planar electrode; (d) narrow channel sidewall electrode; and (e) wide channel sidewall electrodes. The red dashed line circle indicates the intended position of the NMR microdetector.

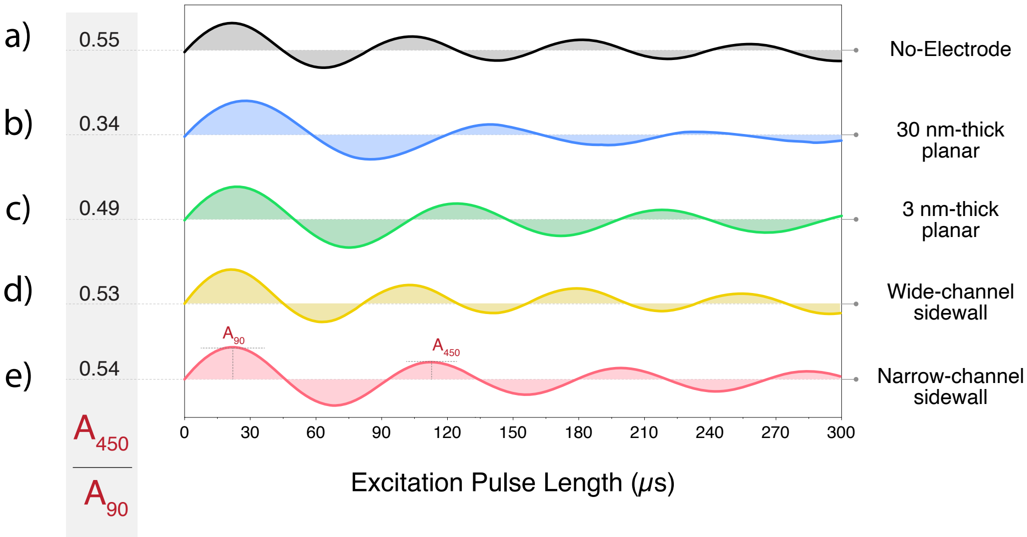

Figure 4.13 – Nutation spectra of chitosan with and without electrodes in detector.

tio between signal amplitudes at 450° tip angle and 90° tip angle. A decrease in the local maximum at 450° tip angle in the nutation spectrum indicates a non-homogeneity of the B_1 field. By comparing the ratio A_{450}/A_{90} of signal amplitudes at 450° and 90° we can qualitatively compare homogeneities of the B_1 fields produced under different experimental conditions. Namely, in the present case, we will compare estimates of B_1 field homogeneities from nutation spectra sampled with a) no electrode in the sample region, b,c) a planar gold electrode of either 30 nm or 3 nm layer thickness and d,e) sidewall electrodes in either a wide channel (larger than the detector diameter) or a narrow channel (whose width is comparable or lower than the detector diameter). The results are collected in Figure 4.13.

The plot shows the amplitude of the NMR signal recorded for pulse length between 0 and 300 µs. The signal amplitude was calculated by taking the integral of the NMR peak of a water-filled sample insert. We will compare results to the case where no electrode was present in the sample insert, and therefore at the sample position. For this configuration, a ratio $A_{450}/A_{90} = 0.55$ was found.

In the case of planar electrodes (b,c), the ratios A_{450}/A_{90} were found to be 0.34 and 0.49 for 30 nm electrodes and 3 nm electrodes, respectively. We attribute the significant signal loss for the case of 30 nm electrodes to the marked thickness of the gold metal layer, that distorts the B_1 field down to a much lower homogeneity with respect to 3 nm electrodes. Indeed, the value of A_{450}/A_{90} recorded for 3 nm electrodes (0.49) allows us to postulate that only marginally

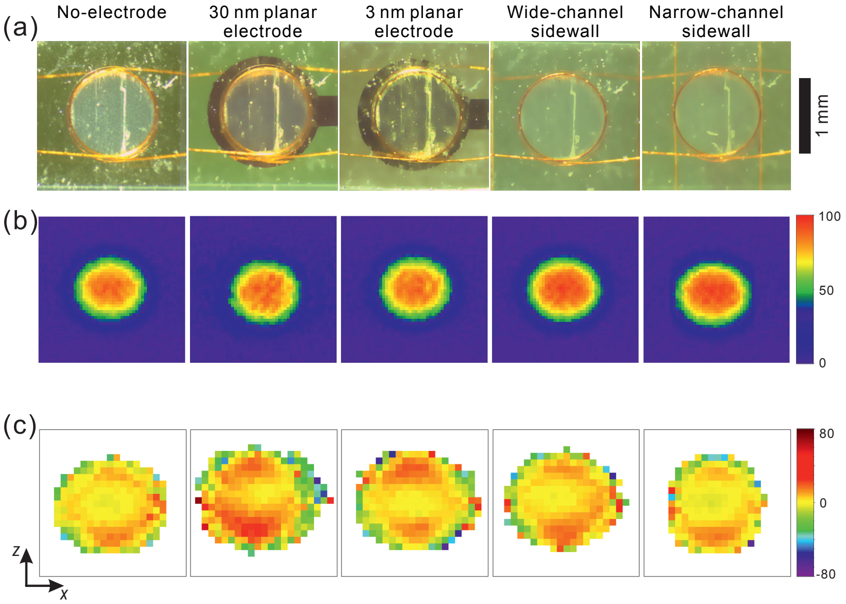

Figure 4.14 – a) Positions of the NMR detector for different types of inserts; (b) normalised distribution of the B_1 field (%) at the sample volume at 70° flip angle for each types of inserts and (c) B_0 field map at the detection zone of the coil.

significant distortions to the B_1 field are introduced by a 3 nm-thin gold metal layer.

For (d,e), A_{450}/A_{90} ratios measured with sidewall electrodes within the sample volume reflect a better homogeneity condition for B_1 when this geometry is used. Namely $A_{450}/A_{90} = 0.54$ for sidewalls on a narrow channel insert (0.9 mm wide) and $A_{450}/A_{90} = 0.53$ on a wide channel insert (2 mm wide). We infer in both cases a minimal distortion to the B_1 field produced by the NMR microcoil. The wide channel insert in particular allows to recover almost completely the homogeneity conditions found on the blank insert (no electrodes).

From these results we can postulate that favourable geometries for chitosan electrodeposition are either sidewall electrodes or a thin-metal-layer planar electrode (3 nm). Selection of the specific geometry may depend on the requirements of the electrodeposition experiment.

4.3.4 MRI Imaging for B_1 and B_0 field Homogeneity

B_1 distribution

B_1 images at a flip angle of 70° for all five experimentally verified configurations are shown in Figure 4.14 and confirm the lower homogeneity of the planar electrodes for 30 nm. To emphasise the field homogeneity, the maps are scaled to one unit. The asymmetrical distribution in the x- and z-axis of the colour maps is due to the relative direction of the B_0 and B_1 fields. For narrow channel applications, the field homogeneity is increased and then the field decreases steeply as the sample volume is limited by the metallic side wall electrodes.

$\mathbf{B_0}$ distribution

Spectral resolution of experimental NMR spectra strongly depends on the ability to correct $\mathrm{B_0}$ imperfections by using shim fields. The NMR signal of the sample for different configurations, after the optimal shim settings, were identified and are presented in Figure 4.14b and c. The *FWHM* value for TSP peak was considered as the measure for the spectral resolution.

In order to investigate the $\mathrm{B_0}$ distribution more precisely and avoid shimming influence on the results, the $\mathrm{B_0}$ maps of different configurations were collected and are plotted in Figure 4.14c. In all configurations, the detection volume was surrounded by a rim whose voxels were severely distorted due to the the partial volume effect (the sample does not fully occupy a voxel) and low $\mathrm{B_1}$ field. To calculate the standard deviation of the colour maps, a rim of one pixel was excluded to minimise the noise contribution. At the bottom and top of the detection zone, similar field distortions were observed in all the $\mathrm{B_0}$ field maps. This distortion originated from the coil windings.

The $\mathrm{B_0}$ pattern at the sensitive zone of the coil showed that the planar 30 nm electrode distorted the static field especially at the top and bottom edges of the electrode, which perfectly aligned the material interface intersections with $\mathrm{B_0}$. The ultra-thin electrodes (3 nm thickness) introduced less perturbations; however, the overall pattern appeared similar as expected. These distortions are likely introduced because of the chromium seed layer. Conversely, the narrow channel sidewall electrodes had almost no effect on the overall field pattern, except for the left and right edges where the ^{1}H NMR signal was excluded due to the presence of the electrodes. These results correlated with the measured spectral *FWHM* results.

4.3.5 $\mathbf{T_1}$ Relaxation NMR

$\mathrm{T_1}$ relaxation is one of the parameters we have considered to ensure that the FID can be collected with adequate time to obtain a good resolution of the NMR

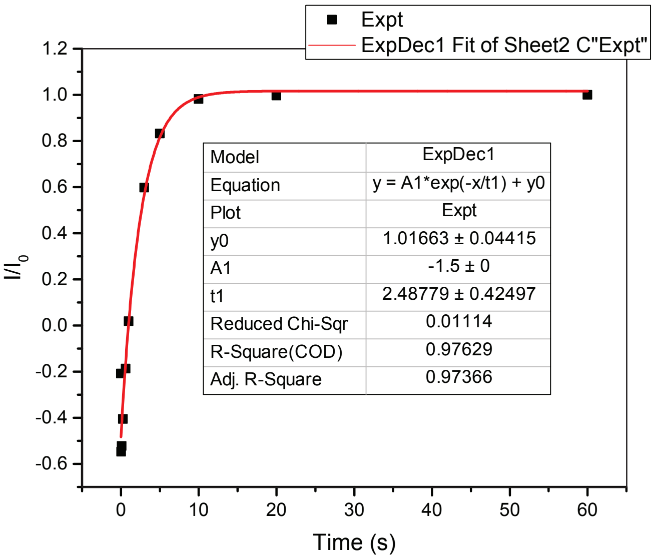

Model	ExpDec1
Equation	y = A1*exp(-x/t1) + y0
Plot	Expt
y0	1.01663 ± 0.04415
A1	-1.5 ± 0
t1	2.48779 ± 0.42497
Reduced Chi-Sqr	0.01114
R-Square(COD)	0.97629
Adj. R-Square	0.97366

Figure 4.15 – Diagram of the relative intensity of the recovery magnetization (M_z) versus time (t) for a sample of 500 mM sucrose in H_2O at 500 MHz at 27 °C. The water signal at 4.8 ppm was integrated.

spectra. Briefly, after the perturbation of the 90° radiofrequency pulse, the longitudinal magnetization (M_z) is flipped over onto the xy-plane and converted into transverse nuclear magnetization, which then begins to precess around the B_0 field at the Larmour frequency. The amplitude of the transverse magnetization decreases exponentially until a steady state is reached again, whereby the magnetization once again is completely aligned to the B_0 field. This process is called relaxation. There are two types of relaxation, longitudinal relaxation and transverse relaxation, which occur over time scales defined by the characteristic times T_1 and T_2, respectively. The T_1 relaxation, also known as longitudinal relaxation, spin-lattice relaxation or z-direction relaxation, is the process by which the longitudinal component of the magnetization returns to equilibrium (along the z-axis) over time.

T_1 relaxation is caused by energy exchanges with the local magnetic environment. This exchange is enabled by transient magnetic field fluctuations due to molecular motion, and it is most effective when said fluctuations happen at the Larmour precession frequency. In liquids solution (near room temperature), the average rates of molecular rotation are several orders of magnitude higher than at ν_0, so that only a very small fraction of the motions occur at the correct frequency, resulting in a very inefficient relaxation (long T_1)[126, 127].

500 mM sucrose was chosen as the test sample to obtain good resolution of

spectra with a standard NMR reference, 50 mM TSP. Figure 4.15 shows that the T_1 of the water signal at 4.8 ppm in a sucrose solution is 2.5 s, which gives us a recommended recycle delay (d1) of 5*T_1, 12.5 s. The d1 for the measurement was set to 10 s. In our result, there are no significant differences between d1 of 5 s and 10 s, when extracting 90° pulse width values from nutation experiments. We observed a difference of 5% in P1 for these two d1 values.

4.3.6 Sensitivity

Table 4.2 – Summary of the NMR/MRI figures of merit for performance evaluation of different inserts.

Configurations	**Experimental**			
	A_{450}/A_{90} (%)	S_{TSP} (%)	$FWHM$ (ppb/Hz)	σ_{B0}
Electrode-free	56	100	9.5 / 4.8	3.1
30 nm-thick disk	32	85	13.3 / 6.7	5.3
3 nm-thick disk	50	93	11.2 / 5.6	3.7
Wide-channel sidewall	56	100	11.4 / 5.7	3.6
Narrow-channel sidewall	54	141	11.7 / 5.9	3.5

According to the reciprocity law, for a uniformly distributed and polarised sample, the total area under an NMR peak is a measure of the average B_1 and is independent of the spectral resolution, which is influenced by the homogeneity of the static B_0 field. In Figure 4.16), the signal amplitudes were scaled so that they all had the same noise level. The mass sensitivity, defined as the average B_1 per collected noise amplitude for a unit sample volume,[128] was studied in order to compare the performance of different insert topologies. Therefore, the area under the normalised NMR spectrum collected for each electrode geometry, relative to the electrode-free case - S_{rel} - was considered as a second figure of merit.

As expected from the analytical expressions given by Zu-Rong *et al.*,[129] the thickest planar disk electrode showed the worst performance in terms of mass sensitivity - S_{rel}= 86.4 %. For all other structures except for the narrow channel sidewall configuration, the penalty to be paid in comparison with the electrode-free configuration, in terms of mass sensitivity, was <5 %. The narrow channel sidewall electrode configuration clearly outperformed all other designs. The sensitivity enhancement for the sidewall structure and 3-nm thick planar could also be observed through the nutation frequency (Figure 4.13). The value of the nutation frequency of these electrode configuration were comparable to the electrode-free insert, suggests that the presence of the vertical electrode and thin planar electrode is constructive and enhances the overall sensitivity.

Figure 4.16 presents NMR spectra of the sucrose sample collected using the different inserts. Similarly, the relative mass sensitivity of each configuration was calculated by considering the integral of the TSP signal (located at 0 ppm) normalised by that of electrode-free geometry as the reference - S_{TSP}. The results are presented in Table 4.2. These results confirm the superior performance of the sidewall and 3-nm planar thick configurations.

The challenge of introducing conductive structures for *in situ* electrochemical analyses with high-field NMR is reflected by there being only a few reports available[129–134]. Ultra-thin metallic layers, which are NMR transparent, can be achieved by rather standard MEMS techniques. On the other hand, microfabrication enables the construction of precisely oriented high aspect-ratio electrodes, which have a minimum footprint to eliminate any B_1 and B_0 distortions. Here, we have demonstrated a fabrication technique based on UV-lithography and gold-electroplating to manufacture such electrodes with an aspect ratio (height to width) of ~ 3. A further reduction of the width of the electrodes requires more sophisticated lithography techniques, e.g., 2PP, X-Ray or e-beam lithography. As an alternative, the distance between the electrodes was optimised in this work to take advantage of the B_1 field perturbation, introduced by the electrodes, and enhance the overall field homogeneity and mass sensitivity.

Since the 3-nm planar thick and sidewall electrode configurations proves to be the best compromise in terms of B_1 field homogeneity and mass sensitivity, as well as in terms of B_0 field distortion, i.e., spectral resolution, this structure was further used for the experiment of NMR in situ monitoring of chitosan electrodeposition.

4.4 Monitoring in situ electrodeposition by NMR

Pre-modified CS: Despite the reduced B_1 homogeneity, we have shown in situ hydrogel deposition observed by monitoring the NMR signal as a function of deposition time during current was running (figure 4.17). In this experiment

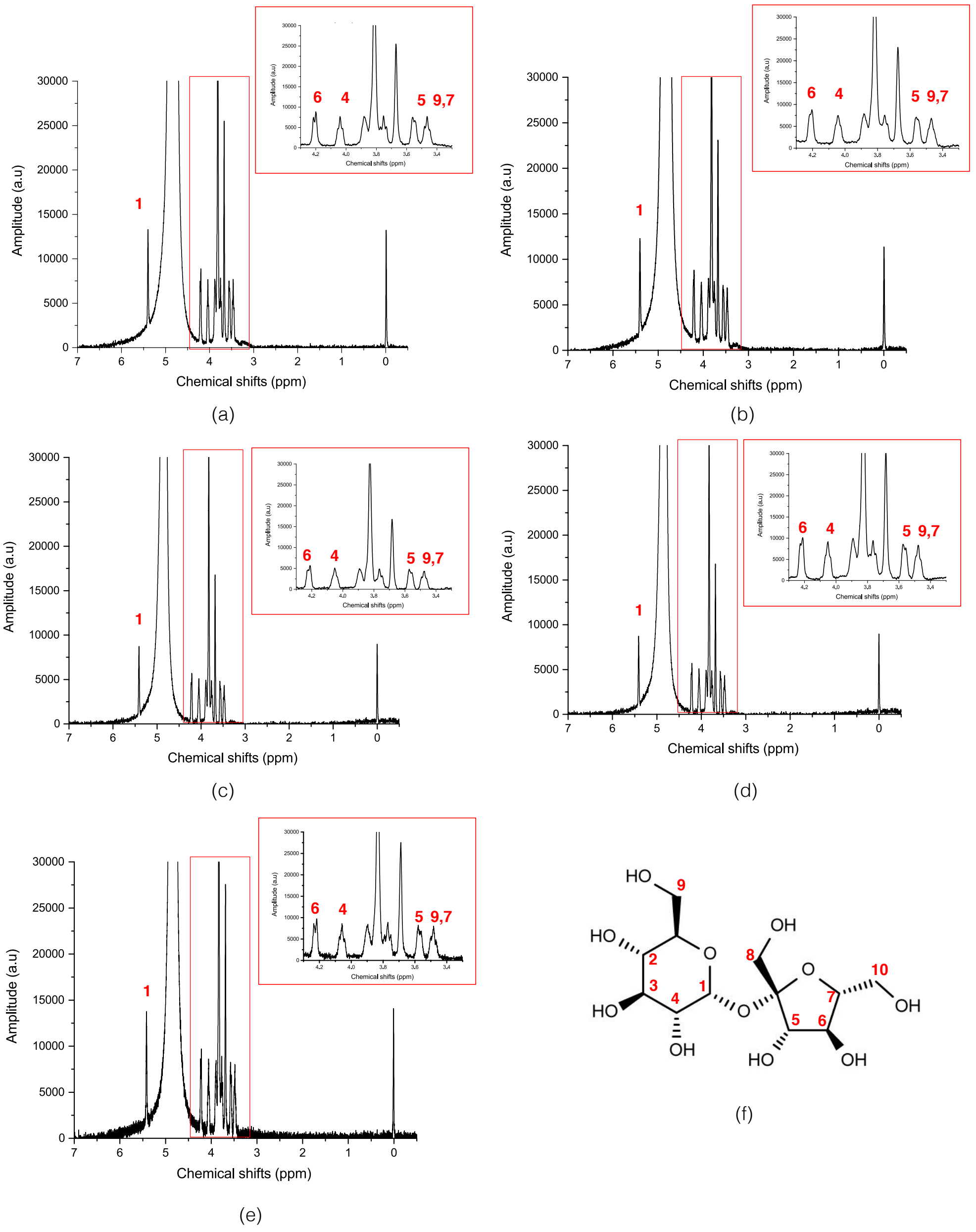

Figure 4.16 – ^{1}H NMR of sucrose for five different configurations, (a) no electrode within the detector; (b) 30 nm planar electrode; (c) 3 nm planar electrode; (d) wide channel sidewall electrode; (e) narrow channel sidewall electrodes within the detector and (f) molecular structure of sucrose. The insets provide a magnification of the sucrose region at 3.3 – 4.3 ppm.

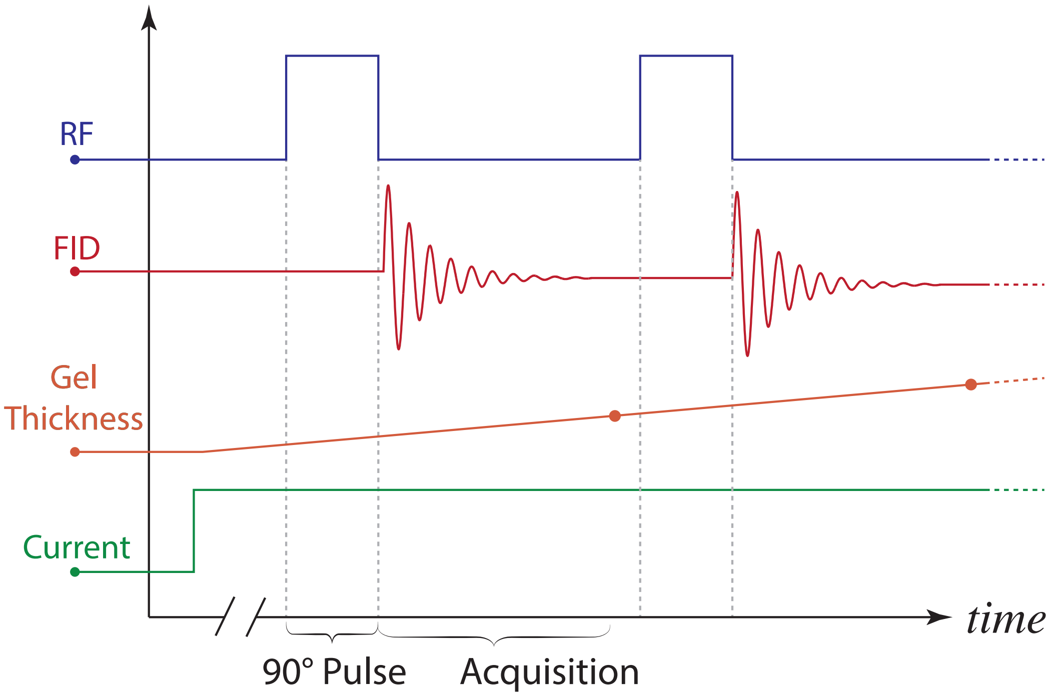

Figure 4.17 – The diagram of the NMR experiment timing during the in situ electrodeposition of chitosan.

a current density of $3\,\mathrm{A/m^2}$ over a working electrode area of $1.76\,\mathrm{mm^2}$ was used. The distance between the counter and the working electrodes was 5 mm. As shown in Figure 4.18a, the CS signals widen at 2-3 ppm (within the red range) during deposition. The widening is due to the formation of the hydrogel, which limits the molecular motion of CS molecules. The bubbles created by the formation of hydrogen gas during the electrodeposition process were dissolved by gently rinsing the chitosan solution during deposition. In addition, we observed a shift in the position of the water resonance after deposition due to the change in pH.

Modified CS: In order to confirm the result as discussed above, we have performed in situ electrodeposition of modified CS by introducing PEG. The spectra were collected after every 5 minutes of deposition up to a total of 30 minutes of electrodeposition. According Figure 4.18(d and e), it was observed that the intensity of the PEG signals at 3-4 ppm (within blue region) were unchanged, while the CS signals broaden during the deposition. This can be explained by noting that the PEG molecule did not experience constrained molecular motion. However, the chemical shift of the PEG signal shifted after the deposition and this is due to the change in pH environment.

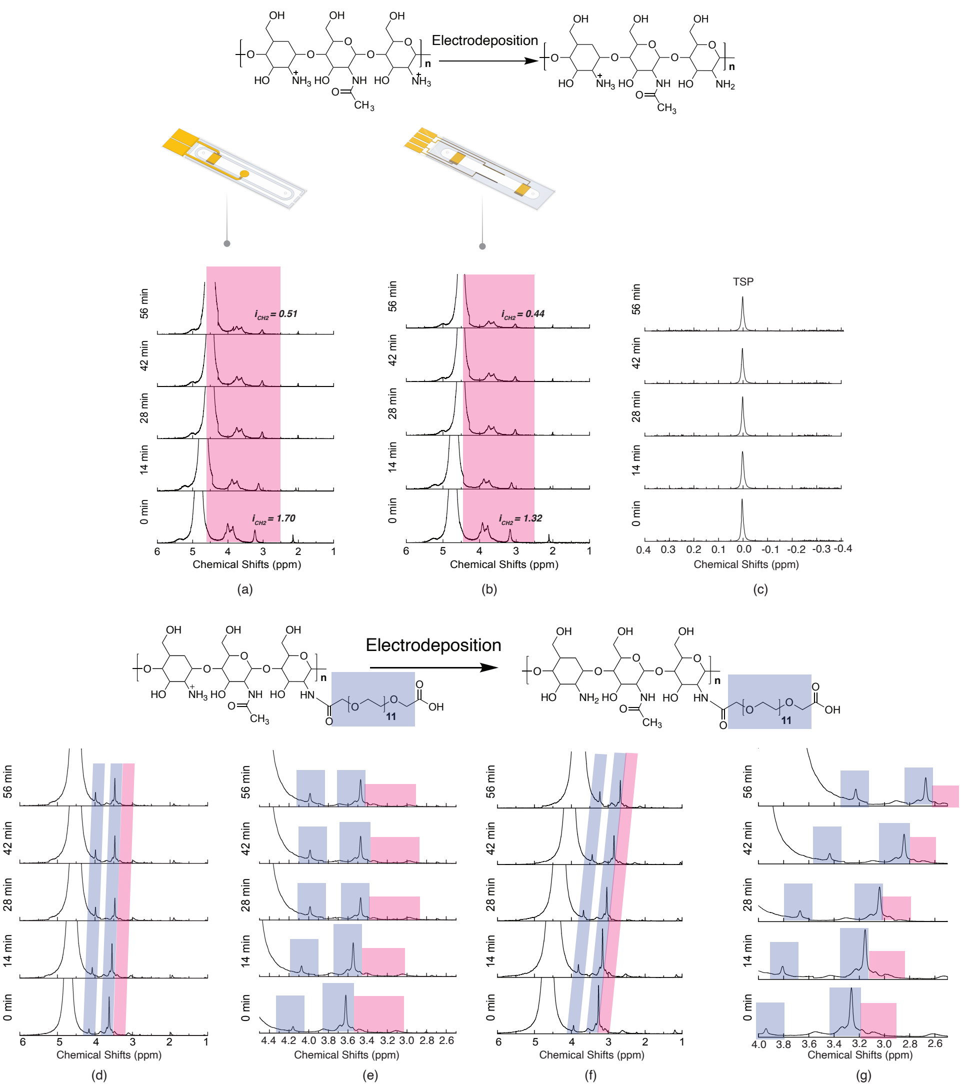

Figure 4.18 – ^{1}H NMR of sequential electrodeposition of (a) CS by using a 3 nm planar electrode and a narrow channel of sidewall electrode (b) and (c) is the TSP reference at 0 ppm; (d) CS-PEG by using 3 nm of planar electrode; (e) magnified spectral region at 2.6-4.4 ppm; (f) CS-PEG by using narrow channel sidewall electrode and zoom-in of the spectrum at 2.6-4.4 ppm (g). Prior to applying a current, a ^{1}H NMR spectrum of the solution was measured and NMR calibrations were performed. After the reference spectrum was measured, a current was applied (3 A/m^2 over a working electrode area) for the entire experiment, and after intervals of 5 minute, a new ^{1}H NMR spectrum was acquired. This cycle was repeated so that a total of 5 spectra were measured.

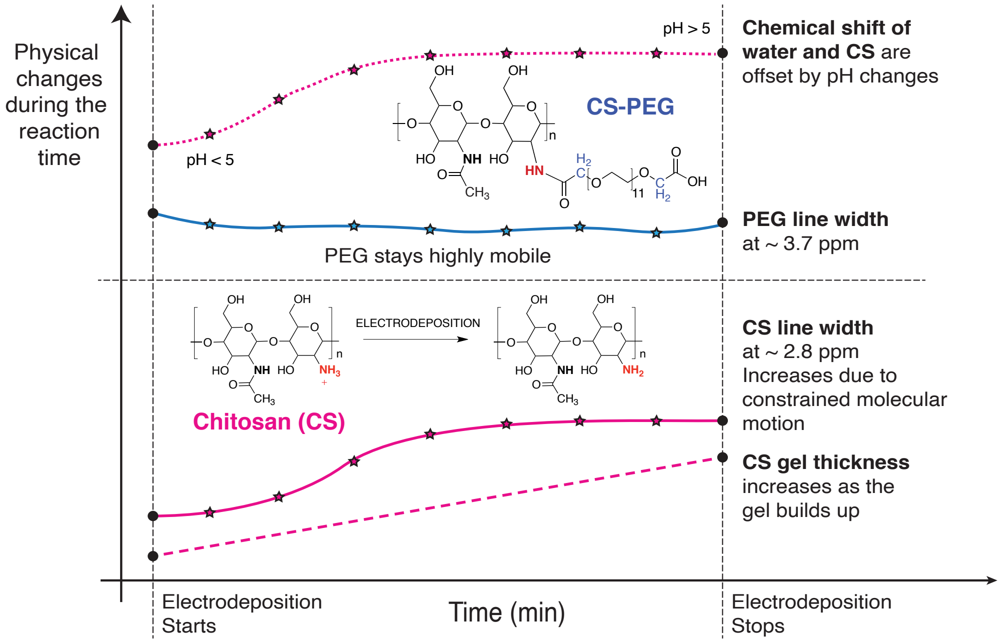
Physical changes during the reaction time
pH > 5
pH < 5
Chemical shift of water and CS are offset by pH changes
CS-PEG
PEG line width at ~ 3.7 ppm
PEG stays highly mobile
ELECTRODEPOSITION
Chitosan (CS)
CS line width at ~ 2.8 ppm Increases due to constrained molecular motion
CS gel thickness increases as the gel builds up
Electrodeposition Starts
Time (min)
Electrodeposition Stops

Figure 4.19 – Information data from the spectra collected for in situ electrodeposition of CSPEG.

By using **planar electrode**: The signal of the PEG shows that the shape of the line is sharper than the spectrum recorded by using the sidewall electrode. This is due to the uniform deposition of hydrogel on the working planar electrode, which covers the entire sample volume under the detector. According to Figure 4.18(d and e), the line width of chitosan at 2.8 ppm increases due to the formation of hydrogel. This shows that the gel builds up. Furthermore, the line width of the PEG signal at 3.7 ppm shows that the PEG molecule stays mobile. The details were illustrated in Figure 4.19.

By using **sidewall electrodes**: The shape of the peaks is wider than the peaks observed with the planar electrode. Nutation spectra shows that the homogeneity of B_1 is higher compared to the planar electrode (Figure 4.13). However, according to Figure 4.18b, the spectra collected before electrodeposition show that the chitosan signal (red region) was observed. In addition, the spectra collected after electrodeposition has similar resolution compared to the platform when using a planar electrode. In a narrow channel of the sidewall electrode platform, the gel was formed on one side of the wall on a working electrode, and another side of the electrode serves as a reference electrode (Figure 4.20). Figure 4.20 shows a representation of the B_0, B_1 and the electric field in

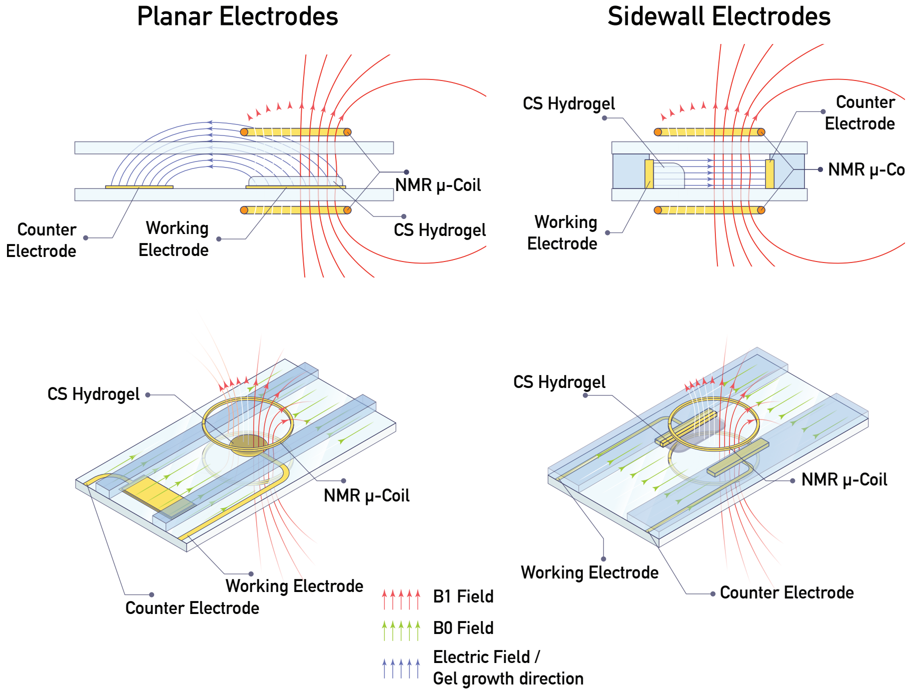
Planar Electrodes
Sidewall Electrodes
NMR µ-Coil
CS Hydrogel
Counter Electrode
Working Electrode
CS Hydrogel
Counter Electrode
NMR µ-Co
Working Electrode
CS Hydrogel
NMR µ-Coil
Working Electrode
Counter Electrode
CS Hydrogel
NMR µ-Coil
Working Electrode
Counter Electrode
B1 Field
B0 Field
Electric Field / Gel growth direction

Figure 4.20 – Illustration of B_1 field, B_0 field and electric field in two different configurations of electrodes during electrodeposition of chitosan.

two different electrode configurations during the electrodeposition of chitosan. The gel deposited on a sidewall electrode is not well distributed in the detector, resulting in a lower homogeneity of both the B_0 and B_1 fields. In addition, the difference in magnetic susceptibility of the materials, i.e. chitosan gel and the solution, also contributes to the signal line broadening (namely; average broadening of the powder: as described in the 2.5.2).

Additional broadening is also attributed to the manufacturing tolerances for the Helmholtz detector, e.g. the Helmholtz coil size, a slight misalignment of the windings, the distance between two windings and the effect of the additional tracks. The narrow sidewalls electrode structure brings the highest B_0 distortions compared to the planar electrode structure, which cannot be fully compensated by shimming. This results in detrimental effects on the signal amplitude.

The SNR was measured for both configurations of electrodes to show the quality of the resolution of the spectra. For the 3 nm planar electrode, the SNR of the water signal before electrodeposition was 4696 and for the narrow channel sidewall electrode 4799. After 15 minutes of plating, the SNR of the water signal for the 3 nm planar electrode was 4080 and for the narrow channel sidewall electrode 4404. This result shows that the electrodeposition of CSPEG has similar impact on the SNR for both electrodes geometries. Furthermore, the integral resulting from the NMR spectra of one of the chitosan signals (at 3.2 ppm) shows that the formation of the hydrogel was $\sim 30\%$.

4.5 Sequential ED of CS-QD for two configurations: Identifying the thickness of the hydrogel

4.5.1 Planar electrodes

The coupling of CS-QD was prepared according to the same protocol as shown in section 4.2.1. This study aims at showing that the multi-layered coupling of CS-QD can be performed using a 3 nm thick planar electrode. Three layers of CS-QD were assembled as shown in Figure 4.21a with a 10-minutes deposition time for each layer at a current density of $3\,\mathrm{A/m^2}$.

The fluorescence intensity from the gel layers was visualised layer by layer using fluorescence microscopy with a band pass filter and the mean intensity was extracted using imageJ. The intensity was then plotted versus time of deposition (Figure 4.21b). To determine the thickness of the individual layers, the upper glass was removed from the platform to measure the thickness of the hydrogel layers using a profilometer. The results of the thickness measurement are shown in Figure 4.21b.

According to Figure 4.21b, for every 20 minutes of deposition, the thickness increases by 20-25 microns, and a proportional increase also results in the mean fluorescence intensity, whereby the average intensity is increased by a factor of 2. On a planar electrode, the gel is stacked vertically layer by layer, therefore we can only visualize a layer if we apply a band pass filter for the emission wavelength of the corresponding quantum dots in the gel.

4.5.2 Sidewall electrodes

By using sidewall electrodes, it is possible to grow hydrogel layers in the direction perpendicular to the channel axis (Figure 4.22a). Therefore, the hydrogel

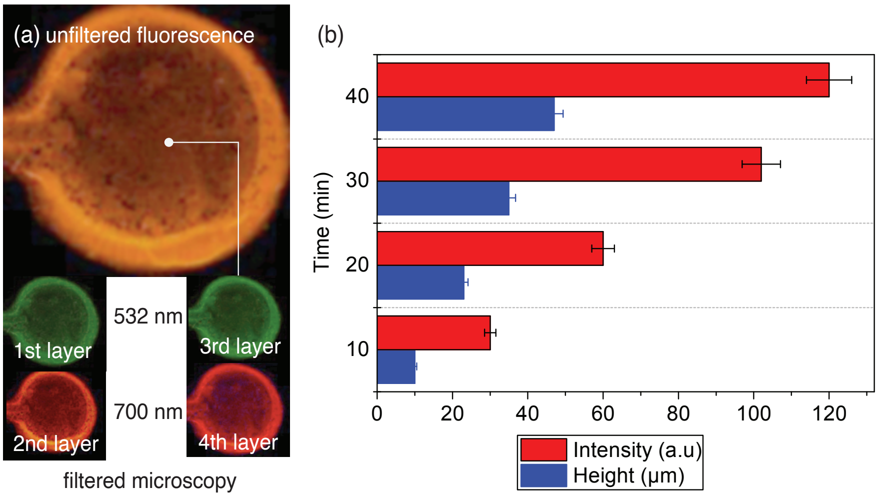

Figure 4.21 – (a) Image of unfiltered (top) and filtered (bottom) from fluorescence microscopy and (b) mean profile height and fluorescence intensity charts versus deposition time, as measured by profilometry and fluorescence microscopy for a three-step sequential electrodeposition of chitosan over 40 minutes total deposition time. A total of four hydrogel layers of QD-labelled chitosan ($\lambda_{\text{emission}} = 532\,\text{nm}$; $560\,\text{nm}$; $700\,\text{nm}$) were assembled.

layer can be visualised like a "layered cake" after coupling to QDs having different emission wavelengths. Figure 4.22b shows a visualization of a total of four hydrogel layers consisting of alternating QD-labelled layers, starting with red QD, followed by green QD and again alternating with red QD and green QD, which were detected by unfiltered fluorescence microscopy. The deposition time for each layer was 10 minutes at the same current density, $3\,\text{A/m}^2$.

The mean fluorescence intensity was extracted using ImageJ. The results in Figure 4.22c show that the mean intensity was in the same range for each 10 minutes deposition. Meanwhile, the measurement of the thickness can be estimated by fluorescent light microscopy because the top glass is firmly bound to the SU-8 layer. To avoid the effect of the sidewall electrodes, the measurement was therefore carried out by standard light microscopy. For each layer, the measurement ruler was placed to estimate the width of the layer. As shown in Figure 4.22c, the width of the first layer is $28 \pm 5\,\mu\text{m}$ after 10 minutes of deposition.

The second layer was $44 \pm 5\,\mu\text{m}$, followed by the third layer $52 \pm 5\,\mu\text{m}$ wide and a fourth layer, $68 \pm 5\,\mu\text{m}$ wide. The measurements were taken after all

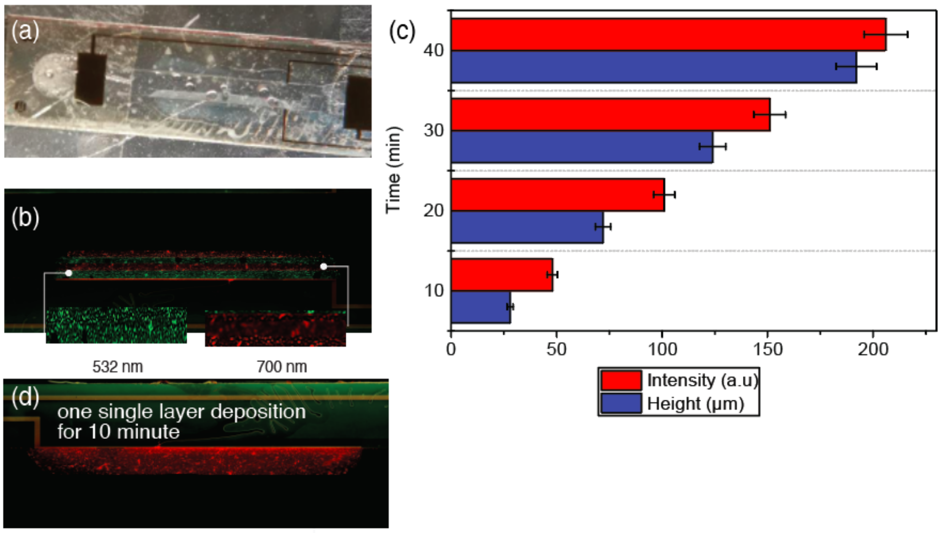

Figure 4.22 – Image from (a) optical microscopy; (b) unfiltered fluorescence microscopy; (c) Mean profile height and fluorescence intensity charts versus time deposition as measured by optical microscopy and fluorescence microscopy for a four-step sequential electrodeposition of chitosan over 40 minutes total deposition time and (d) unfiltered fluorescence microscopy for single layer deposition for 10 minutes. A total of four hydrogel layers of QD-labelled chitosan (($\lambda_{\text{emission}}$ = 532 nm; and 700 nm) were assembled

layers had been deposited. However, the width of single layer deposition for 10 minutes is 65 ± 5 µm(Figure 4.22d). This value is in contrast to the value collected for the first layer after 40 minutes. This result shows that the thickness of the chitosan hydrogel decreases as the next chitosan solution is introduced into the channel, indicating that some of the hydrogel has been re-dissolved.

4.6 Application: Determining the function of enzymes

In this section the results of sequential ED of chitosan within the microfluidic channel, compatible with the NMR microdetector Helmholtz, were used in the application to determine the function of enzymes. In these studies, three different enzymes were monitored, namely urease (Urs), catalase (Cat) and glucose oxidase (GOx). In the first condition of experiment, each enzyme was monitored independently of its own substrates. In the second attempt, the reaction of each enzyme was monitored as co-substrate was added to the reaction. This experiment served to observe the effect of the reaction rate, the active enzyme

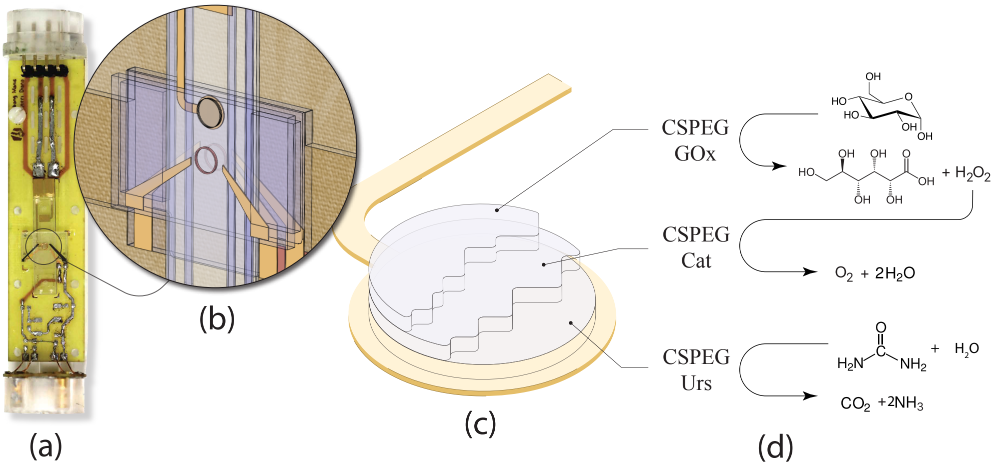

Figure 4.23 – A setup for the multiplex reaction; (a) photo of the platform for the NMR microdetector Helmholtz (b) with the electrochemical cell insert. (c) Illustration of the electrode and stack of gel close to the detector and (d) the chemical reaction relative to each gel layer displayed in (c).

units involved and the kinetic parameters. In the third condition, each enzyme was stacked and the substrates were allowed to carry out their own reaction simultaneously (illustration in Figure 4.23). This study is intended to show that the stack of enzymes can be used as a multiplex biosensor for the own reaction without being dependent on other factors such as co-substrates that are not involved in the reaction process. Note: The reaction was performed with the planar electrode platform. The reason for this is to obtain a large volume of immobilised enzymes on the working electrode and the fabrication process is more robust.

4.6.1 History of urease (Urs) and Glucose Oxidase (GOx)

Background of Urs: Urs is one the most proficient enzymes that catalysed the hydrolysis of urea into ammonia and carbamate (which then decomposes into another ammonia molecule and carbon dioxide)[135]. It has accelerating rate of reaction by a factor of at least 1014 when compared to the urea decomposition by elimination reaction[136–138](Figure 4.24).

At physiological pH, the carbonic acid proton dissociates and the ammonia molecules equilibrate with water to become protonated, resulting in a net increase in pH[136](Figure 4.25).

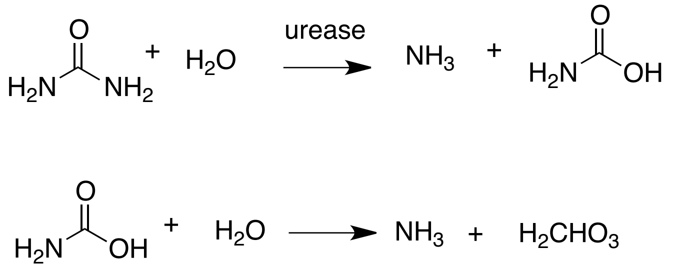

Figure 4.24 – Hydrolysis of urea to yield ammonia and carbonic acid.

$$H_2CO_3 \longrightarrow H^+ + HCO_3^-$$

$$2NH_3 + 2H_2O \longrightarrow 2NH_4^+ + 2OH^-$$

Figure 4.25 – Dissociation of carbonic acid proton and the equilibration of protonated ammonia and water.

Background of GOx: GOx is a flavoprotein that catalyses oxidation of β-D-glucose to D-glucono-δ-Lactone and H_2O_2 with molecular oxygen as an electron acceptor [139, 140]. This reaction can be divided into a reducing and an oxidative step (Figure 4.26). In the reductive half-reaction, GOx catalyzes the oxidation of β-D-glucose to D-glucono-δ-lactone, which is not enzymatically hydrolyzed to gluconic acid. The flavine adeninine nucleotide (FAD) ring is then reduced from GOx to $FADH_2$ [141]. In the oxidative half-reaction, the reduced GOx is re-oxidized by oxygen to obtain H_2O_2. Witteveen *et al.* (1992) [142] found the enzyme melactonase (EC 3.1.1.1.17) in A. niger is responsible for the catalysis of the hydrolysis of glucono-δ-lactone to D-Gluconic acid.

In the solution, the stability of GOx depends on the pH value. It is most stable at about pH 5. Under pH 2 and above pH 8 the catalytic activity is quickly lost [48, 143]. At pH 8.1, for example, only about 10% of the activity is

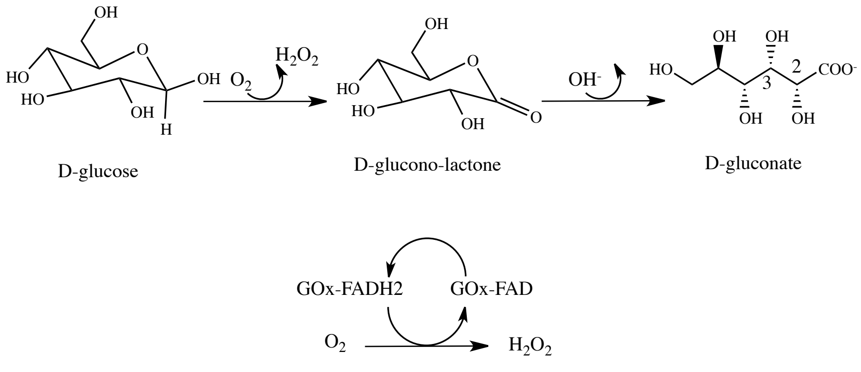

Figure 4.26 – Representation of hydrolysis of urea to yield ammonia and carbonic acid.

retained after 10 minutes; at pH 9.1, inactivation occurs even faster [143]. The inactivation rate at high pH is reduced in the presence of glucose [143, 144]. It is highly resistant to proteolysis and is unaffected by prolonged exposure to trypsin, pepsin and papain [48, 144].

4.6.2 Coupling CSPEG to Urs and GOx

The coupling reaction of CSPEG and the enzymes was performed in a solution using NHS/EDC coupling chemistry. The detailed procedure was discussed in previous section 3.4.1.

To determine the coupling efficiency of enzymes to the PEG linker on the CS chain, we performed UV absorbance measurement on samples containing the modified polymer and the enzyme. First, six different concentrations of free enzymes (Urs and GOx) were measured in three repeated experiments, as shown in to Figure 4.27a and d. Then, solution samples containing only enzymes bound to CSPEG were also measured for UV absorption to estimate the coupling yield. Based on Figure 4.27b and e, the estimate of the initial concentration of 2 mg/mL Urs used to bind to CSPEG and, in a separate sample, 4 mg/mL GOx used to bind to CSPEG was estimated based on the linear adjustment of the free individual enzymes, Urs and GOx. The result revealed the estimated coupling efficiency for enzymes Urs and GOx binding to the polymer show that the coupling efficiency were 41% and 35%, respectively (4.27c and f).

Prior to the electrodeposition of CSPEG enzymes, two different experiments were performed to monitor the function of enzymes with and without polymer in a solution. In the first experiment free enzymes (i.e. without polymer) were allowed to perform the reaction against their own substrates. The reaction was monitored in real-time by collecting ^{1}H NMR spectra every 5-15 minutes (depending on the shimming time). The second experiment, the reaction of the enzymes bound with the polymer, CSPEG, was introduced to the same initial concentration of their own substrates and were monitored in real time. Each ^{1}H NMR spectrum was measured every 5-15 minutes according to the time of the shimming process.

In the next subsection the result of electrodeposition to immobilise enzymes was discussed in detail. The discussion was divided into three parts to explain the function of the individual enzymes, Urs (section 4.6.3), GOx (section 4.6.4) and and multi-layer Urs and GOx enzymes (section 4.6.5).

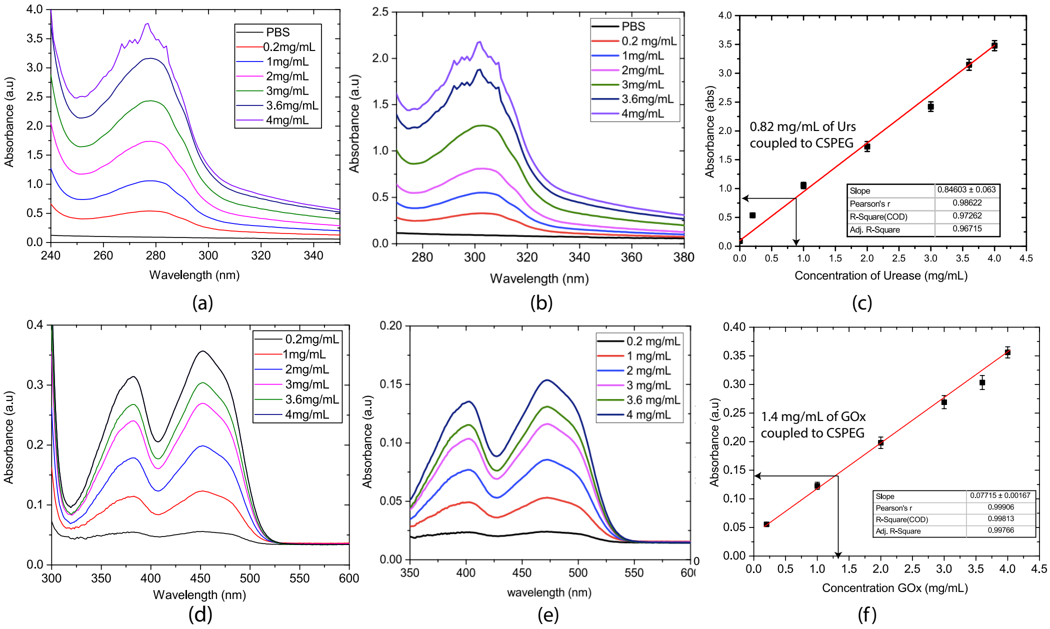

(a) (b) (c)

(d) (e) (f)

Figure 4.27 – UV absorption spectra of (a) Urs, (d) GOx free in solution; (b) CS-Urs, (e) CS-GOx after coupling using the initial enzyme concentrations noted in the legend; (c) Urs and (f) GOx absorbance plots of the six calibration solutions (mean ± standard deviation of three replicates). Arrows indicate the absorbance of the purified CS-enzyme measured at the initial enzyme concentration used throughout this work (2 mg/mL Urs, 4 mg/mL GOx). Absorbance was measured at 280 nm (Urs, solution), 380 nm (GOx, solution), 300 nm (CS-Urs), and 400 nm (CS-GOx).

4.6.3 Monitoring activity in situ first layer of CSPEG-Urs

Enzymatic activity experiments were performed under two different conditions: a) using enzymes with and without CSPEG polymer in solution and b) using immobilised enzymes after the electrodeposition process. For condition (a), the experiments were performed in a solution phase, whereas for condition (b), the activity of the enzyme was monitored in a gel phase. For condition (a), 2 mg/mL Urs was reacted with 1000 mM urea and a timer was started to take note of the time period t_0 occurring between the beginning of the reaction and the start of the sequential NMR acquisitions. Then the solution was transferred to the microfluidic channel mounted on the probe in such a fashion that the NMR detection volume would be placed upstream of the working electrode for electrodeposition, for consistency with the procedure for condition (b). The time required to collect the measurement (including the shimming process) was added to t_0. The reaction was then monitored every 20 minutes, i.e. the ^{1}H NMR spectrum of the on-going reacting sample was regularly recorded every 20 minutes time interval. The procedure was repeated using CSPEG-Urs in 1000 mM urea solution. The results are presented in Figure 4.28b (top), where filled symbols indicate Urs without CSPEG polymer and hollow symbols indicate Urs with CSPEG polymer. This result showed that Urs is active in a solution either containing the polymer or polymer-free and it consumes the urea substrate until the end. The reaction seems to have a faster onset when the enzyme is bound to the CSPEG polymer, as indicated by the initial slope of the reaction, being steeper for CSPEG-bound Urs.

For condition (b), we monitored the function of the immobilised Urs after performing the electrodeposition of modified CSPEG-Urs polymer, where the electrodeposition step was performed for 15 minutes at a stable current density of 3 A/m^2. The microfluidic channel was then gently rinsed with 200 mM NaAc at pH 7 and D_2O to stabilize the gel. Then 1000 mM urea (including 50 mM of TSP as NMR reference) in 200 mM NaAc solution at pH 7 was injected into the channel. The time at which the substrates reached the gel position in the channel was recorded as t_0. The microfluidic channel was then mounted on the probe so that the detection area was placed upstream with respect to the gel. Then the sequential NMR was collected for every 15 minutes + 9 minutes of acquisition time. The resulting NMR spectrum is presented in Figure 4.28a, as

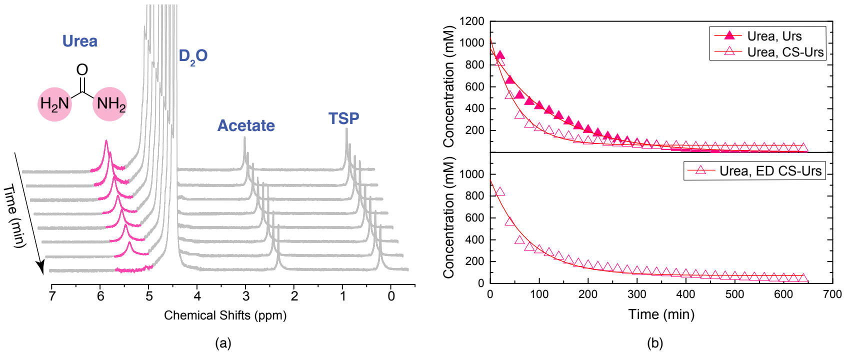

Figure 4.28 – (a) ^{1}H NMR spectra obtained for the electrodeposited CSPEG-Urs hydrogel case. The hydrolysis of urea (highlighted in pink, 5.8 ppm) is shown as a function of time, and (b) extracted urea concentration in the presence of; top: Urs (hollow symbols) and CSPEG-Urs (filled symbols) in solution, and bottom: immobilised CSPEG-Urs. The urea concentration was calculated using the internal standard (TSP, 50 mM). The fits to the data were obtained using the Michaelis-Menten kinetic model (see Eq. 4.6 and 4.7). Kinetic parameters summarized in Table 4.3.

well as the extracted value of the concentration of urea as a function of time (Figure 4.28b(bottom)).

Based on Figure 4.28b, the signal of urea at 5.8 ppm decreases due to hydrolysis of urea into NH_4^+ ion. Furthermore, the constant signal of the methylene group of acetate at 1.8 ppm indicates that the acetate buffer does not interrupt the activity of the enzyme. Furthermore, the water signal shows no changes in the chemical shifts caused by the reaction, since we know that the pH environment for the individual Urs reaction (Appendix D.10) changes due to the formation of NH_4^+ ions that cause the alkaline environment. This counter intuitive finding may be the result of the increased buffering effect of the CS polymer, maintaining better control of pH during the reaction as compared to the case of Urs in solution. Figure 4.29a shows the increase in pH for the activity of Urs, while the pH for CS-Urs had a range in the optimal pH 5.5 –6.5 where the pKa of CS is 6.5. This result confirmed that the CS polymer act as a buffer during the reaction.

4.6.4 Monitoring activity of in situ of CSPEG-GOx

Reaction-monitoring experiments with GOx were set up analogously to what was done with Urs, that is under condition (a) solutions of both free GOx and CSPEG-bound GOx were prepared, and under condition (b) the reactions were

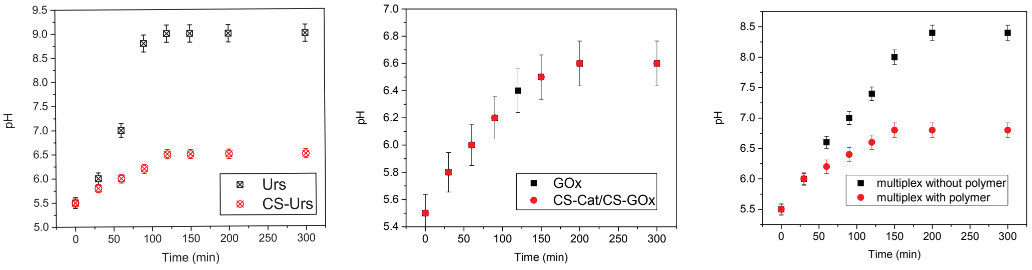

(a) (b) (c)

Figure 4.29 – pH calibration for the enzymes (a)Urs; (b) GOx and (c) multiplex enzymes with and without polymer.

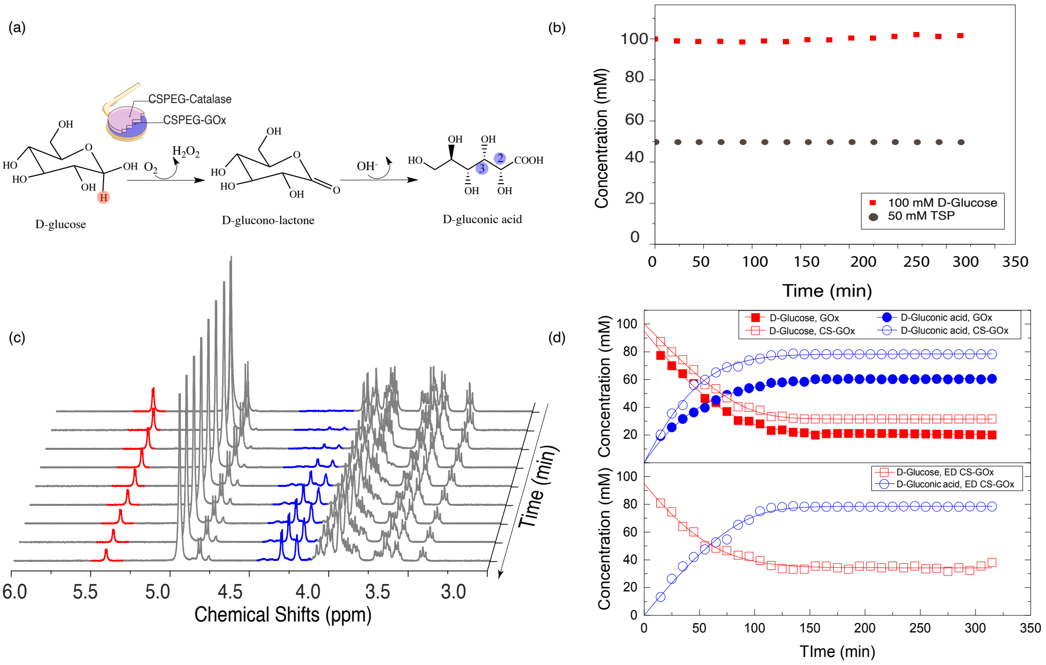

Figure 4.30 – (a) Scheme of oxidation of D-glucose in the presence of immobilised GOx (1st layer) via immobilised catalase (2nd layer) as co-enzyme; (b) the concentration of D-Glucose at 5.3 ppm and TSP (at 0 ppm) as a function of time without GOx. (c) ^{1}H NMR spectra of the electrodeposition of CSPEG-GOx enzyme kinetics at 500 MHz and (d) Top: ^{1}H NMR results of D-glucose depletion of GOx without polymer (filled symbols) and GOx with polymer (hollow symbols) obtained using independent traces; Bottom:NMR results of D-glucose depletion and formation of D-gluconic by immobilised CSPEG-GOx as an independent layer of hydrogel. The D-Glucose concentration is shown as a function of time due to the oxidation process of the enzyme GOx. The fits to the data were obtained using the Michaelis-Menten model, with the kinetic parameters summarized in Table 4.4. Solid lines report Best-fit curves (see Eq. 4.6 and 4.7).

set up in gel. For condition (a), 4 mg/mL GOx and 1 mg/mL catalase co-enzyme was reacted with 100 mM D-glucose. Figure 4.30a shows the schematic reaction of D-glucose in the presence of GOx and catalase to form the intermediate product D-glucono-lactone and the final product D-gluconic acid, and Figure 4.30b shows the extracted data for a control experiment, 100 mM D-glucose solution (at 5.2 ppm) with an internal NMR reference, 50 mM TSP without enzyme. Two separate polymer solutions were prepared, namely CSPEG coupled to GOx and CSPEG coupled to catalase. Then the two solutions were mixed and 100 mM D-glucose was added to the mixture. NMR spectra were collected as a function of time, following the same procedure as for Urs. Sequential NMR measurement with accompanying calculated concentration profiles for the reaction are presented in Figure 4.30d(top). Filled red marks indicate a reaction of D-Glucose with GOx in absence of CSPEG polymer and hollow mark is for the same reaction in the presence of CSPEG polymer. For GOx's reaction, we can simultaneously monitor the decrease of D-glucose and the formation of the product D-gluconic acid (blue marks) with the aid of the co-enzyme catalase. Catalase was introduced to consume hydrogen peroxide from the reaction of GOx and to convert it back into oxygen gas. The full oxidation reaction of D-Glucose and its conversion into the product D-gluconic acid is shown in Figure 4.30b. The result showed that the GOx enzyme in a solution, whether bound to the polymer or not, was observed to be significantly less as compared to Urs, and only up to approximately 70-80 % of the initial D-glucose was consumed.

For condition (b), i.e. a reaction carried out in gel phase, two layers of gel containing GOx and cat were deposited on the working electrodes under constant current density for 15 minutes. CSPEG-GOx was deposited first. Then, after the first layer had stabilized, CSPEG-catalase was deposited on top of it. Both layers were stabilized with 200 mM of NaAc in D_2O. Then 100 mM D-Glucose was introduced to the gels, as well as including 50 mM TSP in a 200 mM NaAc solution at pH 7. Figure 4.30c reports the sequentially acquired NMR spectra for the reaction. Glucose-related peaks occur between 4.0 ppm and 3.2 ppm and also at 5.3 ppm (highlighted in red) in the ^{1}H-NMR spectrum. The concentration of D-gluconic can be easily determined from the two peaks at 4-4.2 ppm, which are due to the protons at positions 2 and 3 in the D-gluconic acid molecule (highlighted in blue). As expected, the D-Gluconic acid concentration increases monotonically with increasing reaction time (Figure 4.30d). The GOx catalyses the reaction using half of an oxygen molecule to produce a D-Gluconic acid molecule. The hydrogen peroxide that is also produced is converted back into molecular oxygen by per-oxidase via the catalase enzyme. Therefore, the final amount of D-Gluconic acid is twice the amount of molecular oxygen absorbed by the solution.

4.6.5 Monitoring activities in situ multi-layers of CSPEG-Urs, CSPEG-cat and CSPEG-GOx

Next, the possible application of the platform system for multiplex screening with a sequential multi-layered hydrogel containing enzymes was evaluated. We assigned three different enzymes on a stack of three hydrogel layers (Figure 4.31a). The three layers (1st layer: CSPEG-Urs; 2nd layer: CSPEG-cat and 3rd layer: CSPEG-GOx) were deposited using the same current density for 15 minutes each (the image of the stacked enzymes is shown in Figure 4.31b). After deposition of each layer, 200 mM NaAc solution was injected, followed by D_2O to rinse and stabilize the gels. The substrates, 1000 mM urea and 100 mM D-glucose in a 200 mM NaAc, 50 mM TSP solution at pH 7 were then introduced to allow the reaction to proceed. The ^{1}H-NMR spectrum was recorded every 15-20 minutes (depending on shimming conditions). The results are presented in Figure 4.31c.

According to Figure 4.31c, the depletion of urea signal (highlighted with pink colour, at 5.8 ppm) during the hydrolysis process and simultaneously the formation of the oxidation product of D-glucose, D-gluconic acid (highlighted with blue colour, at 4-4.2 ppm) as a function of increasing time was observed.

Based on this result, the hydrolysis of urea is not interrupted by the oxidation of the D-glucose. Both reactions are well suited to perform their own process. Furthermore, there are no changes in the chemical shifts of the water signal, which indicates that the pH environment of the reaction does not change. This result is confirmed by monitoring the pH of the activity of the multiplexed enzyme in a solution in which the activity of the enzyme shows the pH range 5.5 –6.6 (Figure 4.29c). The immobilisation of Urs and GOx shows that the reactions run independently of each other. For the immobilisation of the co-enzyme catalase, the reaction for the production of oxygen was dependent on the release of the amount of hydrogen peroxide from the oxidation of the D-glucose, which is carried out in the third layer. In this case, the second layer and the third layer of the stack were categorized as reaction-dependent.

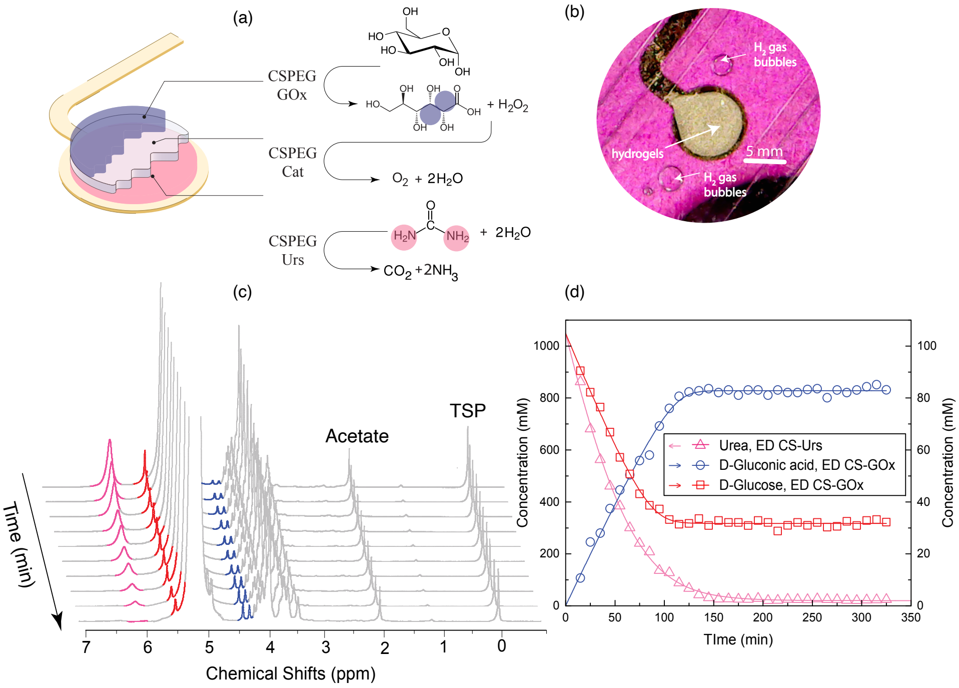

Figure 4.31 – (a) Illustration of the stack of immobilised enzymes with three different layers and the chemical reaction in each substrate; (b) Multi-layer hydrogel on top of each other (3 layers beginning with CSPEG-Urs, CSPEG-cat and CSPEG-GOx); (c) real-time ^{1}H NMR spectra of the Urs and GOx enzymes kinetic at 500 MHz. Hydrolysis of urea (highlighted with pink, 5.8 ppm) as it is converted to NH_4^+ is shown as a function of increasing time, whereas the signal highlighted in blue at 4.2 ppm appear to be D-Gluconic and (d) extracted urea, D-Glucose and D-Gluconic concentrations from the NMR results in (c).*GOx experiments were always performed using GOx:Catalase in a 4:1 ratio.

The kinetic activity is explained in the next subsection.

4.6.6 Extraction of enzymes activity by using Michaelis-Menten equation

The quality and reproducibility of the NMR-based approach to reaction kinetics monitoring depends largely on how reliably the NMR peak area integrals can be converted to concentrations. In this thesis the peak area integrals from recorded ^{1}H-NMR spectra were converted into concentration values using the known concentration of TSP added to the sample (50 mM of initial TSP concentration). Determining the molecular concentration using this approach reduces the uncertainties in the quantification of peak areas, since each sample has its own internal reference (known concentration of TSP spiked into the solvent

D_2O). This approach also allows a comparison of data collected from different experiments.

The initial slope of the concentration profile $S(t)$, i.e. the reaction velocity at the very beginning of the reaction, was estimated by calculating the numerical derivative of the best fit curve to the Michaelis-Menten model at $S(t) = 5\text{min}$. The initial concentration parameter S_0 has been set within a ±5% uncertainty over the nominal initial concentration because there are not enough data points near $S(t)= 0$ to allow accurate extrapolation of the intercept when this parameter is allowed to run freely. The reaction velocity extracted from reagent concentration curves and expressed in mM/min was converted to μmole/min using the known volume of either solution or gel containing the enzyme. This operation allows to estimate the absolute amount of product produced per minute, and therefore estimate the units of active enzymes. By definition, a *unit* (U) of enzyme is the amount required to produce 1 µmol of product per minute, under optimal reaction conditions.

Additional reaction kinetics parameters can by extracted from the time-dependent concentration curve $S(t)$ by using the well established Michaelis-Menten enzyme kinetics model.

For a reagent time series the following equation holds for the time evolution of the concentration $S_r(t)$ of a reactant[145]:

$$S_r(t) = S_\infty + K_m W \left[\frac{S_\infty - S_0}{K_m} e^{\frac{(S_\infty - S_0) - V_{\max}(t-t_0)}{K_m}} \right] \tag{4.6}$$

And for product concentration $S_p(t)$:

$$S_p(t) = S_\infty - K_m W \left[\frac{S_\infty - S_0}{K_m} e^{\frac{(S_\infty - S_0) - V_{\max}(t-t_0)}{K_m}} \right] \tag{4.7}$$

where S_0 is the concentration of reagent at time t_0, S_∞ is the concentration at the conclusion of the reaction, K_m (Michaelis constant) corresponds to the reagent concentration at which half of the enzyme's active sites are occupied, $V_{\max}$ is the maximum possible reaction rate . W is the Lambert W-function, the inverse function of $f(W) = W \exp W$. Details about the derivation of equations 4.6 and 4.7 can be found in [146].

It should be noted that the kinetic parameter $V_{\max}$ is defined as maximum rate of the reaction when *all active sites* are populated by the substrate. The initial reaction rates from the experiments may in principle differ from $V_{\max}$

since the initial reaction rate depends on S_0, i.e. on the initial substrate concentration. Nevertheless, in the presented work, we took care of oversaturating the active sites with substrates in all experimental setups. Therefore the initial reaction rate has been nominally considered equal to the maximum reaction rate V_{max}.

The number of active enzyme units calculated from the initial reaction rates extracted from the kinetic data was used to determine the catalytic performance under various conditions. These conditions included enzymes in solution, polymer-coupled enzymes in solution, and polymer-coupled enzymes in the hydrogel state.

Urs activity

(a) Reaction in solution

1) Urs with and without polymer in a solution: The number of active units was used as a metric to investigate the influence of the coupling chemistry and hydrogel immobilisation on enzyme performance. Urs was tested by transferring a solution containing 2 mg/mL Urs + 1000 mM urea to the microfluidic channel (3.2 µL) for NMR measurement (pH 5.5, NaAc). The resulting NMR data are plotted in Figure 4.28b (top:filled symbols). As per the manufacturer data sheet, 0.633 ± 0.006 U of Urs were expected using 2 mg/mL Urs, while the measurement revealed 0.057 ± 0.013 U of Urs, i.e. the active fraction was 9 ± 2 %.

The procedure was repeated using CSPEG-Urs in 1000 mM urea solution (pH 5.5, NaAc). The results are presented in Figure 4.28b (top:hollow symbols). The CSPEG-Urs solution was prepared so that the concentration of Urs was 2 mg/mL and, accounting for the coupling yield, 0.259 ± 0.007 U of Urs was expected. The measurement revealed 0.076 ± 0.025 U of Urs were present, i.e. 29.3 ± 9.8 % (data summarized in Table 4.3).

The fraction of active Urs units was observed to be higher for CSPEG-Urs in solution compared to free Urs in solution (29.3 ± 9.8 % vs. 9 ± 2 %). One would expect that the restricted diffusion together with deactivation of a fraction of the enzymes due to the coupling chemistry would decrease the efficiency[147]. This counter intuitive result may be the result of the increased buffering effect of the CS polymer, maintaining better control of pH during the reaction as compared to the case of Urs in solution. In the absence of CS, the pH was observed to increase from 5.5 to 9 at the end of the reaction, while the presence of CS controlled the pH such that it increased from 5.5 to 6.5 (Figure 4.29a). At elevated pH, Urs activity is expected to be limited as it has been reported that Urs maintains activity from below pH 3 to 7.5[148].

Experiment	Initial Slope mM/ min	$V_{\max}$ mM/ min	K_m mM	Container Volume nl	Coupling Efficiency -	Theoretical Units mU	Active Units mU	Active Fraction %
Solution								
Urs + Urea	9 ± 2	11 ± 3	996 ± 228	3163 ± 32	-	633 ± 6	57 ± 13	9.0 ± 2.0
CSPEG-Urs + Urea	12 ± 4	14 ± 4	801 ± 133	3163 ± 32	0.41 ± 0.01	259 ± 7	76 ± 25	29.3 ± 9.8
Urs / GOx* + Urea, D-Glucose	14 ± 2	14 ± 3	504 ± 161	3163 ± 32	-	633 ± 6	89 ± 13	14.0 ± 2.0
CSPEG-Urs / CSPEG-GOx* + Urea, D-Glucose	14 ± 3	15 ± 7	355 ± 101	3163 ± 32	0.41 ± 0.01	259 ± 7	89 ± 19	34.2 ± 7.4
Hydrogel								
CSPEG-Urs + Urea	10.3 ± 3	13 ± 3	540 ± 118	26.5 ± 0.3	0.41 ± 0.01	2.17 ± 0.06	0.53 ± 0.16	24.4 ± 7.4
CSPEG-Urs / CSPEG-GOx* + Urea, D-Glucose	14 ± 2	15 ± 3	540 ± 118	22.6 ± 0.2	0.41 ± 0.01	1.85 ± 0.05	0.63 ± 0.09	34.2 ± 5.0

Table 4.3 – Summary of the kinetic activity of **Urease** using the micro-detector Helmholtz coil. *Note: The reaction of the GOx enzyme is always linked to its co-enzyme, catalase, in a 4:1 ratio.

(b) Reaction in hydrogel

2) Electrodeposition of CSPEG-Urs: To verify that the enzymes retained their activity post-electrodepostion, hydrogels were generated using the same CS-enzyme solutions as were functionally verified in solution. For CSPEG-Urs, the microfluidic device was filled with a 1 % w/v solution and 3 A/m^2 of current was applied for 15 min to the electrodes within the channel. Once electrodeposition was complete, the fluidic channel was gently flushed with 200 mM NaAc and D_2O to stabilize the hydrogel before introducing a 1000 mM urea solution (in 200 mM NaAc, pH 7) to initiate the reaction. For NMR measurements, the sample insert was placed so that the planar electrode did not enter the NMR detection volume. The resulting NMR spectra (one time point every 24 min) and extracted concentrations are plotted in 4.28b (bottom).

The NMR measurement revealed 0.53 ± 0.16 μU of Urs were present in the system. To estimate the fraction of Urs that was active, it was first necessary to estimate the volume of the hydrogel (details in Appendix E.1). Given the dimensions of the planar electrode (circle with radius 0.6 mm) and a deposition time of 15 min yielding a thickness of $\sim$ 15 µm,[107] a volume of 26.5 ± 0.3 nL could be estimated. Given that the coupling yield was 41 %, the fraction of Urs that was active was then 24.4 ± 7.4 % (summarized in Table 4.3).

Several important parameters can be extracted from NMR data by nonlinear fitting to the Michaelis-Menten model (equations 4.6 and 4.7), such as $V_{\max}$ and the K_M values that identify the reaction rate and the affinity that binds the substrate and the active site of its own enzymes, respectively. The initial slope, $V_{\max}$ for the single gel layer and for the multi-layered gel stack have overall similar values as those found in a solution, that is 13 ± 3 mM/min for the single layer of CSPEG-Urs layer versus 14.0 ± 4 mM/min for CSPEG-Urs in a solution, and 15.0 ± 3 mM/min for multi-layer CSPEG-Urs vs. 15.0 ± 7 mM/min for multiplex enzymes in a solution.

The K_M value for individual layers of CSPEG-Urs is 540 ± 118 mM, but in a solution of Urs bound to CSPEG, the K_M value is higher, i.e. 801 ± 133 mM. However, in a multiplex system, the K_M value for the dual hydrogel layer of CSPEG-Urs is higher than in a multiplex system in a solution, that is 540 ± 118 mM versus 355 ± 101 mM. These results show that the binding affinity of substrates with the active site of Urs is weaker in a multiplex system in hydrogel with respect to within a solution, but for individual layers the affinity is stronger than in a solution[138]. For single layer systems, there is no competition from other substrates (e.g. D-glucose), therefore a relatively low concentration of urea is needed to occupy the binding site. On the other hand, in a multiplex system, binding with low affinity (high K_M value), a much higher concentration of a urea is required before the binding site is maximally occupied and the maximum physiological response to urea is achieved. This increase in K_M values from the solution phase to the hydrogel phase can either be a consequence of structural changes in the enzyme introduced by the multi-layer immobilisation process, or reduced accessibility of the substrate to the active site of the immobilized enzyme, as reported [149, 150].

GOx activity

(a) Reaction in solution

1) Catalase + GOx with and without polymer in a solution: The GOx / Catalase system was similarly evaluated in the microfluidic system, starting with a solution containing 4 mg/mL GOx and 1 mg/mL Catalase + 100 mM D-glucose (pH 5.5, NaAc). Figure 4.30d (top) reports the NMR data, in this case both reactant consumption (D-glucose) and product formation (D-gluconic acid) could be followed. From the data sheet, 1.265 ± 0.013 U GOx were expected, and from the NMR data 2.9 ± 0.1 mU were observed (0.23 ± 0.01 % active fraction).

To perform the CS-coupled experiments, two polymer solutions were prepared: CSPEG-GOx and CS-Catalase. The two polymer solutions were mixed to maintain the 4:1 ratio of GOx:Catalase, and to maintain the expected concentration of GOx at 4 mg/mL. Finally, the polymer solution was added to a D-glucose solution (100 mM) before transfer to the microfluidic system and the start of the NMR measurement (results in Figure 4.30d (top: hollow symbols), spectra in Appendix D.12b). The active units were determined to be 2.5 ± 0.6 mU, which was 0.57 ± 0.14 % of the added 443 ± 13 mU (after accounting for coupling yield) (data summarized in Table 4.4).

The fraction of active GOx enzyme was observed to be significantly lower compared to Urs, and only up to approximately 70-80 % of the initial D-glucose was consumed. The solution pH cannot explain this observation: the optimal pH for GOx activity is in the range 6.5-7.5[151] which was maintained in our system (Figure 4.29b). A possible explanation for the incomplete substrate conversion is an oxygen deficiency. In the presence of catalase, 0.5 mol of oxygen is consumed for every mol of D-glucose. Since the reaction volume was only 3.2 µL and the materials used to fabricate the device restrict oxygen diffusion into the solution, oxygen could have become the limiting reagent as the reaction progressed. This is supported by control experiments performed in standard 5 mm NMR tubes, where the sample volume is 500 µL and a large gas headspace is available in the NMR tube. Every other parameter held constant, a factor of 2-4 improvement in the fraction of active units was observed (Table 4.6). This highlights the importance of considering oxygen perfusion in microfluidic devices in cases where it participates in the process[152].

(b) Reaction in hydrogel

2) Electrodeposition of CSPEG-GOx (1st layer) and CSPEG-catalase (2nd layer): In the case of the GOx and Cat, a two layer hydrogel was generated (multi-layered hydrogels will be denoted as layer-1 / layer-2 / layer-n). Using the same polymer concentration and electrodeposition parameters as for CSPEG-Urs, the two layer hydrogel was built by depositing CSPEG-GOx, rinsing and stabilization with 200 mM NaAc buffer in D_2O, then deposition of CSPEG-Catalase, followed by rinsing and stabilization so that a CSPEG-GOx / CSPEG-Cat hydrogel was created. To initiate the reaction, 200 mM D-Glucose was flushed into the microfluidic channel (in 200 mM NaAc, pH 7) and NMR measurements were started. The NMR spectra and extracted concentrations (glucose at 5.2 ppm, D-Gluconic acid at 4.0, 4.2 ppm) are plotted in Figure 4.30c,d (bottom).

As in the case of the Urs hydrogel, GOx was observed to retain its activity when coupled to chitosan and electrodeposited as a hydrogel. The number of active units were determined to be 23 ± 3 nU, with a fractional activity of 0.60 ± 0.07 % (summarized in Table 4.4).

Comparison between the chitosan-coupled cases reveals that the activity of both Urs and GOx is not influenced after deposition as a hydrogel. This result is not completely surprising since by definition the hydrogel is highly hydrated, and thus diffusion of the substrate through the polymer network should be minimally restricted.

Experiment	Initial Slope mM/ min	$V_{\max}$ mM/ min	K_m mM	Container Volume nl	Coupling Efficiency -	Theoretical Units mU	Active Units mU	Active Fraction %
Solution								
GOx + D-Glucose	0.93 ± 0.02	0.98 ± 0.04	282 ± 67	3163 ± 32	-	1265 ± 13	2.9 ± 0.1	0.23 ± 0.01
CSPEG-GOx + D-Glucose	0.80 ± 0.20	0.87 ± 0.04	77 ± 16	3163 ± 32	0.35 ± 0.01	443 ± 13	2.5 ± 0.6	0.57 ± 0.14
Urs / GOx* + D-Glucose, Urea	1.60 ± 0.80	1.50 ± 0.50	38 ± 6	3163 ± 32	-	1265 ± 13	5.1 ± 2.5	0.40 ± 0.20
CSPEG-Urs / CSPEG-GOx* + D-Glucose, Urea	0.84 ± 0.05	0.90 ± 0.30	25 ± 5	3163 ± 32	0.35 ± 0.01	443 ± 13	2.7 ± 0.2	0.60 ± 0.04
Hydrogel								
CSPEG-GOx* + D-Glucose	0.84 ± 0.10	0.85 ± 0.08	57 ± 13	26.5 ± 0.3	0.35 ± 0.01	3.7 ± 0.1	0.023 ± 0.003	0.60 ± 0.07
CSPEG-Urs / CSPEG-GOx* + D-Glucose, Urea	0.90 ± 0.20	0.90 ± 0.10	22 ± 4	26.5 ± 0.3	0.35 ± 0.01	3.7 ± 0.1	0.024 ± 0.005	0.64 ± 0.14

Table 4.4 – Summary of the kinetic activity of **Glucose Oxidase** using the micro-detector Helmholtz coil.*Note: The reaction of the GOx enzyme is always linked to its co-enzyme, catalase, in a 4:1 ratio.

As in the case of the Urs hydrogel, GOx was observed to have an initial rate of reaction, $V_{\max}$ of D-gluconic acid similar to the one extracted from the initial slope. The results are shown in table 4.4. Analogously to what was observed with Urs, the initial slope and $V_{\max}$ for the single gel layer and the gel multi-layer have the comparable value with respect to experiments carried out in solution, i.e. $0.84 \pm 0.10\,\mathrm{mM/min}$ for the single layer CSPEG-Urs versus $0.80 \pm 0.20\,\mathrm{mM/min}$ for CSPEG-Urs in a solution, and $0.90 \pm 0.20\,\mathrm{mM/min}$ for a multi-layer of CSPEG-Urs versus $0.84 \pm 0.05\,\mathrm{mM/min}$ for multiplex enzymes in a solution.

These values of $V_{\max}$ show that the initial reaction rate for the GOx enzyme is similar in all cases. This is due to the fact that the S_0 of the substrates have been set to the same concentration, by taking into account a relative uncertainty of ±5%, that is for Urs: 950 mM - 1050 mM urea, and for GOx: 95 mM - 105 mM D-glucose.

In the case of the binding affinity of GOx activity, it was observed that the K_M value for free GOx is higher, $282 \pm 67\,\mathrm{mM}$, compared to GOx bound to CSPEG, $K_M = 77 \pm 16\,\mathrm{mM}$. This result showed that the binding of D-glucose to the active site of GOx is weaker in the first case, and this is confirmed by the lower percentage of active fraction estimated by the NMR result (0.23 ± 0.01 %). In the case of a bilayer CSPEG-GOx/CSPEG-catalase hydrogel, the value of $K_M = 57 \pm 13\,\mathrm{mM}$ is higher than in the solution phase, i.e. $38 \pm 16\,\mathrm{mM}$. This shows that the binding of D-glucose to the active site of GOx is stronger in solution than in hydrogel. In contrast, the multiplex system in the hydrogel has a similar value of K_M with a multiplex solution, that is $22 \pm 4\,\mathrm{mM}$ versus $25 \pm 5\,\mathrm{mM}$, respectively. This result shows that the D-glucose in a multiplex system has a stable binding affinity with the active site of GOx bound to CSPEG. The active fraction for the CSPEG-bound GOx cases confirms the stability of the substrate D-glucose when binding to the active site of GOx (Table 4.4).

Multiplex enzymatic activity

Enzyme functionality is maintained after coupling and deposition as a hydrogel. Catalytic cascades also remain active, even when catalytic steps are spatially separated, as in the the dual-layer CSPEG-GOx / CSPEG-Catalase example. The multi-layer hydrogel assembly process was further extended to include multiple, independent catalytic reactions. A three layer hydrogel was deposited with the composition CSPEG-Urs / CSPEG-Cat / CSPEG-GOx (schematic in Figure 4.31a). This multiplexed system was prepared using two different electrode geometries, taking advantage of the investigation into optimizing electrode placement with respect to the NMR detection volume (see Section 4.3)[153]. The planar geometry, as in the CSPEG-Urs and CSPEG-GOx / CSPEG-catalase examples, was used to place the catalytic hydrogel assembly slightly upstream (i.e. outside) of the NMR detector. The side-wall electrode geometry, with better NMR performance, was used to place the hydrogel within the NMR detector.

The hydrogel was assembled using the same protocol as described in Section 4.6.5: for each layer, CS-modified polymer solution was injected into the microfluidic device, then electrodeposition was carried out for 15 min, then rinsing (using 200 mM NaAc, pH 7). The final assembly was then exposed to a solution containing substrates for both GOx and Urs: 1000 mM urea and 100 mM D-glucose (200 mM NaAc, pH 7). The ^{1}H NMR spectra and extracted concentration profiles versus time are presented in Figure 4.31 c,d and Figure 4.32c,d for both electrode geometries.

The NMR data clearly shows the ability to monitor both reactions (urea hydrolysis, glucose oxidation) simultaneously. The substrates (urea, glucose) and product (D-Gluconic acid) all have unique signals that can be used for quantitative determination of the catalytic processes. The extracted kinetic data is summarized in Table 4.5. Accounting for the expected number of active units within the respective hydrogel layers, the fraction of active enzymes were determined to be essentially independent of hydrogel assembly (compare Tables 4.3 and 4.4) and electrode geometry (Table 4.5).

Multiplex enzymatic activity using sidewalls electrode

By using electrodes fabricated on the sidewalls of the fluidic channel, it is possible to grow a chitosan gel in the direction perpendicular both to the channel axis and to the gel growth direction on a planar electrode. Due to a limit on the achievable NMR spectrum resolution, sidewall electrodes in a narrow fluidic channel was the selected geometry. Unlike the planar electrodes case, the immobilised enzymes were placed directly within the NMR detector to monitor the enzymes activity. The results are presented in Figure 4.32.

Figure 4.32a and b show an illustration and snapshot of three layers of

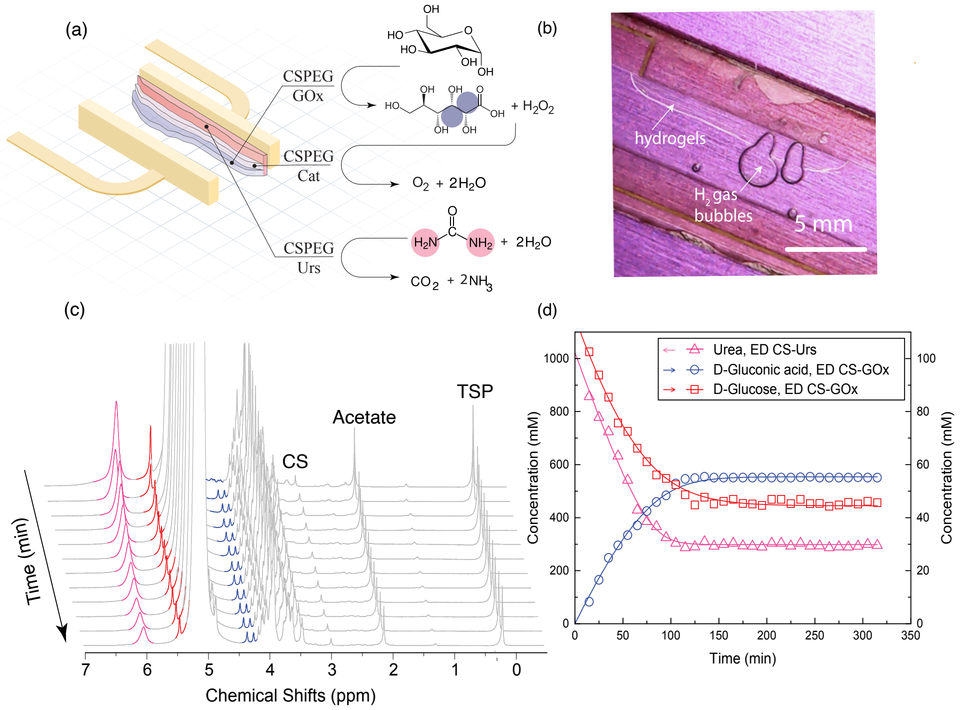

Figure 4.32 – (a) Illustration of the stack of immobilised enzymes with three different layers and the chemical reaction carried out in each layer; (b) Multi-layer hydrogel side by side to each other (3 layers beginning with CSPEG-Urs, CSPEG-cat and CSPEG-GOx); (c) real-time ^{1}H NMR spectra of the Urs and GOx enzymes kinetic at 500 MHz. Hydrolysis of urea (highlighted with pink, 5.8 ppm) as it is converted to NH_4^+ is shown as a function of increasing time, whereas the highlighted signal with blue at 4.2 ppm appear to be D-Gluconic acid and (d) extracted urea, D-Glucose and D-Gluconic acid concentrations from the NMR results in (c).*GOx experiments were always performed using GOx:Cat in a 4:1 ratio.

immobilised enzymes; Urs (in the first layer), catalase (2nd layer) and GOx (3rd layer) captured by microscopy. The detection area was positioned exactly in-between the sidewall electrodes; therefore, the layers of hydrogel were included in the detection. As shown in Figure 4.32c, the signal of the PEG linker was noticeable at 3.3 ppm. Furthermore, the proton signal of chitosan gel at 3.0 ppm is also visible. Surprisingly, NMR spectra show that urea (marked in pink) is only 70% consumed, while in the GOx reaction only 50% of the D-glucose (marked in red) is used during the reaction to produce D-gluconic acid (Figure 4.32d). Even though, the area of the working electrode in the sidewall platform (0.46 mm^2) is smaller than the area of the planar electrode (1.76 mm^2), but the volume of the deposited hydrogel for each layer in the sidewall platform is higher than in the planar platform, that is 175 ± 2 nL for CSPEG-Urs and 379 ± 4 nL for CSPEG-GOx layers versus 22.6 ± 0.2 nL for the CSPEG-Urs layer and 26.5 ± 0.3 nL for the CSPEG-GOx layer.

The NMR measurement revealed 3.50 ± 0.70 mU of Urs were present in the system. Given that the coupling yield was 41 %, the fraction of Urs that was active was then 24.4 ± 5 % (summarized in Table 4.5). As a comparison, the active fraction for Urs using sidewall platform is lower compared to planar platform, i.e. 24.4 ± 5 % versus 34.2 ± 5 %. This result demonstrated that after immobilisation of the enzymes in the narrow channel, using sidewall electrodes, the enzymes are not fully active. This could be due to changes to the immobilised enzyme caused by an electrostatic interaction with the matrix[154] (since the volume of hydrogel is larger). We did not observe this effect in the planar electrodes configuration.

The NMR measurements for GOx determined that 0.28 ± 0.01 mU were present and that the fraction of GOx (at a coupling yield of 35 %) that was active was 0.54 ± 0.02 %. The active fraction for GOx is less significant for both configurations and differs only by 0.01% (0.52 ± 0.12 % for the planar system). In contrast to the planar configuration, the consumption of the substrate, D-glucose to D-gluconic acid in the presence of the immobilized CSPEG-GOx on the third layer was less than 70%. This may be due to a similar issue as in CSPEG-Urs, where the immobilized CSPEG-GOx changes due to electrostatic interaction with the hydrogel matrix [154]. These results indicate that the activity of GOx was severely hampered, possibly due to the fact that the first immobilised enzyme was affected by steric hindrance of catalase, leading to insufficient oxygen access to the GOx layer[155].

The estimated Michaelis-Menten constants and the initial concentration slope for the multi-layer experiments for both configurations of the platform are shown in Table 4.5. The reagents and product concentration data for the model hydrolysis of urea and oxidation of D-Glucose reaction for both configurations exhibit exponential behaviour with time. This is consistent with a simple first order reaction kinetics. The values of $V_{\max}$ for the substrates, urea and D-glucose are similar for both enzymes, as was also shown in previous experiments. For the planar electrode the mean value ($\mathrm{V_{max}}$) of the Urs is $15.0 \pm 3\,\mathrm{mM/min}$, while for the sidewall electrode it is $12 \pm 2\,\mathrm{mM/min}$. For GOx in a planar system $V_{\max}$ is $0.9 \pm 0.1\,\mathrm{mM/min}$ while for the sidewall system $1.0 \pm 0.1\,\mathrm{mM/min}$.

This study shows that the reaction rate, $V_{\max}$ for the multiplex biosensor for multi-layered immobilised Urs and GOx is consistent with the reaction rate for the free enzymes in solution, either with or without coupling to the chitosan polymer, for both configurations. This is due to the fact that the same initial concentration S_0 of enzymes and substrates was used in all experiments. In addition, by using the different platform configurations such as planar electrodes and narrow channel sidewall electrodes, we confirmed a similar enzymatic activity in multi-layered hydrogels.

Concerning binding affinity, the CSPEG-Urs on the first layer of a multiplex reaction in a planar electrode setup showed K_M values higher than those of the same experiment on sidewall electrodes, namely $K_M = 540 \pm 118\,\mathrm{mM}$ versus $K_M = 125 \pm 79\,\mathrm{mM}$. A possible explanation is a reduced accessibility of the substrate, urea, to the active site of the immobilised CSPEG-Urs enzyme on the first layer. This may be due to either diffusion resistance of the stagnant solvent layers formed around the immobilised molecules or to the inclusion of enzyme molecules on the surface of the gel during the reaction [156]. The Michaelis constant, K_M of CSPEG-Urs in the sidewall electrode was lower than that of CSPEG-Urs on the planar electrode, indicating the increasing affinity of immobilised CSPEG-Urs for substrate binding in the enzymatic system. The immobilisation step increased the mass transfer rate between enzyme and enzyme (side by side). These kinetic parameters indicate that the diffusion of the reactants and products in the sidewall electrode case was higher compared to that of the planar electrode case, probably due to the spacing of the multilayered ones by co-immobilization (middle layer : CSPEG-catalase) accelerating the mass transfer efficiency. However, due to mass efficiency, the small substrate such as urea possibly stayed trapped within the active sites of the topmost immobilised layer (such as CSPEG-catalase and CSPEG-GOx), which led to a lower efficiency of the other immobilised enzymes.

For CSPEG-GOx, which is located in a multiplex system on the top layer (either x- or xy-plane of hydrogel), K_M values for both configurations are low: for the planar electrode it is $22 \pm 4\,\mathrm{mM}$ and for a sidewall electrode it is $23 \pm 8\,\mathrm{mM}$. Therefore, the substrate has easy access to the active sites on the gel surface. In terms of mass transfer efficiency, we found that the GOx activity for the sidewall electrodes case is much lower, although the volume of immobilised CSPEG-GOx and CSPEG-catalase should increase the activity of GOx compared to the planar electrode configuration.

Experiment	Initial Slope mM/ min	$V_{\max}$ mM/ min	K_m mM	Container Volume nl	Coupling efficiency -	Theoretical Units mU	Active Units mU	Active Fraction %
				Planar Electrode				
CSPEG-**Urs** / CSPEG-GOx*	14 ± 2	15 ± 3	540 ± 118	22.6 ± 0.2	0.41 ± 0.01	1.85 ± 0.05	0.63 ± 0.09	34.2 ± 5.0
CSPEG-Urs / CSPEG-**GOx***	0.90 ± 0.20	0.90 ± 0.10	22 ± 4	26.5 ± 0.3	0.41 ± 0.01	4.3 ± 1.2	0.024 ± 0.005	0.52 ± 0.12
				Sidewall Electrode				
CSPEG-**Urs** / CSPEG-GOx*	10 ± 2	12 ± 2	125 ± 79	175 ± 2	0.41 ± 0.01	14.3 ± 0.4	3.50 ± 0.70	24.4 ± 5
CSPEG-Urs / CSPEG-**GOx***	0.75 ± 0.02	1.0 ± 0.1	23 ± 8	379 ± 4	0.35 ± 0.01	53.3 ± 1.6	0.28 ± 0.01	0.54 ± 0.02

Table 4.5 – Summary of the kinetic activity of the multi-layered enzymes using two different geometries, planar and sidewall electrodes. Substrate solution composition was 1000 mM urea, 100 mM D-glucose (200 mM NaAc, pH 7 + 50 mM TSP) in each case. Each row reports the extracted data for the enzyme highlighted in **bold**. *Note: GOx is always prepared together with catalase in a 4:1 ratio.

4.6.7 Saddle coil versus microdetector Helmholtz coil

In this subsection, we compare enzymatic activity when it is determined by either a commercial saddle-coil NMR detector and a custom Helmholtz-coil microdetector. Protocols for monitoring the enzymatic reaction were described in section 3.4.1. The results are summarized in Figure 4.33. According to results reported in figure 4.33, the fraction of active units for Urs is slightly higher for the Micro 5 NMR detector with respect to the Helmholtz microdetector. The Urs activity shows that the Helmholtz microdetector is able to determine the fraction active unit with small volume, and the result is comparable to the commercial micro-5 NMR detector (Table 4.6).

On the other hand, GOx behaves differently. The sample volume has a great influence on the reaction of GOx, as oxygen gas is required to initiate the conversion of D-glucose to D-gluconic acid. As we have seen, the microfludic channel does not consume enough oxygen gas for D-glucose to be converted to 100% D-gluconic acid. In contrast, in the Micro 5 NMR detector, a sample volume of 500 µL is sufficient to accelerate the reaction of GOx to convert D-gluconic acid to D-gluconic acid (Appendix D.3-D.6). The results are summarized in table 4.6. Figure 4.33 shows that the fractional active unit of GOx in a bulk container is significantly higher than the fractional active unit in the microfluidic channel.

The best optimal pH for Urs in NaAc buffer is 6.4 and it has been reported that Urs can remain active from below pH 3 to 7.5 [156]. For GOx, it has been reported that the best optimal pH for the GOx reaction is in the range 5.5-7.5 [157]. In our multiplex experiments, the enzymatic reaction was maintained at pH 5.5 in NaAc buffer for both enzymes, although this is not the optimal pH. However, the fractional unit of the active enzyme shows that multiplexed enzymes bound to CSPEG have a higher activity compared to the free multiplex enzymes in a solution. This result shows that the CS polymer improves the buffers of the reaction for the enzyme Urs as measured by a pH indicator (4.29c). For GOx, the additional factor is the volume of the sample, which helps to improve the reaction of GOx measured with the saddle coil compared to the Helmholtz coil. The reason for this is similar to what explained above, which is due to the sufficient oxygen gas in the sample volume of 500 µL.

	Experiment	Initial Slope mM/ min	$V_{\max}$ mM/ min	K_M mM	Container Volume µl	Coupling Efficiency -	Theoretical Units U	Active Units U	Active Fraction %
Urs	Urs + Urea	24 ± 6	24 ± 7	712 ± 95	500 ± 6	-	100 ± 1.2	23.9 ± 5.8	23.9 ± 5.8
	CSPEG-Urs + Urs	25 ± 5	25 ± 5	601 ± 123	500 ± 6	0.41 ± 0.01	41 ± 1.1	25.4 ± 4.8	62.0 ± 11.8
	Urs / GOx* + D-Glucose, Urea	17 ± 3	17 ± 3	201 ± 21	500 ± 6	-	100 ± 1.2	17.0 ± 3.0	17.0 ± 3.0
	CSPEG-Urs/CSPEG-GOx* + D-Glucose, Urea	19 ± 2	19 ± 4	102 ± 10	500 ± 6	0.41 ± 0.01	41 ± 1.1	19.0 ± 2.0	46.3 ± 5.1
GOx	GOx + D-Glucose	2.5 ± 0.2	2.5 ± 0.2	228 ± 50	500 ± 6	-	200 ± 2.4	1.25 ± 0.10	0.6 ± 0.1
	CSPEG-GOx + D-Glucose	2.5 ± 0.1	2.5 ± 0.2	50 ± 12	500 ± 6	0.35 ± 0.01	70 ± 2.2	1.25 ± 0.05	1.8 ± 0.1
	Urs / GOx* + D-Glucose, Urea	2.4 ± 0.1	2.4 ± 0.1	28 ± 6	500 ± 6	-	200 ± 2.4	1.20 ± 0.05	0.60 ± 0.03
	CSPEG-Urs/CSPEG-GOx* + D-Glucose, Urea	2.6 ± 0.2	2.6 ± 0.3	30 ± 9	500 ± 6	0.35 ± 0.01	70 ± 2.2	1.30 ± 0.10	1.9 ± 0.2

Table 4.6 – Summary of the kinetic activity of **Urease** and **Glucose Oxidase** using using the commercial saddle coil. Kinetic parameters were extracted by fitting the consumption of urea and the production of D-gluconic acid, respectively. *Note: The reaction of the GOx enzyme is always linked to its co-enzyme, catalase, in a 4:1 ratio.

The V_{max} value calculated by Michaelis-Menten equations (based on 4.6 and 4.7) for the two enzymes Urs and GOx either with or without CSPEG shows consistency with the value as extracted from initial slope of the concentration time series curves. After various experiments performed under different conditions, maintaining a constant reagent:catalyst ratio, no significant difference in the maximum reaction rate (V_{max}) with respect to a conventional instrument was found[156].

It was shown that the K_M of Urs activity is practically independent of pH[158]. Meanwhile, the K_M values determined by free and immobilised enzymes for both Urs and GOx (with the help of catalase) agree quite well with the K_M values previously reported by Krajewska[138] (which depends on the concentration of urea) and Wu[155, 156, 159]. The method they used to determine K_M was not clearly described. The stability index of the nonlinear curve in our experiments is $R^2 > 0.98$, which illustrates the accuracy of the results obtained from all experiments. Therefore, this technique seems to be suitable for the determination of K_M and V_{max} of enzyme-catalyzed reactions, especially for reactions with rather high K_M values.

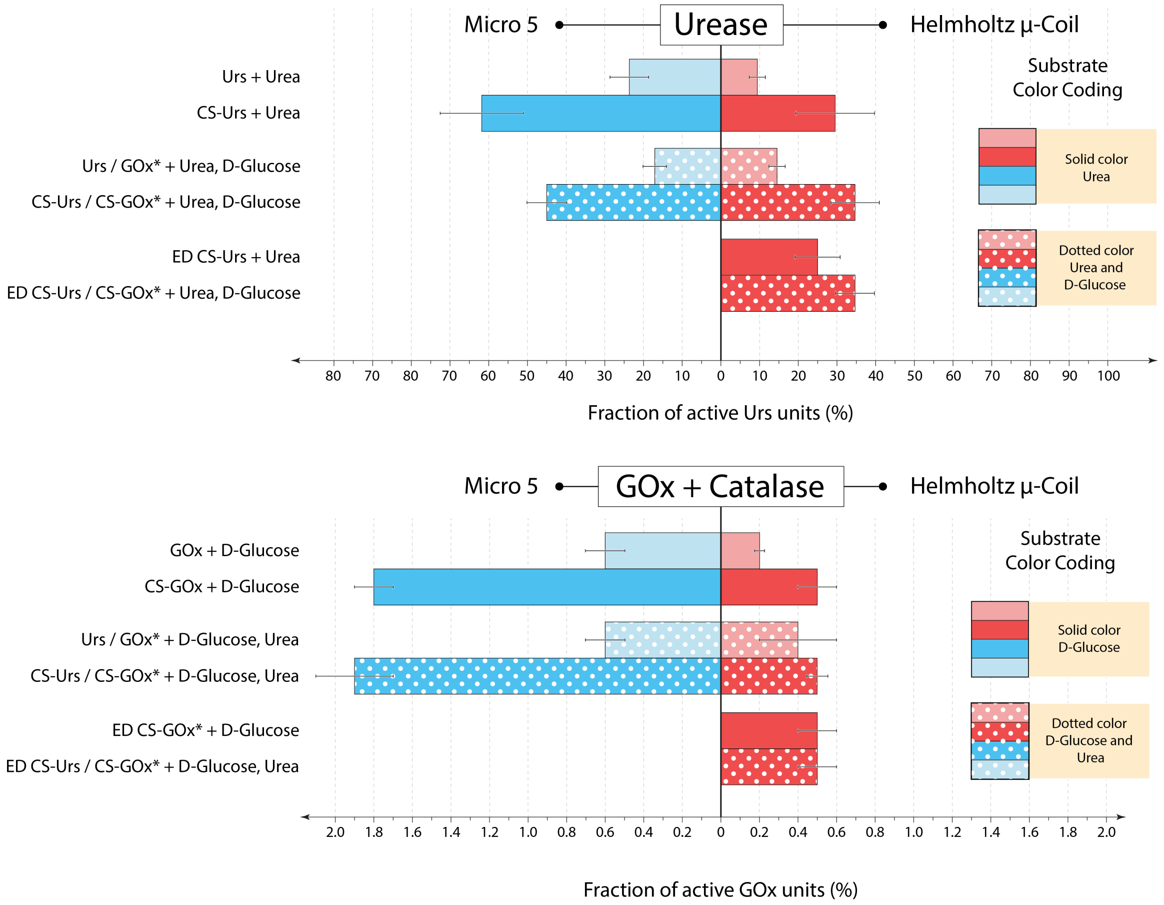

Figure 4.33 – Real-time display of the fraction of active units of two different enzymes using two different NMR detectors, Micro 5 and Helmholtz microcoil. Three different subcategories of experiments were grouped, i.e. single enzyme (one enzyme), multiplex (multi-layer enzymes) and electrodeposition of multiplex enzymes.

Chapter 5

General Conclusion

5.1 Miniaturisation of a chitosan electrodeposition setup

In this thesis we have designed, fabricated and tested electrodes arrays encapsulated within a microfluidic environment to demonstrate the ability to perform sequential electrodeposition of chitosan hydrogel in a parallel fashion. We also demonstrated that a stack of chitosan hydrogel stack can be functionalised to support either independent or interdependent chemical reactions. The miniaturization of this electrodeposition platform unlocks applicability of a multitude of microTAS technologies, e.g. controlling the hydrogel arrangement for biomimicking purposes and/or for reading out an interesting chemical signal from the composite chitosan stack.

Additionally, we demonstrated that a pair of electrodes can be patterned inside a microfluidic channel in a way that is compatible with an NMR microdetector, achieving strong integration with NMR spectroscopy. It is expected that a rational design of the electrode geometries is possible in order to minimise any deleterious effects in the recorded NMR signal. In the specific case of CS electrodeposition, the gel state can be used for chemical or physical immobilisation of analytes within the NMR detection volume.

5.2 Immobilisation of biological samples

Due to its inert nature, CS proves attractive for the immobilisation of enzymes; chitosan is an inexpensive and hydrophilic carrier material; it is biocompatible, biodegradable and non-toxic. By leveraging sequential electrodeposition of functionalised CS we implemented multiplex biosensing either independently or dependently through the coupling process. The gel state can be exploited for analyte immobilisation, either chemically or physically, within the NMR detection volume. For example, monitoring the in situ electrodeposition of CS and the in situ conversion of chemical reactants into products in real time proved to be one of the applications. On top of that, the possibility to immobilise enzymes takes us to another level of investigation of the enzymes function.

5.3 Towards application in metabolomics

The NMR-compatible microfluidic channel with integrated electrode opens up many applications, especially in biomedical applications and metabolomics. With this platform we were able to demonstrate the dynamics of immobilised enzymes within the NMR detection volume. Each stack of immobilised enzymes is independent of the individual substrates so that the products of the reactions can be controlled without affecting active sites of other enzymes in the chitosan hydrogel stack. This platform can was used for a biosensing application, the results of which were interpreted from NMR data using the Michaelis-Menten model.

Finally, this platform may increase the time efficiency in determining the function of biological samples. For example, this platform can be reused several times by rinsing the gel and loading new gel coupled with different biological samples (protein/enzymes). The loading operation takes less than 10 minutes while the acquisition time depends on the specific reaction rates but is generally in the order of 100 minutes. The reaction can then be monitored in situ using NMR spectroscopy. One can estimate that, under the assumption of an heavily automated loading procedure, between 100 and 1000 proteins could be processed in one week with an improved version of the presented platform.

Chapter 6

Limitation and Future Prospect

6.1 Limitation known issues affecting the ED platform

Limitations of the platform:

1. The current in situ ED platform does not allow for isolation of the sample insert (microfluidic chip) once it is flooded with solution. In case of delicate experiments where quantitative information is essential, diffusion of reagents and products into and out of the sample insert can be an issue. In a future revision of the device the addition of gated fluidics connectors could solve this problem. The gates could take the form of either electrically or mechanically actuated micro-valves, such as piezoelectric microvalves or membrane-based microvalves.
2. The current fabrication protocol for sidewall electrodes ED sample inserts is affected by a problem regarding the bonding step of the top glass wafer to the SU8. Due to the issue, the fraction of leaking chips over the produced total is high ($> 80\%$). During in-situ reaction or during experiments that take a long time, the issue leads to loss of the sample within the channel by evaporation. The leakage can also contaminate other components of the platform. Possible solutions include a redesign of the microfluidic channel, the use of different fabrication materials and a revision of the bonding process.
3. An essential step required for calibration of the CS ED using a specific

electrodes pair geometry was the deposition of quantum-dot-coupled chitosan gel. However, in the case of the sidewall electrodes design, characterisation by visualisation from a fluorescence spectrometer could not be implemented, because the SU-8 material used for structuring the insert fluidics fluoresces itself. The fluorescent emission of SU-8 superimposes over the emission of the chitosan coupled to quantum dots. In a future revision SU-8 can be replaced by another suitable material that does not fluoresce under UV light. Another alternative that can be considered is the installation of a band-blocking optical filter centered on the SU-8 emission wavelength.

6.2 Known issues affecting the electrodeposited gel

1. Chitosan does not work well as a substrate to perform the reactions on cell cultures. We were not able to determine any bacterial activity as chitosan kills bacterial cultures; there are many hypotheses about the observed bactericidal activity of chitosan, but almost all studies underline the crucial contribution of the polycationic nature of chitosan. The electrostatic interaction proves to be a fundamental feature of the killing potential, as the interaction with the negatively charged microbial surface dramatically affects bacterial vitality. However, given the variability of microbial surfaces, different organisms may release differently charged molecular patterns and react differently to chitosan. In a future revision, other potential gel substrates such as alginate and gelatine may be considered for *in vitro* study.

2. A suitable linker is required to increase the number of biomolecules that may bind to the chitosan polymer chain. In this work, we have shown that we can use PAMAM dendrimers to increase the number of "anchor points", i.e. the amine groups. However, the coupling yield of PAMAM dendrimers with bifunctional PEG linkers is low. This is due to the environment of the coupling process, which requires optimal conditions, such as pH 7 at room temperature for a prolonged time. Since chitosan also reacts to pH, chitosan forms a gel at this pH, which limits the EDC/NHS coupling chemistry reaction.

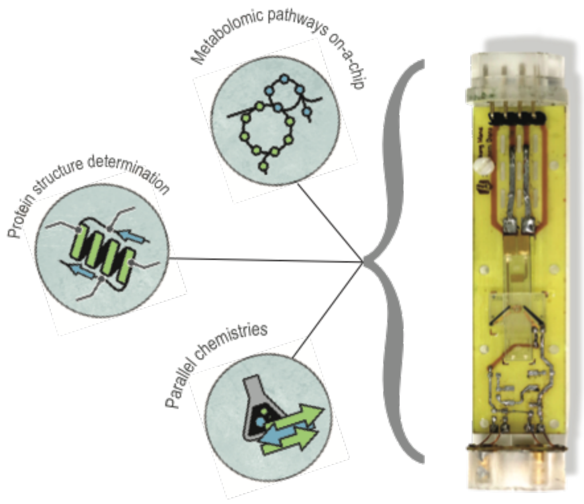
Metabolomic pathways on-a-chip
Protein structure determination
Parallel chemistries

6.3 Future Work

1. Chitosan hydrogel electrodeposition technology can be used to design and implement a platform for the replication of the metabolism of the living tissue. One such example is the liver sinusoid; by using the presented platform, an artificial liver sinusoid could be accurately grown out of chitosan hydrogel on a microfluidic insert. If successfully implemented, our solution would completely avoid the use of cell cultures on a chip and mimic liver zoning. In a future work, the idea can be implemented to set up a microfluidic platform containing a suitable electrode network and support structures so that the resulting structure corresponds topologically to an ideal liver sinusoid after deposition of chitosan.

2. The microfluidic platform can be redesigned to increase the number of electrochemical cells to achieve a high throughput parallel system. Pairs of electrochemical cells can be implemented on the microfluidic chips to increase the number of samples that allow the reaction to take place efficiently. For example, if the reaction can take place in situ in the NMR magnet, we do not need to interrupt one reaction by removing the probe and filling the channel for the second reaction. The reaction can be continuous and this does not modify the existing optimised shimming conditions.

Bibliography

[1] RCSB. PDB Statistics: Overall Growth of Released Structures Per Year, 2018. URL `http://www.rcsb.org/stats/growth/overall`. Accessed on 07.10.2020.

[2] D Williams Parsons, Siân Jones, Xiaosong Zhang, Jimmy Cheng-Ho Lin, Rebecca J Leary, Philipp Angenendt, Parminder Mankoo, Hannah Carter, I-Mei Siu, Gary L Gallia, and others. An integrated genomic analysis of human glioblastoma multiforme. *Science*, 321(5897):1807–1812, 2008.

[3] Dan Ye, Shenghong Ma, Yue Xiong, and Kun-Liang Guan. R-2-hydroxyglutarate as the key effector of IDH mutations promoting oncogenesis. *Cancer Cell*, 23(3):274–276, 2013.

[4] Elaine R Mardis, Li Ding, David J Dooling, David E Larson, Michael D McLellan, Ken Chen, Daniel C Koboldt, Robert S Fulton, Kim D Delehaunty, Sean D McGrath, and others. Recurring mutations found by sequencing an acute myeloid leukemia genome. *New England Journal of Medicine*, 361(11):1058–1066, 2009.

[5] Julie-Aurore Losman, Ryan E Looper, Peppi Koivunen, Sungwoo Lee, Rebekka K Schneider, Christine McMahon, Glenn S Cowley, David E Root, Benjamin L Ebert, and William G Kaelin. (R)-2-hydroxyglutarate is sufficient to promote leukemogenesis and its effects are reversible. *Science*, 339(6127):1621–1625, 2013.

[6] Mario Compiani and Emidio Capriotti. Computational and theoretical methods for protein folding. *Biochemistry*, 52(48):8601–8624, 2013.

[7] Jocelyne Fiaux, Eric B Bertelsen, Arthur L Horwich, and Kurt Wüthrich. NMR analysis of a 900K GroEL–GroES complex. *Nature*, 418(6894):207–211, 2002.

[8] Kurt Wüthrich. NMR studies of structure and function of biological macromolecules (Nobel Lecture). *Angewandte Chemie International Edition*, 42(29):3340–3363, 2003.

[9] Ursula K Nowak, Xiang Li, Andrew J Teuten, Richard A G Smith, and Christopher M Dobson. NMR studies of the dynamics of the multidomain protein urokinase-type plasminogen activator. *Biochemistry*, 32(1):298–309, 1993.

[10] Aaron K Chamberlain, Veronique Receveur, Andrew Spencer, Christina Redfield, and Christopher M Dobson. Characterization of the structure and dynamics of amyloidogenic variants of human lysozyme by NMR spectroscopy. *Protein Science*, 10(12): 2525–2530, 2001.

[11] Rawi Ramautar, Ruud Berger, Jan van der Greef, and Thomas Hankemeier. Human metabolomics: strategies to understand biology. *Current opinion in chemical biology*, 17(5):841–846, 2013.

[12] Jan Van Der Greef, Thomas Hankemeier, and Robert N McBurney. Metabolomics-based systems biology and personalized medicine: moving towards n= 1 clinical trials? *Pharmacogenomics*, 7(7):1087–1094, 2006. ISSN 14622416.

[13] Andrew M Wolters, Dimuthu A Jayawickrama, and Jonathan V Sweedler. Microscale nmr. *Current opinion in chemical biology*, 6(5):711–716, 2002.

[14] Vlad Badilita, Robert Ch Meier, Nils Spengler, Ulrike Wallrabe, Marcel Utz, and Jan G Korvink. Microscale nuclear magnetic resonance: a tool for soft matter research. *Soft Matter*, 8(41):10583–10597, 2012.

[15] Kalpana R Kamath and Kinam Park. Biodegradable hydrogels in drug delivery. *Advanced drug delivery reviews*, 11(1):59–84, 1993.

[16] W E Hennink and C F Van Nostrum. Novel crosslinking methods to design hydrogels. *Advanced drug delivery reviews*, 64:223–236, 2012.

[17] EH Schacht. Polymer chemistry and hydrogel systems. In *Journal of Physics Conference Series*, volume 3, pages 22–28. IOP Publishing, Gent Belgium, 2004. ISBN 1742-6596.

[18] Anna C Jen, M Conley Wake, and Antonios G Mikos. Review: Hydrogels for cell immobilization. *Biotechnology and bioengineering*, 50(4):357–364, 1996.

[19] Timothy A Becker, Daryl R Kipke, and Tedd Brandon. Calcium alginate gel: a biocompatible and mechanically stable polymer for endovascular embolization. *Journal of Biomedical Materials Research*, 54(1):76–86, 2001.

[20] Raquel De Souza, Payam Zahedi, Christine J Allen, and Micheline Piquette-Miller. Biocompatibility of injectable chitosan–phospholipid implant systems. *Biomaterials*, 30(23-24):3818–3824, 2009.

[21] Wendy A Petka, James L Harden, Kevin P McGrath, Denis Wirtz, and David A Tirrell. Reversible hydrogels from self-assembling artificial proteins. *Science*, 281(5375):389–392, 1998.

[22] Kangde Yao, Junjie Li, Fanglian Yao, and Yuji Yin. *Chitosan-based hydrogels: functions and applications*. CRC Press, Boca Raton Fl, 2011.

[23] Yihui Zhang, Fan Zhang, Zheng Yan, Qiang Ma, Xiuling Li, Yonggang Huang, and John A Rogers. Printing, folding and assembly methods for forming 3d mesostructures in advanced materials. *Nature Reviews Materials*, 2(4):1–17, 2017.

[24] Sanchita Bhattacharya, Franziska Eckert, Volodymyr Boyko, and Andrij Pich. Temperature-, pH-, and Magnetic-Field-Sensitive Hybrid Microgels. *Small*, 3(4):650–657, 2007.

[25] Allan S Hoffman. Applications of thermally reversible polymers and hydrogels in therapeutics and diagnostics. *Journal of Controlled Release*, 6(1):297–305, 1987.

[26] K Kontturi, S Mafe, J A Manzanares, B L Svarfvar, and P Viinikka. Modeling of the salt and pH effects on the permeability of grafted porous membranes. *Macromolecules*, 29(17):5740–5746, 1996.

[27] John H Holtz and Sanford A Asher. Polymerized colloidal crystal hydrogel films as intelligent chemical sensing materials. *Nature*, 389(6653):829–832, 1997.

[28] Ick Chan Kwon, You Han Bae, and Sung Wan Kim. Electrically credible polymer gel for controlled release of drugs. *Nature Cell Biology*, 354(6351):291–293, January 1991. ISSN 1465-7392. doi: 10.1038/354291a0.

[29] Takashi Miyata, Noriko Asami, and Tadashi Uragami. A reversibly antigen-responsive hydrogel. *Nature*, 399(6738):766–769, 1999.

[30] Ronald A Siegel and Bruce A Firestone. pH-dependent equilibrium swelling properties of hydrophobic polyelectrolyte copolymer gels. *Macromolecules*, 21(11):3254–3259, 1988.

[31] A Lengalova, V Pavli, P Saha, O Quadrat, and J Stejskal. The effect of dispersed particle size and shape on the electrorheological behaviour of suspensions. *Colloids and Surfaces A: Physicochemical and Engineering Aspects*, 227(1):1–8, 2003.

[32] Taeghwan Hyeon, Su Seong Lee, Jongnam Park, Yunhee Chung, and Hyon Bin Na. Synthesis of highly crystalline and monodisperse maghemite nanocrystallites without a size-selection process. *Journal of the American Chemical Society*, 123(51):12798–12801, 2001.

[33] Leonid Ionov, Sergiy Minko, Manfred Stamm, Jean-François Gohy, Robert Jérôme, and Andreas Scholl. Reversible chemical patterning on stimuli-responsive polymer film: Environment-responsive lithography. *Journal of the American Chemical Society*, 125 (27):8302–8306, 2003.

[34] David J Lestage, Min Yu, and Marek W Urban. Stimuli-responsive surfactant/phospholipid stabilized colloidal dispersions and their film formation. *Biomacromolecules*, 6(3):1561–1572, 2005.

[35] Chuanmin Ruan, Kefeng Zeng, Oomman K Varghese, and Craig A Grimes. Magnetoelastic Immunosensors: Amplified Mass Immunosorbent Assay for Detection of Escherichia c oli O157: H7. *Analytical Chemistry*, 75(23):6494–6498, 2003.

[36] Patrick S Stayton, Tsuyoshi Shimoboji, Cynthia Long, Ashutosh Chilkoti, Guohua Ghen, J Milton Harris, and Allan S Hoffman. Control of protein–ligand recognition using a stimuli-responsive polymer. *Nature*, 378:472–474, 1995.

[37] Jacques A Delaire and Keitaro Nakatani. Linear and nonlinear optical properties of photochromic molecules and materials. *Chemical reviews*, 100(5):1817–1846, 2000.

[38] Susan L R Barker, David Ross, Michael J Tarlov, Michael Gaitan, and Laurie E Locascio. Control of flow direction in microfluidic devices with polyelectrolyte multilayers. *Analytical Chemistry*, 72(24):5925–5929, 2000.

[39] Jun Chen, Haesun Park, and Kinam Park. Synthesis of superporous hydrogels: hydrogels with fast swelling and superabsorbent properties. *Journal of Biomedical Materials Research*, 44(1):53–62, 1999.

[40] Behzad Jafari, Farzaneh Rafie, and Soodabeh Davaran. Preparation and characterization of a novel smart polymeric hydrogel for drug delivery of insulin. *BioImpacts: BI*, 1(2):135, 2011.

[41] Botho Kickhöfen, Heinrich Wokalek, Doris Scheel, and Helga Ruh. Chemical and physical properties of a hydrogel wound dressing. *Biomaterials*, 7(1):67–72, 1986.

[42] Akira Matsumoto, Takehiko Ishii, Junko Nishida, Hiroko Matsumoto, Kazunori Kataoka, and Yuji Miyahara. A Synthetic Approach Toward a Self-Regulated Insulin Delivery System. *Angewandte Chemie International Edition*, 51(9):2124–2128, 2012.

[43] Tomomi Tanigo, Ryohei Takaoka, and Yasuhiko Tabata. Sustained release of water-insoluble simvastatin from biodegradable hydrogel augments bone regeneration. *Journal of Controlled Release*, 143(2):201–206, 2010.

[44] Akihiko Kikuchi and Teruo Okano. Pulsatile drug release control using hydrogels. *Advanced drug delivery reviews*, 54(1):53–77, 2002.

[45] David Cunliffe, Carolina de las Heras Alarcón, Vanessa Peters, James R Smith, and Cameron Alexander. Thermoresponsive surface-grafted poly (N-isopropylacrylamide) copolymers: effect of phase transitions on protein and bacterial attachment. *Langmuir*, 19(7):2888–2899, 2003.

[46] L K Ista and G P Lopez. Lower critical solubility temperature materials as biofouling release agents. *Journal of Industrial Microbiology and Biotechnology*, 20(2):121–125, 1998.

[47] Allan S Hoffman. Hydrogels for biomedical applications. *Advanced drug delivery reviews*, 64:18–23, 2012.

[48] CE Coulthard, R Michaelis, WF Short, G Sykes, GEH Skrimshire, AFB Standfast, JH Birkinshaw, and H Raistrick. Notatin: an anti-bacterial glucose-aerodehydrogenase from penicillium notatum westling and penicillium resticulosum sp. nov. *Biochemical Journal*, 39(1):24–36, 1945.

[49] John A Rogers, Kateri E Paul, Rebecca J Jackman, and George M Whitesides. Using an elastomeric phase mask for sub-100 nm photolithography in the optical near field. *Applied physics letters*, 70(20):2658–2660, 1997.

[50] Timothy L Peck, Richard L Magin, and Paul C Lauterbur. Design and analysis of microcoils for NMR microscopy. *Journal of Magnetic Resonance, Series B*, 108(2): 114–124, 1995.

[51] E W McFarland and A Mortara. Three-dimensional NMR microscopy: improving SNR with temperature and microcoils. *Magnetic resonance imaging*, 10(2):279–288, 1992.

[52] Dean L Olson, Timothy L Peck, Andrew G Webb, Richard L Magin, and Jonathan V Sweedler. High-resolution microcoil 1H-NMR for mass-limited, nanoliter-volume samples. *Science*, 270(5244):1967–1970, 1995.

[53] K Yamauchi, J W G Janssen, and A P M Kentgens. Implementing solenoid microcoils for wide-line solid-state NMR. *Journal of Magnetic Resonance*, 167(1):87–96, 2004.

[54] L Ciobanu, D A Seeber, and C H Pennington. 3D MR microscopy with resolution 3.7 μm by 3.3 μm by 3.3 μm. *Journal of Magnetic Resonance*, 158(1-2):178–182, 2002.

[55] David I Hoult and R E Richards. The signal-to-noise ratio of the nuclear magnetic resonance experiment. *Journal of Magnetic Resonance (1969)*, 24(1):71–85, 1976.

[56] P J M Van Bentum, J W G Janssen, A P M Kentgens, J Bart, and Johannes G E Gardeniers. Stripline probes for nuclear magnetic resonance. *Journal of magnetic resonance*, 189(1):104–113, 2007.

[57] Jacob Bart. *Stripline-based microfluidic devices for high-resolution NMR spectroscopy.* Wöhrmann Print Service, Zutphen, The Netherlands, 2009.

[58] J Bart, J W G Janssen, P J M Van Bentum, A P M Kentgens, and Johannes G E Gardeniers. Optimization of stripline-based microfluidic chips for high-resolution NMR. *Journal of magnetic resonance*, 201(2):175–185, 2009.

[59] Yael Maguire, Isaac L Chuang, Shuguang Zhang, and Neil Gershenfeld. Ultra-small-sample molecular structure detection using microslot waveguide nuclear spin resonance. *Proceedings of the National Academy of Sciences*, 104(22):9198–9203, 2007.

[60] N. Spengler, A. Moazenzadeh, R. Ch Meier, V. Badilita, J. G. Korvink, and U. Wallrabe. Micro-fabricated Helmholtz coil featuring disposable microfluidic sample inserts for applications in nuclear magnetic resonance. *Journal of Micromechanics and Microengineering*, 2014. ISSN 13616439. doi: 10.1088/0960-1317/24/3/034004.

[61] Lorenzo Bordonali, Nurdiana Nordin, Erwin Fuhrer, Neil MacKinnon, and Jan G Korvink. Parahydrogen based nmr hyperpolarisation goes micro: an alveolus for small molecule chemosensing. *Lab on a Chip*, 19(3):503–512, 2019.

[62] Jung Jin Park, Xiaolong Luo, Hyunmin Yi, Reza Ghodssi, and Gary W. Rubloff. In situ biomolecule assembly and activity within completely packaged microfluidic devices. In *2006 IEEE/NLM Life Science Systems and Applications Workshop, LiSA 2006*, volume 1, pages 1315–1321. IEEE, Bethesda, MD, USA, 2006.

[63] Yi Cheng, Xiaolong Luo, Gregory F Payne, and Gary W Rubloff. Biofabrication: programmable assembly of polysaccharide hydrogels in microfluidics as biocompatible scaffolds. *Journal of Materials Chemistry*, 22(16):7659–7666, 2012.

[64] Gregory F. Payne and Srinivasa R. Raghavan. Chitosan: a soft interconnect for hierarchical assembly of nano-scale components. *Soft Matter*, 3(5):521, 2007. ISSN 1744-683X. doi: 10.1039/b613872a.

[65] Lei Yu, Qi Sun, Yue Hui, Arjun Seth, Nikolai Petrovsky, and Chun-Xia Zhao. Microfluidic formation of core-shell alginate microparticles for protein encapsulation and controlled release. *Journal of colloid and interface science*, 539:497–503, 2019.

[66] Li-Qun Wu, Anand P Gadre, Hyunmin Yi, Mark J Kastantin, Gary W Rubloff, William E Bentley, Gregory F Payne, and Reza Ghodssi. Voltage-dependent assembly of the polysaccharide chitosan onto an electrode surface. *Langmuir*, 18(22):8620–8625, 2002.

[67] Yong Qiu and Kinam Park. Environment-sensitive hydrogels for drug delivery. *Advanced drug delivery reviews*, 53(3):321–339, 2001.

[68] Robert Langer and Nicholas A. Peppas. Advances in Biomaterials, Drug Delivery, and Bionanotechnology. In *AIChE Journal*, volume 49, pages 2990–3006, 2003. ISBN 0001-1541. doi: 10.1002/aic.690491202.

[69] Anil Kumar Bajpai, Sandeep K Shukla, Smitha Bhanu, and Sanjana Kankane. Responsive polymers in controlled drug delivery. *Progress in Polymer Science*, 33(11): 1088–1118, 2008.

[70] Kang Moo Huh, Han Chang Kang, Young Ju Lee, and You Han Bae. ph-sensitive polymers for drug delivery. *Macromolecular research*, 20(3):224–233, 2012.

[71] Tao Wang, Mahir Turhan, and Sundaram Gunasekaran. Selected properties of pH-sensitive, biodegradable chitosan–poly (vinyl alcohol) hydrogel. *Polymer International*, 53(7):911–918, 2004.

[72] Seon Jeong Kim, Seoung Gil Yoon, Sang Min Lee, Sang Hoon Lee, and Sun I Kim. Electrical sensitivity behavior of a hydrogel composed of polymethacrylic acid/poly (vinyl alcohol). *Journal of Applied Polymer Science*, 91(6):3613–3617, 2004.

[73] Jérôme Berger, Marianne Reist, Joachim M Mayer, Olivia Felt, N A Peppas, and R Gurny. Structure and interactions in covalently and ionically crosslinked chitosan hydrogels for biomedical applications. *European Journal of Pharmaceutics and Biopharmaceutics*, 57(1):19–34, 2004.

[74] P Arthur Felse and T Panda. Studies on applications of chitin and its derivatives. *Bioprocess Engineering*, 20(6):505–512, 1999.

[75] Olivia Felt, Pierre Buri, and Robert Gurny. Chitosan: a unique polysaccharide for drug delivery. *Drug development and industrial pharmacy*, 24(11):979–993, 1998.

[76] Barbara Krajewska, Maciej Leszko, and Wiesawa Zaborska. Urease immobilized on chitosan membrane: Preparation and properties. *Journal of Chemical Technology & Biotechnology*, 48(3):337–350, 1990. doi: 10.1002/jctb.280480309.

[77] A K Singla and M Chawla. Chitosan: Some pharmaceutical and biological aspects-an update. *Journal of Pharmacy and Pharmacology*, 53(8):1047–1067, 2001.

[78] Hyunmin Yi, Li-Qun Wu, William E Bentley, Reza Ghodssi, Gary W Rubloff, James N Culver, and Gregory F Payne. Biofabrication with chitosan. *Biomacromolecules*, 6(6): 2881–2894, 2005.

[79] Majeti N V Ravi Kumar. A review of chitin and chitosan applications. *Reactive and functional polymers*, 46(1):1–27, 2000.

[80] Xin Pang, Travis Casagrande, and Igor Zhitomirsky. Electrophoretic deposition of {hydroxyapatite–CaSiO3–chitosan} composite coatings. *Journal of Colloid and Interface Science*, 330(2):323, 2009. ISSN 0021-9797. doi: 10.1016/j.jcis.2008.10.070.

[81] F Pishbin, A Simchi, M P Ryan, and A R Boccaccini. Electrophoretic deposition of chitosan/45S5 Bioglass® composite coatings for orthopaedic applications. *Surface and Coatings Technology*, 205(23):5260–5268, 2011.

[82] Jody Redepenning, Guhanand Venkataraman, Jun Chen, and Nathan Stafford. Electrochemical preparation of chitosan/hydroxyapatite composite coatings on titanium substrates. *Journal of Biomedical Materials Research Part A*, 66(2):411–416, 2003.

[83] Rebecca A Zangmeister, Jung J Park, Gary W Rubloff, and Michael J Tarlov. Electrochemical study of chitosan films deposited from solution at reducing potentials. *Electrochimica acta*, 51(25):5324–5333, 2006.

[84] Rohan Fernandes, Hyunmin Yi, Li-Qun Wu, Gary W Rubloff, Reza Ghodssi, William E Bentley, and Gregory F Payne. Thermo-biolithography: A technique for patterning nucleic acids and proteins. *Langmuir*, 20(3):906–913, 2004.

[85] Xiaolong Luo, Angela T Lewandowski, Hyunmin Yi, Gregory F Payne, Reza Ghodssi, William E Bentley, and Gary W Rubloff. Programmable assembly of a metabolic pathway enzyme in a pre-packaged reusable bioMEMS device. *Lab on a Chip*, 8(3): 420–430, 2008.

[86] Angela T Lewandowski, Hyunmin Yi, Xiaolong Luo, Gregory F Payne, Reza Ghodssi, Gary W Rubloff, and William E Bentley. Protein assembly onto patterned microfabricated devices through enzymatic activation of fusion pro-tag. *Biotechnology and bioengineering*, 99(3):499–507, 2008.

[87] Hyunmin Yi, Li Qun Wu, Reza Ghodssi, Gary W. Rubloff, Gregory F. Payne, and William E. Bentley. Signal-directed sequential assembly of biomolecules on patterned surfaces. *Langmuir*, 21(6):2104–2107, 2005. ISSN 07437463. doi: 10.1021/la047529k.

[88] Hyunmin Yi, Saira Nisar, Sang Yup Lee, Michael A. Powers, William E. Bentley, Gregory F. Payne, Reza Ghodssi, Gary W. Rubloff, Michael T. Harris, and James N. Culver. Patterned assembly of genetically modified viral nanotemplates via nucleic acid hybridization. *Nano Letters*, 5(10):1931–1936, 2005. ISSN 15306984. doi: 10.1021/nl051254r.

[89] Aishling Dunne, Wayne Francis, Larisa Florea, Fernando Benito-Lopez, and Dermot Diamond. Biocompatible, reversible photo-actuated hydrogels, operative in neutral environments, for micro-valve applications in microfluidic devices. In *18th International Conference on Miniaturized Systems for Chemistry and Life Sciences, San Antonio, United States*, volume 1, pages 1871–1873. Miniaturized Systems for Chemistry and Life Sciences, San Antonio, Texas, United States, 2014.

[90] Yi Cheng, Xiaolong Luo, Chen-Yu Tsao, Hsuan-Chen Wu, Jordan Betz, Gregory F Payne, William E Bentley, and Gary W Rubloff. Biocompatible multi-address 3D cell assembly in microfluidic devices using spatially programmable gel formation. *Lab on a Chip*, 11(14):2316–2318, 2011.

[91] Yi Liu, Jessica L. Terrell, Chen Yu Tsao, Hsuan Chen Wu, Vishal Javvaji, Eunkyoung Kim, Yi Cheng, Yifeng Wang, Rein V. Ulijn, Srinivasa R. Raghavan, Gary W. Rubloff, William E. Bentley, and Gregory F. Payne. Biofabricating multifunctional soft matter with enzymes and stimuli-responsive materials. *Advanced Functional Materials*, 22(14): 3004–3012, 2012. ISSN 1616301X. doi: 10.1002/adfm.201200095.

[92] James Keeler. *Understanding NMR spectroscopy.* John Wiley & Sons, Cambridge, UK, 2011.

[93] Anatole Abragam. *The principles of nuclear magnetism*, volume 32. Oxford university press, UK, 1961.

[94] Michael E Lacey, Raju Subramanian, Dean L Olson, Andrew G Webb, and Jonathan V Sweedler. High-resolution nmr spectroscopy of sample volumes from 1 nl to 10 μl. *Chemical reviews*, 99(10):3133–3152, 1999.

[95] Maximilian Focke, Dominique Kosse, Claas Müller, Holger Reinecke, Roland Zengerle, and Felix von Stetten. Lab-on-a-Foil: microfluidics on thin and flexible films. *Lab on a Chip*, 10(11):1365, 2010. ISSN 1473-0197. doi: 10.1039/c001195a.

[96] Martin Licht, Martin Straub, Karsten König, Maziar Afshar, Dara Feili, and Helmut Seidel. Three-dimensional polymer nanostructures for applications in cell biology generated by high-repetition rate sub-15 fs near-infrared laser pulses. In *Nanoscale Imaging, Sensing, and Actuation for Biomedical Applications VIII*, volume 7908, page

79080M. International Society for Optics and Photonics, San Francisco, California, United States, 2011.

[97] Amara Apilux, Wijitar Dungchai, Weena Siangproh, Narong Praphairaksit, Charles S Henry, and Orawon Chailapakul. Lab-on-paper with dual electrochemical/colorimetric detection for simultaneous determination of gold and iron. *Analytical chemistry*, 82(5): 1727–1732, 2010.

[98] Shaopeng Wang, Natalia Mamedova, Nicholas A Kotov, Wei Chen, and Joe Studer. Antigen/antibody immunocomplex from CdTe nanoparticle bioconjugates. *Nano letters*, 2(8):817–822, 2002.

[99] Yi Liu, Boce Zhang, Kelsey M. Gray, Yi Cheng, Eunkyoung Kim, Gary W. Rubloff, William E. Bentley, Qin Wang, and Gregory F. Payne. Electrodeposition of a weak polyelectrolyte hydrogel: remarkable effects of salt on kinetics, structure and properties. *Soft Matter*, 9(9), 2013. ISSN 1744-683X. doi: 10.1039/c3sm27581g.

[100] Oliver G. Gruschke, Nicoleta Baxan, Lars Clad, Kai Kratt, Dominik von Elverfeldt, Andreas Peter, Jürgen Hennig, Vlad Badilita, Ulrike Wallrabe, and Jan G. Korvink. Lab on a chip phased-array MR multi-platform analysis system. *Lab on a chip*, 12(3): 495–502, 2012. doi: 10.1039/c2lc20585h.

[101] Kun Yan, Fuyuan Ding, William E. Bentley, Hongbing Deng, Yumin Du, Gregory F. Payne, and Xiao-Wen Shi. Coding for hydrogel organization through signal guided self-assembly. *Soft Matter*, 10(3):465–469, 2014. ISSN 1744-683X. doi: 10.1039/C3SM52405A.

[102] Kun Yan, Yi Liu, Jitao Zhang, Santiago O Correa, Wu Shang, Cheng-Chieh Tsai, William E Bentley, Jana Shen, Giuliano Scarcelli, Christopher B Raub, Xiao-Wen Shi, and Gregory F Payne. Electrical Programming of Soft Matter: Using Temporally Varying Electrical Inputs To Spatially Control Self Assembly. *Biomacromolecules*, 19 (2):364–373, 2018.

[103] Kun Yan, Yuan Xiong, Si Wu, William E Bentley, Hongbing Deng, Yumin Du, Gregory F Payne, and Xiao-Wen Shi. Electro-molecular assembly: electrical writing of information into an erasable polysaccharide medium. *ACS Applied Materials & Interfaces*, 8(30):19780–19786, 2016.

[104] Junhua Wang, Li Wang, Haojie Yu, Zain-ul-Abdin, Yongsheng Chen, Qing Chen, Weidong Zhou, Hongtao Zhang, and Xiao Chen. Recent progress on synthesis, property and application of modified chitosan: An overview. *International Journal of Biological Macromolecules*, 88:333, 2016.

[105] Jing Ji, Li Wang, Haojie Yu, Yongsheng Chen, Yulai Zhao, Hongtao Zhang, Wael A Amer, Yubiao Sun, Liang Huang, and Muhammad Saleem. Chemical Modifications of Chitosan and Its Applications. *Polymer-Plastics Technology and Engineering*, 53(14): 1494, 2014.

[106] Sébastien Ladet, Laurent David, and Alain Domard. Multi-membrane hydrogels. *Nature*, 452(7183):76–79, 3 2008.

[107] Nurdiana Nordin, Lorenzo Bordonali, Vlad Badilita, and Neil MacKinnon. Spatial and temporal control over multilayer bio-polymer film assembly and composition. *Macromolecular bioscience*, 19(4):1800372, 2019.

[108] Asako Hirai, Hisashi Odani, and Akio Nakajima. Determination of degree of deacetylation of chitosan by 1H NMR spectroscopy. *Polymer Bulletin*, 26(1):87, 1991.

[109] H Sashiwa, Y Shigemasa, and R Roy. Highly Convergent Synthesis of Dendrimerized Chitosan{\textminus}Sialic Acid Hybrid. *Macromolecules*, 34(10):3211, 2001.

[110] Hitoshi Sashiwa, Yoshihiro Shigemasa, and René Roy. Chemical modification of chitosan 11: chitosan{\textendash}dendrimer hybrid as a tree like molecule. *Carbohydrate Polymers*, 49(2):195, 2002.

[111] Yanhui Niu, Li Sun, and Richard M. Crooks. Determination of the intrinsic proton binding constants for poly(amidoamine) dendrimers via potentiometric pH titration. *Macromolecules*, 36(15):5725–5731, 2003. ISSN 00249297. doi: 10.1021/ma034276d.

[112] Junjie Deng, Yanfang Zhou, Bo Xu, Kaijin Mai, Yubin Deng, and Li-Ming Zhang. Dendronized chitosan derivative as a biocompatible gene delivery carrier. *Biomacromolecules*, 12(3):642–649, 1 2011.

[113] Kishor Sarkar and P P Kundu. Preparation of low molecular weight N-maleated chitosan-graft-PAMAM copolymer for enhanced DNA complexation. *International Journal of Biological Macromolecules*, 51(5):859–867, 7 2012.

[114] Rohan Fernandes, Li-Qun Wu, Tianhong Chen, Hyunmin Yi, Gary W Rubloff, Reza Ghodssi, William E Bentley, and Gregory F Payne. Electrochemically induced deposition of a polysaccharide hydrogel onto a patterned surface. *Langmuir*, 19(10):4058–4062, 2003.

[115] Kelsey M Gray, Benjamin D Liba, Yifeng Wang, Yi Cheng, Gary W Rubloff, William E Bentley, Alexandra Montembault, Isabelle Royaud, Laurent David, and Gregory F Payne. Electrodeposition of a biopolymeric hydrogel: potential for one-step protein electroaddressing. *Biomacromolecules*, 13(4):1181–1189, 2012.

[116] C Qiu, M Chen, H Yan, and H K Wu. Generation of uniformly sized alginate microparticles for cell encapsulation by using a soft-lithography approach. *Advanced Materials*, 19(12):1603, 2007. ISSN 0935-9648. doi: 10.1002/adma.200602574.

[117] Yi Cheng, Xiaolong Luo, Jordan Betz, Susan Buckhout-White, Omar Bekdash, Gregory F Payne, William E Bentley, and Gary W Rubloff. In situ quantitative visualization and characterization of chitosan electrodeposition with paired sidewall electrodes. *Soft Matter*, 6(14):3177–3183, 2010.

[118] Matthias C Wapler, Jochen Leupold, Iulius Dragonu, Dominik von Elverfeld, Maxim Zaitsev, and Ulrike Wallrabe. Magnetic properties of materials for mr engineering, micro-mr and beyond. *Journal of magnetic resonance*, 242:233–242, 2014.

[119] John F Schenck. The role of magnetic susceptibility in magnetic resonance imaging: Mri magnetic compatibility of the first and second kinds. *Medical physics*, 23(6):815–850, 1996.

[120] Giulio Milazzo, Sergio Caroli, and Robert D Braun. Tables of standard electrode potentials. *Journal of The Electrochemical Society*, 125(6):261C, 1978. doi: 10.1149/1.2131790.

[121] AllenJ Bard. *Standard potentials in aqueous solution.* Routledge, New York, United States, 2017.

[122] Zenghua Geng, Xia Wang, Xuecheng Guo, Zheng Zhang, Yanjun Chen, and Yifeng Wang. Electrodeposition of chitosan based on coordination with metal ions in situ-generated by electrochemical oxidation. *Journal of Materials Chemistry B*, 4(19):3331–3338, 2016. doi: 10.1039/C6TB00336B.

[123] Shih-Hao Huang, Lu-Shiuan Wei, Hsiao-Tzu Chu, and Yeu-Long Jiang. Light-addressed electrodeposition of enzyme-entrapped chitosan membranes for multiplexed enzyme-based bioassays using a digital micromirror device. *Sensors*, 13(8):10711–10724, 2013.

[124] Li-Qun Wu, Kyuyong Lee, Xiang Wang, Douglas S English, Wolfgang Losert, and Gregory F Payne. Chitosan-mediated and spatially selective electrodeposition of nanoscale particles. *Langmuir*, 21(8):3641–3646, 2005.

[125] Yi Cheng, Xiaolong Luo, Jordan Betz, Susan Buckhout-White, Omar Bekdash, Gregory F Payne, William E Bentley, and Gary W Rubloff. In situ quantitative visualization and characterization of chitosan electrodeposition with paired sidewall electrodes. *Soft Matter*, 6(14):3177–3183, 2010.

[126] Nikolaus M Loening, Michael J Thrippleton, James Keeler, and Robert G Griffin. Single-scan longitudinal relaxation measurements in high-resolution nmr spectroscopy. *Journal of Magnetic Resonance*, 164(2):321–328, 2003.

[127] Michael J Thrippleton, Richard AE Edden, and James Keeler. Suppression of strong coupling artefacts in j-spectra. *Journal of Magnetic Resonance*, 174(1):97–109, 2005.

[128] AG Webb. Radiofrequency microcoils for magnetic resonance imaging and spectroscopy. *Journal of Magnetic Resonance*, 229:55–66, 2013.

[129] Zu-Rong Ni, Xiao-Hong Cui, Shuo-Hui Cao, and Zhong Chen. A novel in situ electrochemical nmr cell with a palisade gold film electrode. *AIP Advances*, 7(8):085205, 2017.

[130] Pollyana Ferreira Da Silva, Bruna Ferreira Gomes, Carlos Manuel Silva Lobo, Luiz Henrique Keng Queiroz Júnior, Ernesto Danieli, Marcelo Carmo, Bernhard Blümich, and Luiz Alberto Colnago. Electrochemical nmr spectroscopy: Electrode construction and magnetic sample stirring. *Microchemical Journal*, 146:658–663, 2019.

[131] Bruna Ferreira Gomes, Pollyana Ferreira da Silva, Carlos Manuel Silva Lobo, Maiara da Silva Santos, and Luiz Alberto Colnago. Strong magnetoelectrolysis effect during electrochemical reaction monitored in situ by high-resolution nmr spectroscopy. *Analytica chimica acta*, 983:91–95, 2017.

[132] Eric G Sorte, Safia Jilani, and YuYe J Tong. Methanol and ethanol electrooxidation on ptru and ptnicu as studied by high-resolution in situ electrochemical nmr spectroscopy with interdigitated electrodes. *Electrocatalysis*, 8(2):95–102, 2017.

[133] Eric G. Sorte, Nathan A. Banek, Michael J. Wagner, Todd M. Alam, and YuYe J. Tong. In Situ Stripline Electrochemical NMR for Batteries. *ChemElectroChem*, 5(17): 2336–2340, 2018. doi: 10.1002/celc.201800434.

[134] YuYe J. Tong. In situ electrochemical nuclear magnetic resonance spectroscopy for electrocatalysis: Challenges and prospects. *Current Opinion in Electrochemistry*, 4(1): 60–68, 2017. doi: 10.1016/j.coelec.2017.09.017.

[135] Robert K Andrews, Robert L Blakeley, and Burt Zerner. Urea and urease. *Advances in inorganic biochemistry*, 6(6):245–283, 1984.

[136] HL Mobley and RP Hausinger. Microbial ureases: significance, regulation, and molecular characterization. *Microbiology and Molecular Biology Reviews*, 53(1):85–108, 1989.

[137] Michael J Maroney and Stefano Ciurli. Nonredox nickel enzymes. *Chemical reviews*, 114(8):4206–4228, 2014.

[138] Barbara Krajewska. Ureases I. Functional, catalytic and kinetic properties: A review. *Journal of Molecular Catalysis B: Enzymatic*, 59(1-3):9–21, 2009. ISSN 13811177. doi: 10.1016/j.molcatb.2009.01.003.

[139] Stefanie Pluschkell, Karsten Hellmuth, and Ursula Rinas. Kinetics of glucose oxidase excretion by recombinant aspergillus niger. *Biotechnology and Bioengineering*, 51(2): 215–220, 1996.

[140] D G Hatzinikolaou, O C Hansen, BJ Macris, A Tingey, D Kekos, P Goodenough, and P Stougaard. A new glucose oxidase from aspergillus niger: characterization and regulation studies of enzyme and gene. *Applied microbiology and biotechnology*, 46(4): 371–381, 1996.

[141] Susanne Witt, Gerd Wohlfart, Dietmar Schomburg, Hans-Jürgen Hecht, and Henryk M Kalisz. Conserved arginine-516 of penicillium amagasakiense glucose oxidase is essential for the efficient binding of β-d-glucose. *Biochemical Journal*, 347(2):553–559, 2000.

[142] Cor FB Witteveen, Marten Veenhuis, and Jaap Visser. Localization of glucose oxidase and catalase activities in aspergillus niger. *Applied and environmental microbiology*, 58 (4):1190–1194, 1992.

[143] D Keilin and EF Hartree. Specificity of glucose oxidase (notatin). *Biochemical Journal*, 50(3):331–341, 1952.

[144] David Keilin and EF Hartree. The use of glucose oxidase (notatin) for the determination of glucose in biological material and for the study of glucose-producing systems by manometric methods. *Biochemical Journal*, 42(2):230–238, 1948.

[145] D Keilin and E F Hartree. Properties of glucose oxidase (notatin): Addendum. Sedimentation and diffusion of glucose oxidase (notatin). *Biochemical journal*, 42(2):221, 1948.

[146] Wylie Stroberg and Santiago Schnell. On the estimation errors of km and v from time-course experiments using the michaelis-menten equation. *Biophysical Chemistry*, 219: 17 – 27, 2016. ISSN 0301-4622. doi: https://doi.org/10.1016/j.bpc.2016.09.004.

[147] Dan Yang, Junhe Fan, Fengyi Cao, Zuojun Deng, John A Pojman, and Lin Ji. Immobilization adjusted clock reaction in the urea–urease–h+ reaction system. *RSC advances*, 9(7):3514–3519, 2019.

[148] Stacey F Howell and James B Sumner. The specific effects of buffers upon urease activity. *Journal of Biological Chemistry*, 104(3):619–626, 1934.

[149] Kwabena Sarfo, Helen H Petach, and William Henderson. Polymeric phosphine oxide polyether-derived copolymer as a support for urease immobilization. *Enzyme and microbial technology*, 17(9):804–808, 1995.

[150] JP Chen and SH Chiu. Preparation and characterization of urease immobilized onto porous chitosan beads for urea hydrolysis. *Bioprocess Engineering*, 21(4):323–330, 1999.

[151] Min-Hua Xue, Qin Xu, Mi Zhou, and Jun-Jie Zhu. In situ immobilization of glucose oxidase in chitosan–gold nanoparticle hybrid film on prussian blue modified electrode for high-sensitivity glucose detection. *Electrochemistry communications*, 8(9):1468–1474, 2006.

[152] Ali Yilmaz and Marcel Utz. Characterisation of oxygen permeation into a microfluidic device for cell culture by in situ NMR spectroscopy. *Lab on a Chip*, 16(11):2079, 2016. ISSN 1473-0189. doi: 10.1039/c6lc00396f.

[153] Hossein Davoodi, Nurdiana Nordin, Lorenzo Bordonali, Jan G Korvink, Neil MacKinnon, and Vlad Badilita. An nmr-compatible microfluidic platform enabling in situ electrochemistry. *Lab on a Chip*, 20(17):3202–3212, 2020. doi: 10.1039/D0LC00364F.

[154] Sachin Talekar, Amol Pandharbale, Mayur Ladole, Shamraja Nadar, Mosin Mulla, Kshitija Japhalekar, Kishori Pattankude, and Devika Arage. Carrier free co-immobilization of alpha amylase, glucoamylase and pullulanase as combined cross-linked enzyme aggregates (combi-cleas): a tri-enzyme biocatalyst with one pot starch hydrolytic activity. *Bioresource technology*, 147:269–275, 2013.

[155] Han Zhang, Shao-Feng Hua, and Lei Zhang. Co-immobilization of cellulase and glucose oxidase on graphene oxide by covalent bonds: a biocatalytic system for one-pot conversion of gluconic acid from carboxymethyl cellulose. *Journal of Chemical Technology & Biotechnology*, 95(4):1116–1125, 2020.

[156] A. Blandino, M. Macías, and D. Cantero. Immobilization of glucose oxidase within calcium alginate gel capsules. *Process Biochemistry*, 36:601–606, 2001. ISSN 13595113. doi: 10.1016/S0032-9592(00)00240-5.

[157] Min-Hua Xue, Qin Xu, Mi Zhou, and Jun-Jie Zhu. In situ immobilization of glucose oxidase in chitosan-gold nanoparticle hybrid film on prussian blue modified electrode for high-sensitivity glucose detection. *Electrochemistry communications*, 8(9):1468–1474, 2006.

[158] Barbara Krajewska, Michal Chudy, Marek Drozdek, and Zbigniew Brzózka. Potentiometric study of urease kinetics over ph 5.36–8.21. *Electroanalysis: An International Journal Devoted to Fundamental and Practical Aspects of Electroanalysis*, 15(5-6):460–466, 2003.

[159] Bao-Yan Wu, Shi-Hua Hou, Feng Yin, Zi-Xia Zhao, Yan-Yan Wang, Xin-Sheng Wang, and Qiang Chen. Amperometric glucose biosensor based on multilayer films via layer-by-layer self-assembly of multi-wall carbon nanotubes, gold nanoparticles and glucose oxidase on the pt electrode. *Biosensors and Bioelectronics*, 22(12):2854–2860, 2007.

Appendices

Appendix A

Potentiometric Titration.

All titrations began at pH 1.0 after addition of a known amount of HCl and were considered complete at pH 12.0. Quantification was done by measuring the equivalence point volumes by differentiating the titration curves and picking the position of the derivative peaks. An uncertainty figure was assigned to each volume based on the width of the corresponding derivative peak. Inflection points were labelled as v_i:

- v_1: neutralization of excess H_3O^+
- v_2: full deprotonation of primary amines on CS
- v_3: deprotonation of unreacted CS amines of CS-QD
- v_4: deprotonation of unreacted CS amines of CS-PEG
- v_5: deprotonation of unreacted CS amines of CS-PEG-QD
- v_6: neutralization of PAMAM amines of CS-PEG-Pa
- v_7: deprotonation of unreacted CS amines of CS-PEG-PAMAM
- v_8: deprotonation of unreacted PAMAM amines of CS-PEG-PAMAM-QD

DS information were gathered from titration experiments by noticing that the following relations hold true for the number of available amines A in the various stages of CS modification:

$$\begin{aligned} A_{\text{CS}} &\propto v_2 - v_1 \\ A_{\text{CS-PEG}} &\propto v_4 - v_1 \\ A_{\text{CS-PEG-PAMAM}} &\propto v_6 - v_4 \end{aligned} \tag{A.1}$$

where $A_{\text{CS:PEG}}$ is a quantity proportional to the unreacted amines after PEG modification. Thus the DS for PEG can be estimated by taking the ratio $(A_{\text{CS}} - A_{\text{CS-PEG}})/A_{\text{CS}} = (v_2 - v_4)/(v_2 - v_1)$ while the DS for PAMAM (with respect to the initial CS amines) is $(A_{\text{CS-PEG-PAMAM}}/3)/A_{\text{CS}} = (v_6 - v_4)/3(v_2 - v_1)$.

Titration data for the molar ratios tested are given in Figure A.1.

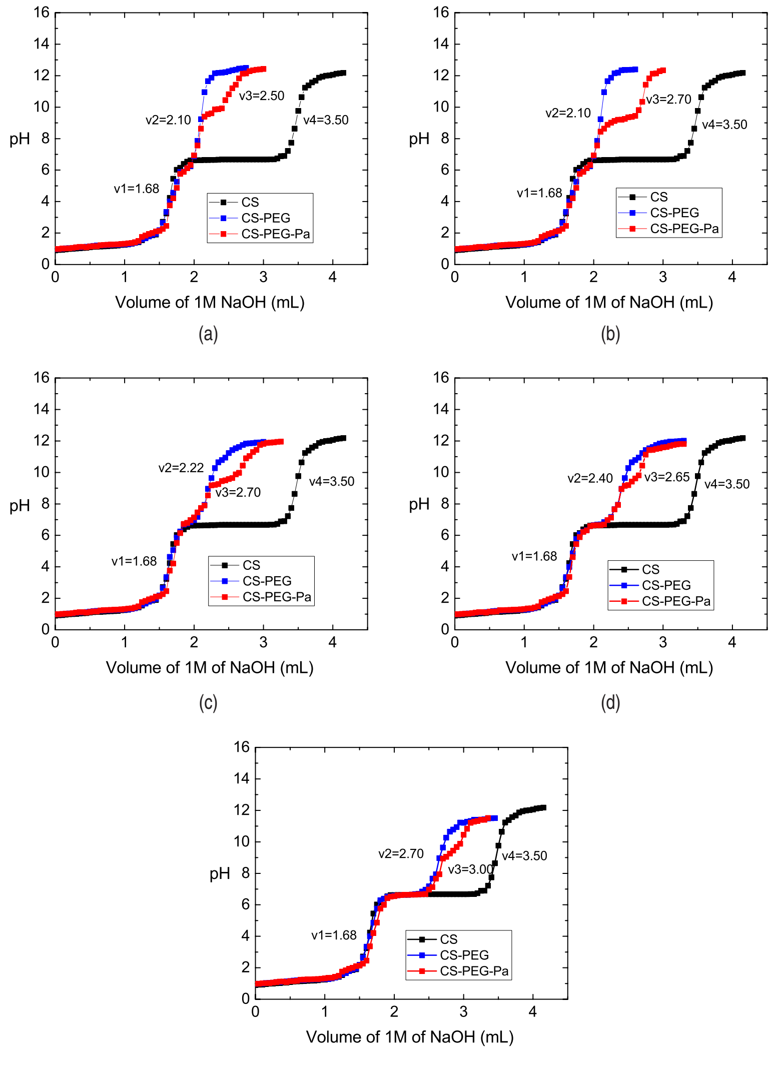

(a) (b) (c) (d) (e)

Figure A.1 – Titration of chitosan (black), CS-PEG (blue) and CS-PEG-Pa (red) with 1 M NaOH. Molar ratios for CS:PEG:Pa were (a) 1:1:1, (b) 1:2:2, (c) 1:1:0.5, (d) 1:1:2 and (e) 1:0.5:0.5, respectively.

Appendix B

NMR spectroscopy.

Coupling efficiencies of PEG and PAMAM were also determined by ^{1}H NMR spectroscopy. Figures B.1-B.5 are representative spectra for Chitosan (CS), and modified CS under the reaction conditions CS-PEG-Pa 1:1:1, CS-PEG-Pa 1:2:2, CS-PEG-Pa 1:1:0.5, CS-PEG-Pa 1:1:2, CS-PEG-Pa 1:0.5:0.5, respectively. Quantification was accomplished by measuring the signal integrals at $\sim$ 1.9 ppm (CS, acetyl-CH_3, 3H), $\sim$ 2.95 ppm (PAMAM, core CH_2, 4H), $\sim$ 4.0 ppm (PEG, α-CH_2, 4H) and using the following equivalencies:

$$\begin{aligned} S_{\mathrm{Deacy}} &= \tfrac{S_{\mathrm{Acy}}}{3}\tfrac{\mathrm{DD}}{1-\mathrm{DD}} \\ \mathrm{DS}_{\mathrm{CS-PEG}} &= \tfrac{1}{S_{\mathrm{Deacy}}}\tfrac{S_{\mathrm{PEG}}}{4} \\ \mathrm{DS}_{\mathrm{CS-PEG-Pa}} &= \tfrac{1}{S_{\mathrm{Deacy}}}\tfrac{S_{\mathrm{Pa}}}{4} \end{aligned} \tag{B.1}$$

where DD is the degree of de-acetylation for chitosan, S_{Acy} is the NMR peak integral corresponding to acetyl-CH_3 in CS, S_{Deacy} is the reference quantity for CS deacetylation obtained by scaling the acetyl-CH_3 peak of chitosan (3 protons). $\mathrm{DS}_{\mathrm{CS-PEG}}$ is the degree of substitution for PEG on CS, S_{PEG} is the NMR peak integral for α-CH_2 protons in PEG (4 protons). $\mathrm{DS}_{\mathrm{CS-PEG-Pa}}$ is the degree of substitution for PAMAM on CS, S_{Pa} is the NMR peak integral for CH_2 protons in PAMAM (4 protons).

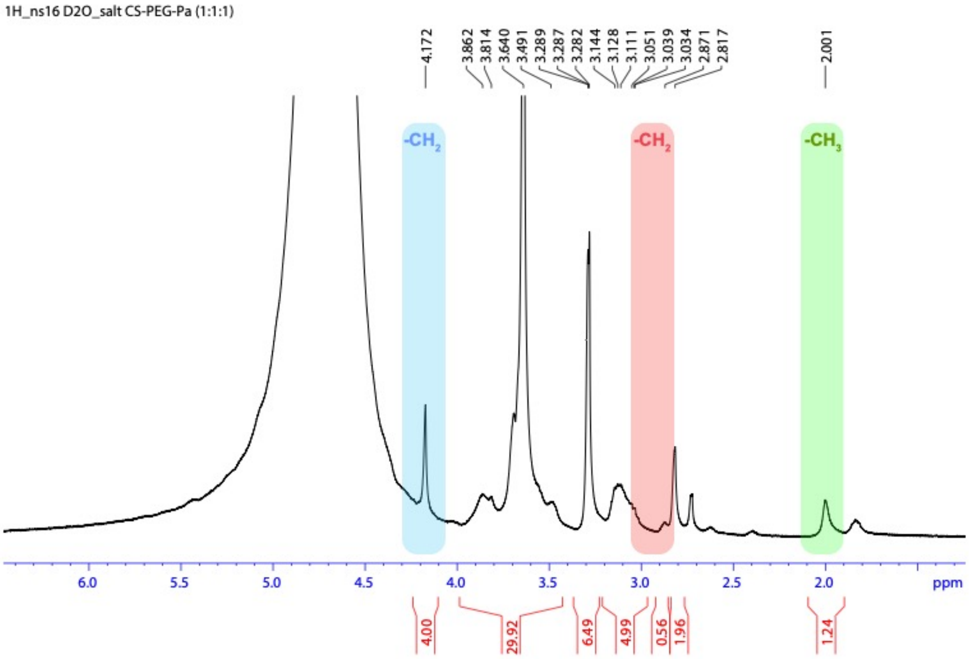

Figure B.1 – ^{1}H NMR spectrum of CS-PEG-PAMAM (molar ratio 1:1:1). The colour scheme is the same as presented in Figure 4.5 of the subsection modification of chitosan in chapter 4.

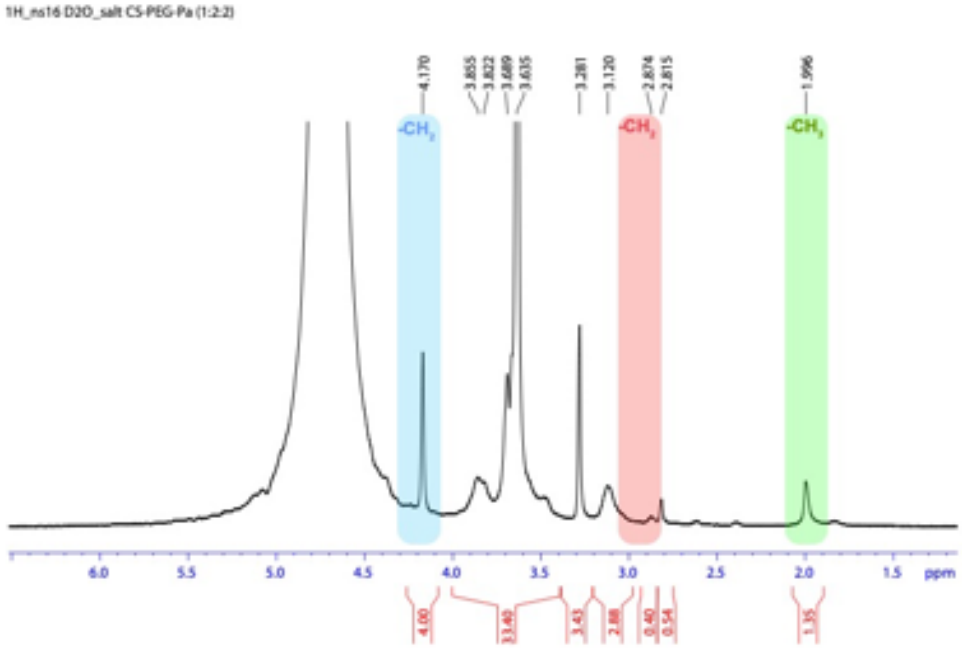

Figure B.2 – ^{1}H NMR spectrum of CS-PEG-PAMAM (molar ratio 1:2:2). The colour scheme is the same as presented in Figure 4.5 of the subsection modification of chitosan in chapter 4.

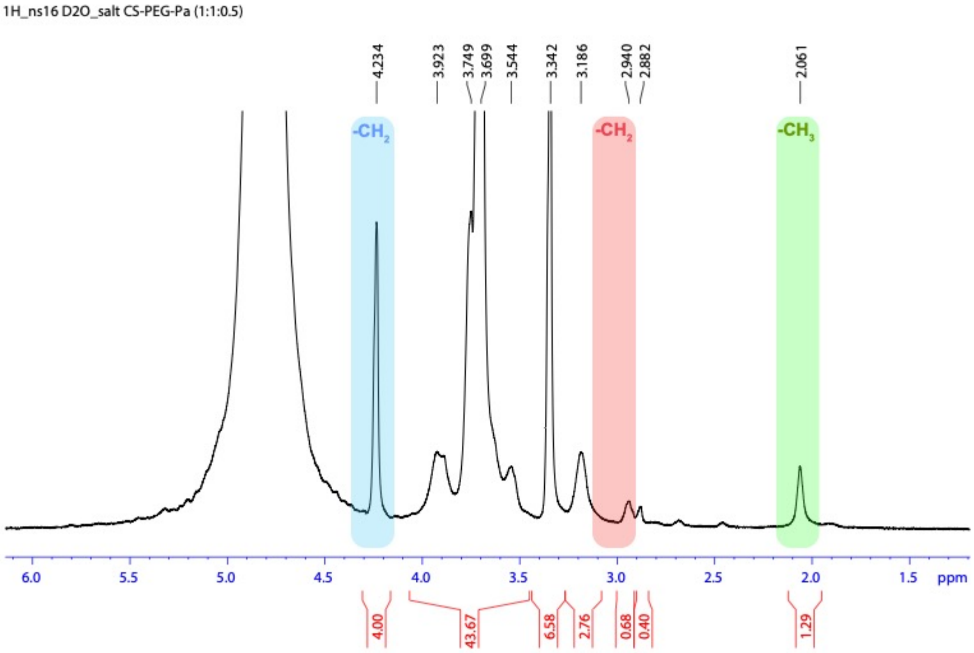

Figure B.3 – ^{1}H NMR spectrum of CS-PEG-PAMAM (molar ratio 1:1:0.5). The colour scheme is the same as presented in Figure 4.5 of the subsection modification of chitosan in chapter 4.

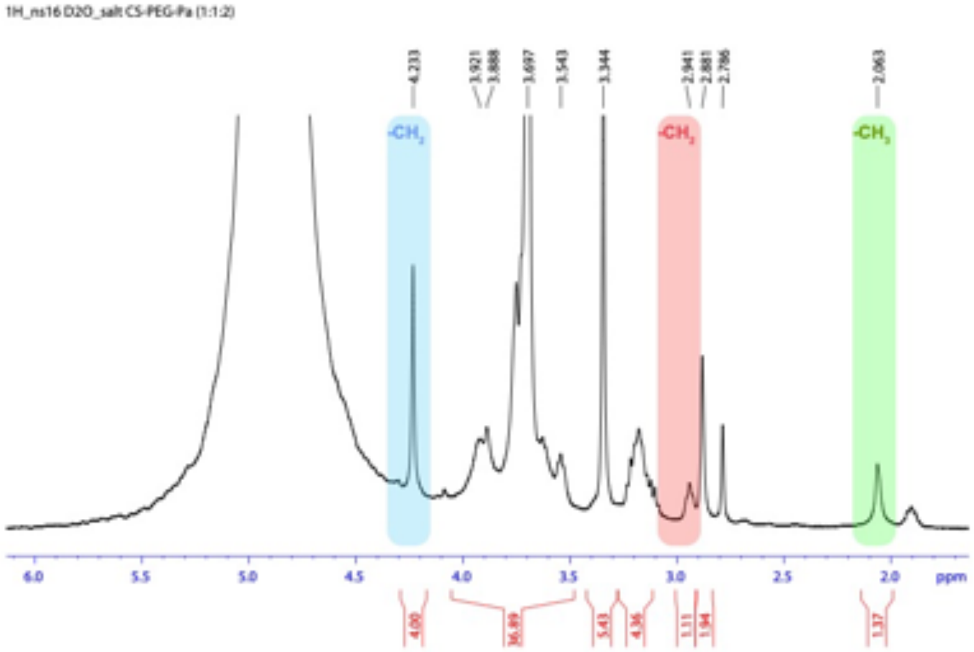

Figure B.4 – ^{1}H NMR spectrum of CS-PEG-PAMAM (molar ratio 1:1:2). The colour scheme is the same as presented in Figure 4.5 of the subsection modification of chitosan in chapter 4.

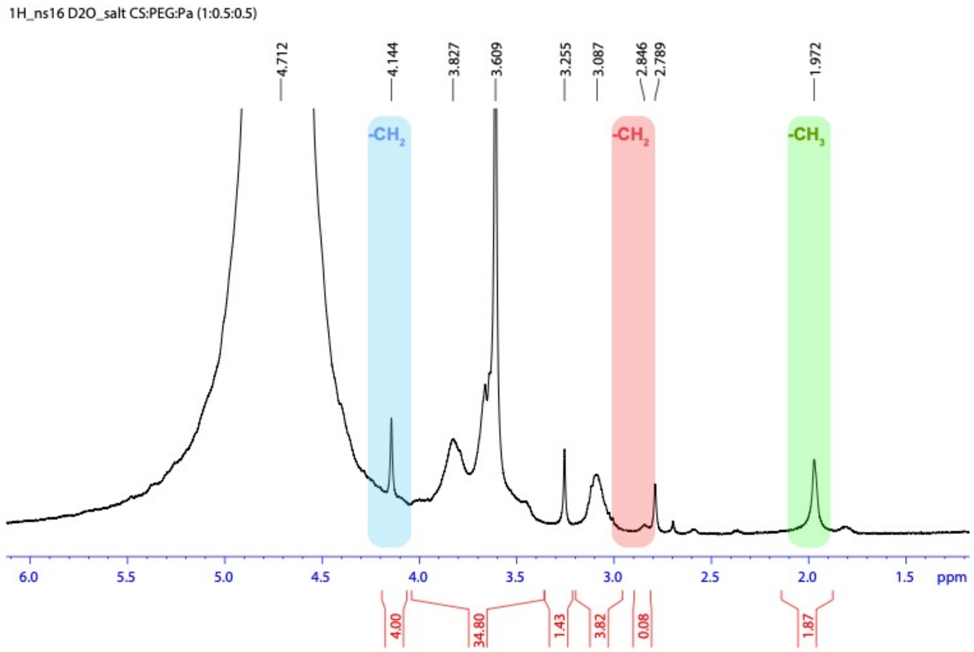

Figure B.5 – ^{1}H NMR spectrum of CS-PEG-PAMAM (molar ratio 1:0.5:0.5). The colour scheme is the same as presented in Figure 4.5 of the subsection modification of chitosan in chapter 4.

Appendix C

Fluorescence spectroscopy & Fluorescence microscopy

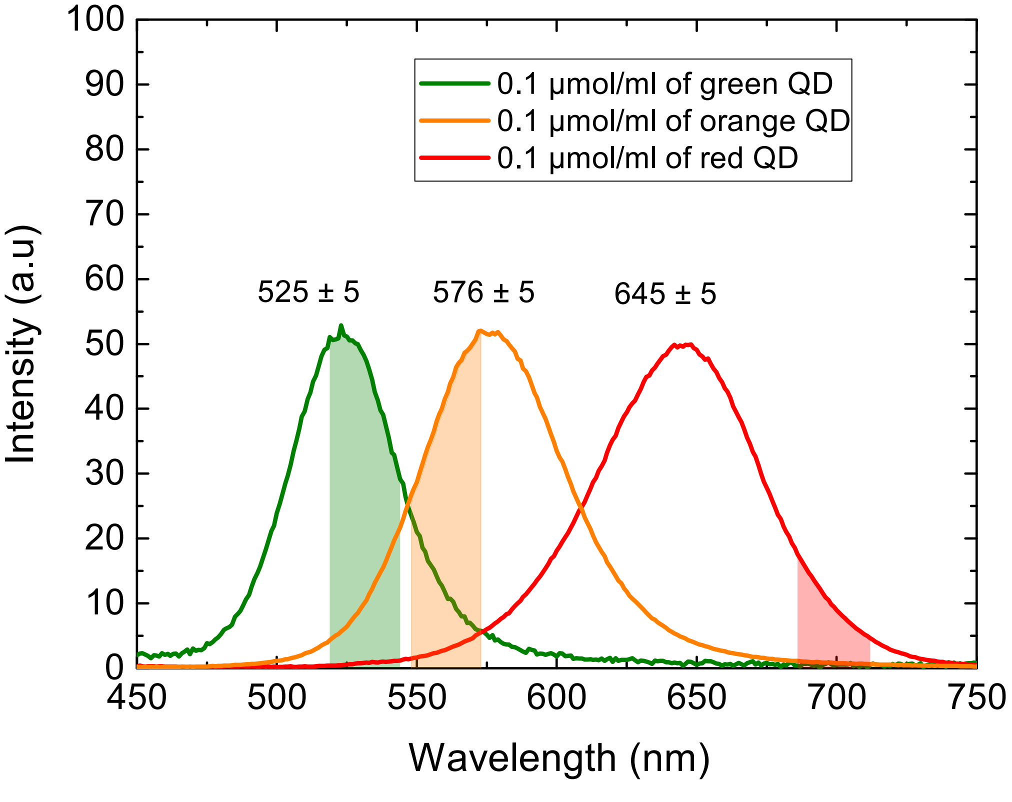

Figure C.1 – Fluorescence emission spectra of QDs at an excitation wavelength of 310 nm; red $\lambda_{emission} = 645\,\text{nm}$, orange $\lambda_{emission} = 576\,\text{nm}$, and green $\lambda_{emission} = 525\,\text{nm}$. The solid filled regions indicated the spectral regions passed by the three transmission band-pass filters used.

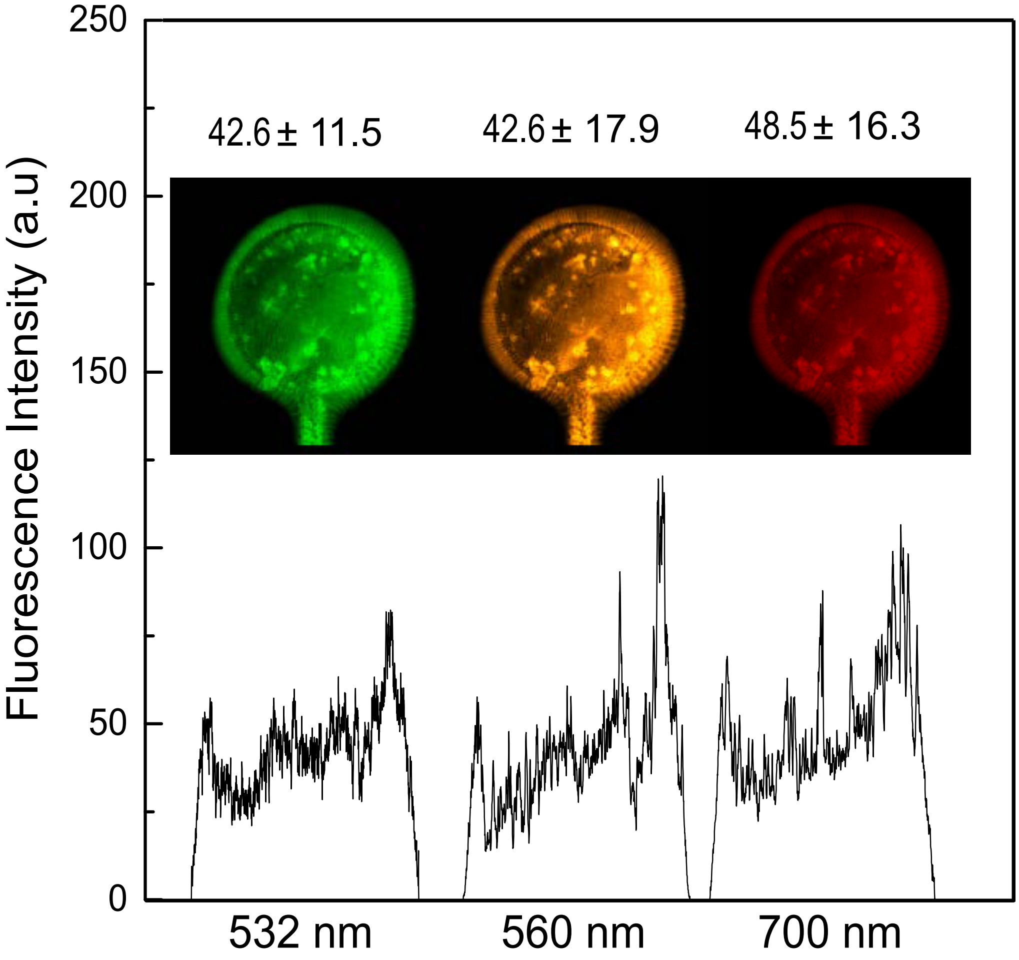

Figure C.2 – Fluorescence emission profiles of multi-layered CS obtained by microscopy. Three layers were assembled, with each layer featuring CS coupled to QDs of different colour. In the presence of transmission band pass filters (green λ =(532 ± 12.5) nm, orange λ =(550 ± 12.5) nm, and red λ =(700 ± 12.5) nm), the different layers can be visualized.

Appendix D

Monitoring in real-time NMR

D.1 Measurement using Bruker's Micro 5

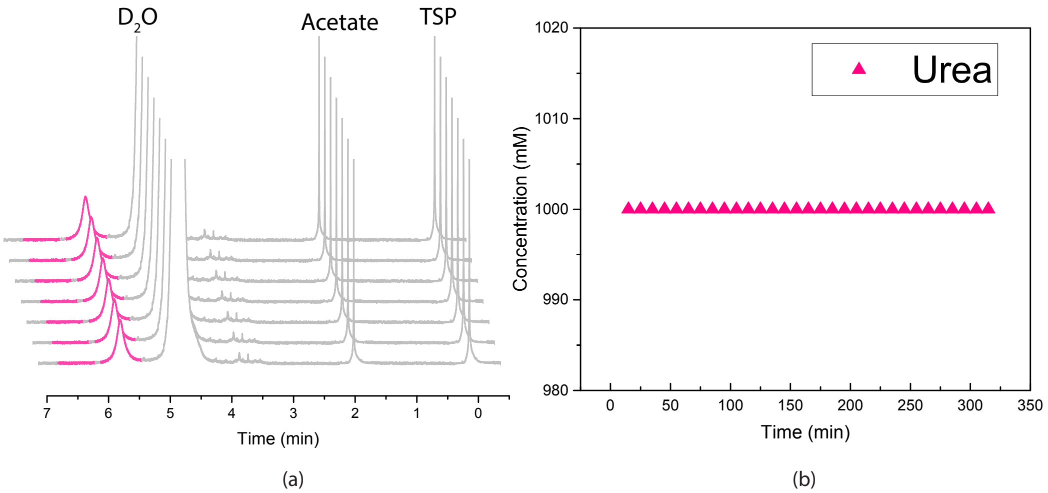

Figure D.1 – ^{1}H NMR spectra of 1000 mM of urea at 5.8 ppm with 50 mM of TSP as a reference.

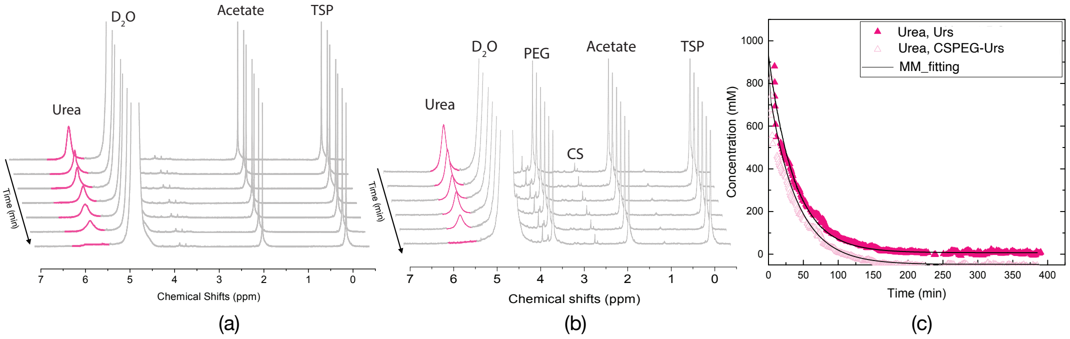

Figure D.2 – ^{1}H NMR spectra of the reaction of urease (a) without; (b) with a polymer with 1000 mM of urea with 50 mM of TSP as a reference and (c) extracted urea concentrations from the NMR results in (a) and (b).

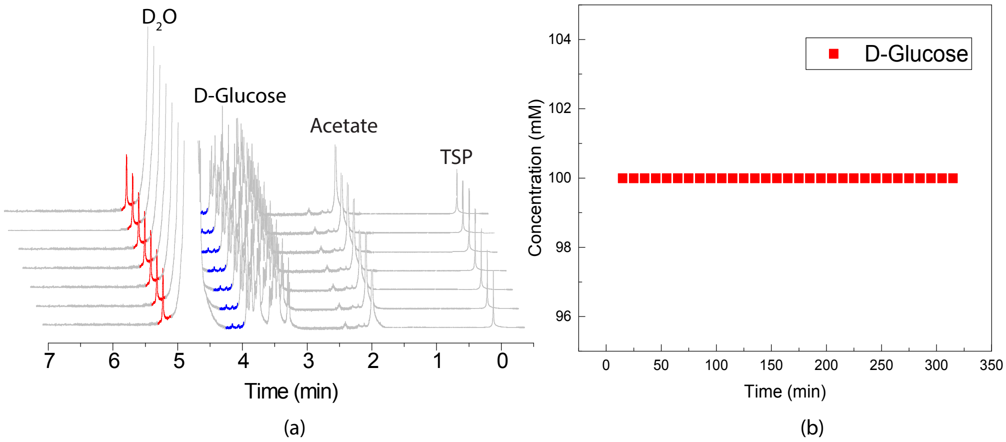

Figure D.3 – ^{1}H NMR spectra of 100 mM of D-Glucose with 50 mM of TSP as a reference.

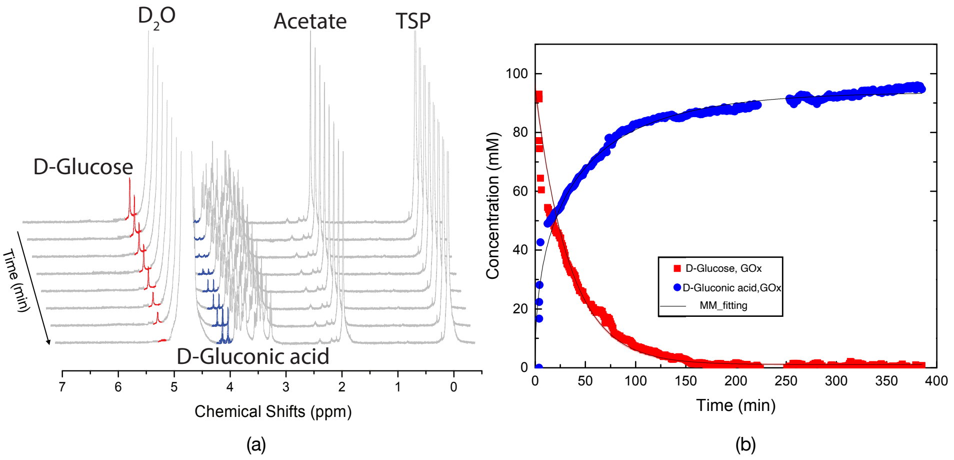

Figure D.4 – (a)^{1}H NMR spectra of the reaction of GOx with 100 mM of D-Glucose with 50 mM of TSP as a reference and (b) extracted D-Glucose (at 5.3 ppm) concentrations and formation of D-Gluconic acid at 4.2 ppm from the NMR results in (a).

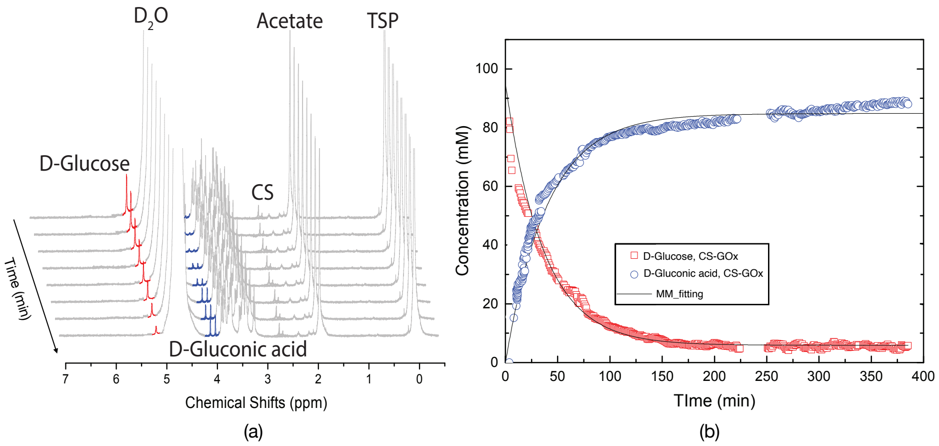

Figure D.5 – (a)^{1}H NMR spectra of the reaction of CSPEG-GOx with 100 mM of D-Glucose with 50 mM of TSP as a reference and (b) extracted D-Glucose (at 5.3 ppm) concentrations and formation of D-Gluconic acid at 4.2 ppm from the NMR results in (a).

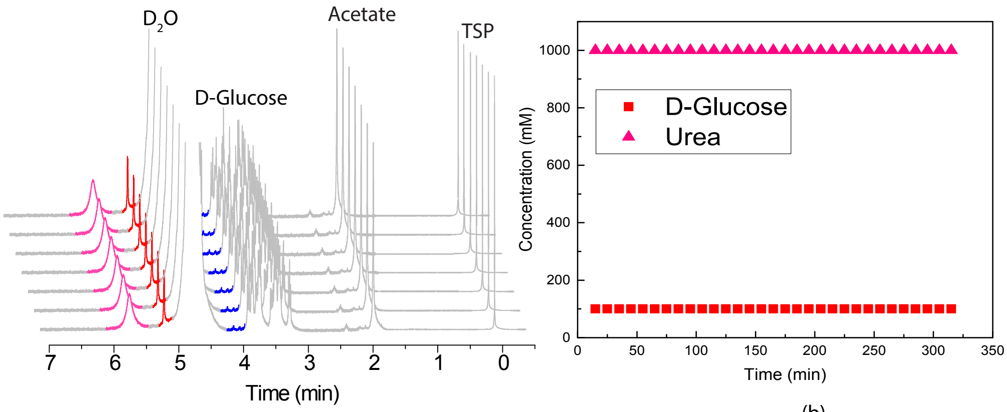

(a) (b)

Figure D.6 – (a) ^{1}H NMR spectra of 100 mM of D-Glucose, 1000 mM of urea with 50 mM of TSP as a reference without enzymes and (b) extracted D-Glucose (at 5.3 ppm) concentrations and Urea at 5.8 ppm from the NMR results in (a).

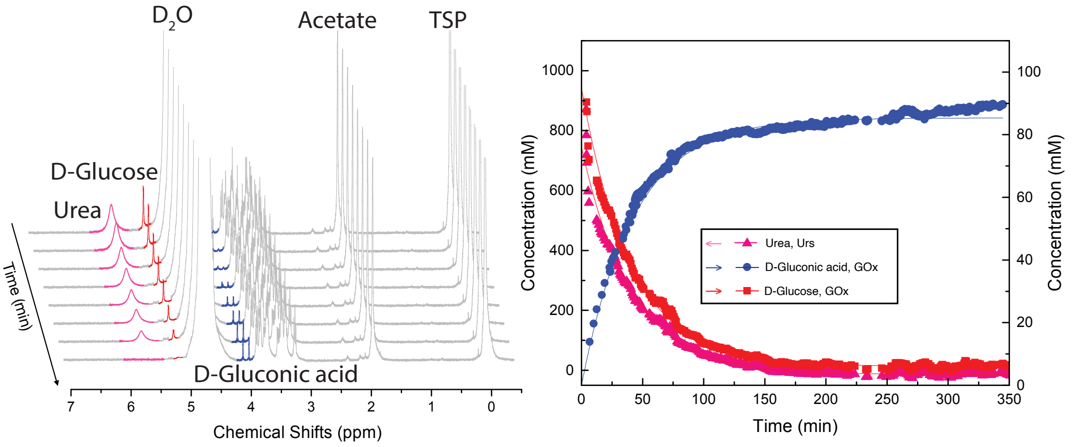

(a) (b)

Figure D.7 – (a) ^{1}H NMR spectra of the reaction of multiplex Urs/GOx with 1000 mM of urea and 100 mM of D-Glucose with 50 mM of TSP as a reference and (c) extracted urea (at 5.8 ppm), D-Glucose (at 5.3 ppm) concentrations and formation of D-Gluconic acid at 4.2 ppm from the NMR results in (a).

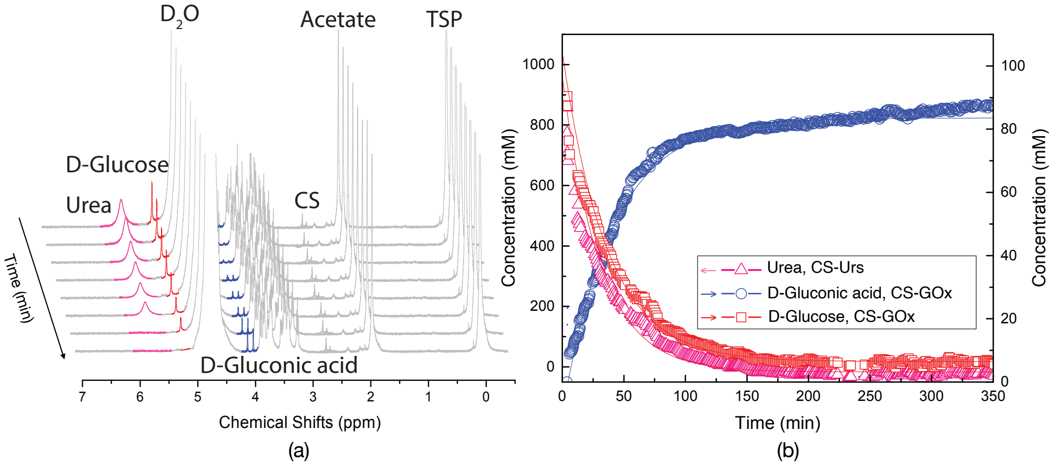

(a) (b)

Figure D.8 – (a) ^{1}H NMR spectra of the reaction of multiplex CSPEG-Urs/CSPEG-GOx with 1000 mM of urea and 100 mM of D-Glucose with 50 mM of TSP as a reference and (c) extracted urea (at 5.8 ppm), D-Glucose (at 5.3 ppm) concentrations and formation of D-Gluconic acid at 4.2 ppm from the NMR results in (a).

D.2 Measurement using a custom Helmholtz coil microdetector, NMR

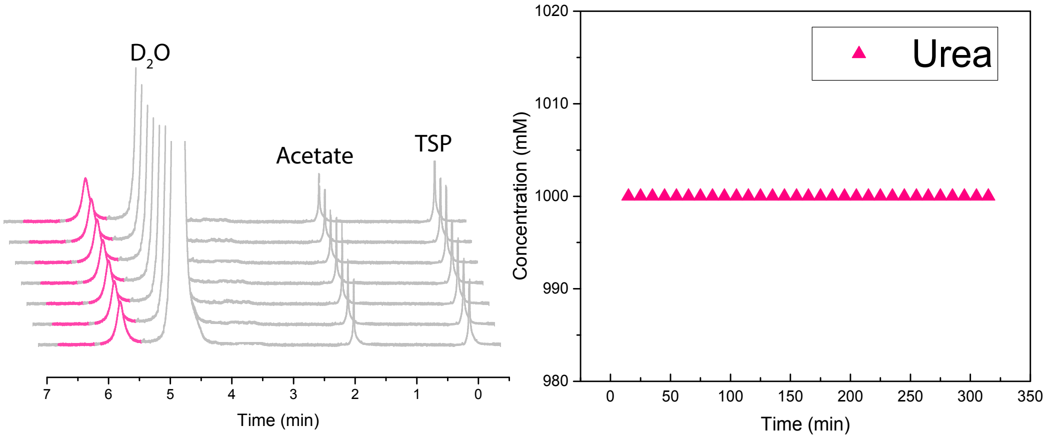

(a)

(b)

Figure D.9 – ^{1}H NMR spectra of 1000 mM of urea with 50 mM of TSP as a reference.

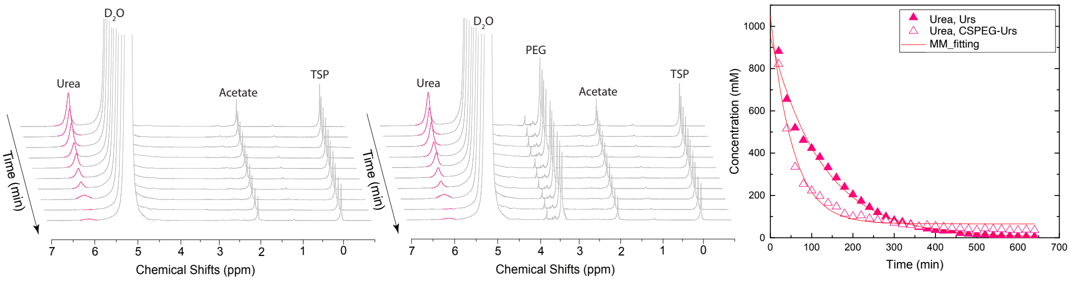

(a)

(b)

(c)

Figure D.10 – ^{1}H NMR spectra of (a) CS; (b) CSPEG-Urs with 1000 mM of urea in a solution with 50 mM of TSP as a reference and (c) extracted NMR results from condition of (a) and (b).

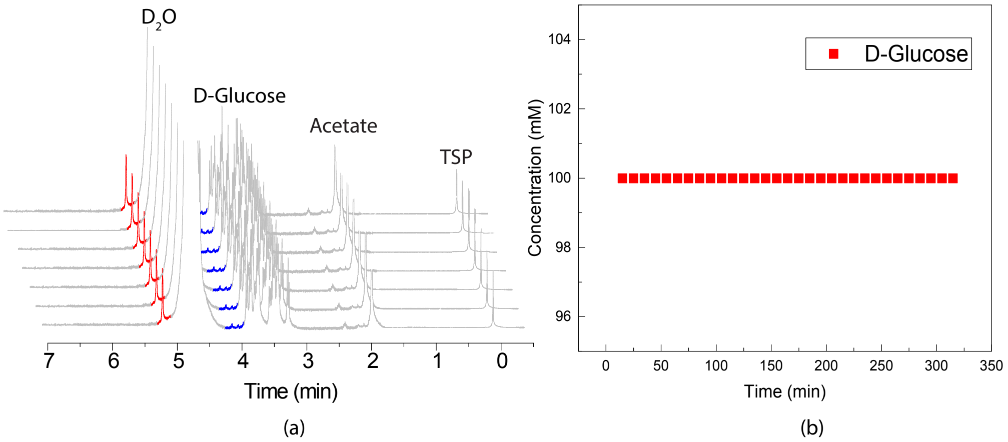

Figure D.11 – ^{1}H NMR spectra of 100 mM of D-Glucose with 50 mM of TSP as a reference.

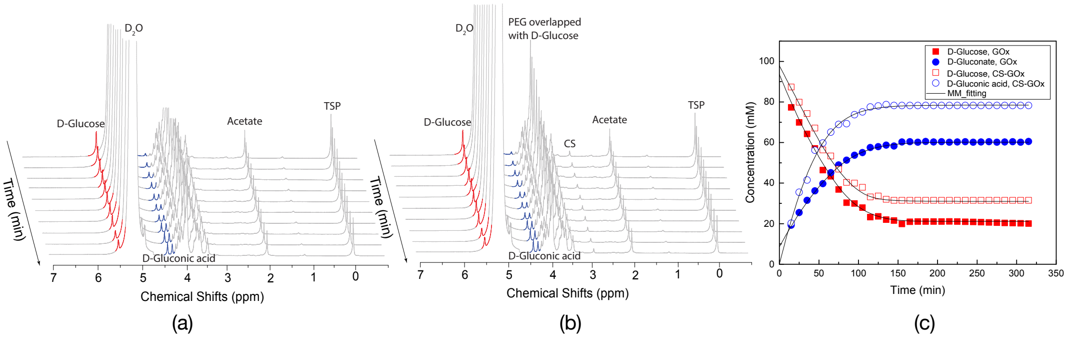

Figure D.12 – ^{1}H NMR spectra of reaction of (a) GOx; (b) CSPEG-GOx with 100 mM of D-Glucose in a solution with 50 mM of TSP as a reference and (c) extracted NMR result from condition of (a) and (b).

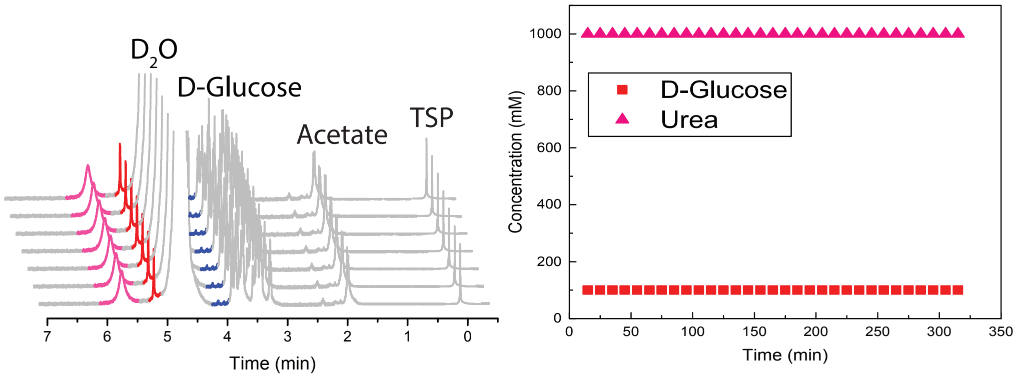

(a) (b)

Figure D.13 – ^{1}H NMR spectra of 1000 mM of urea and 100 mM of D-Glucose with 50 mM of TSP as a reference.

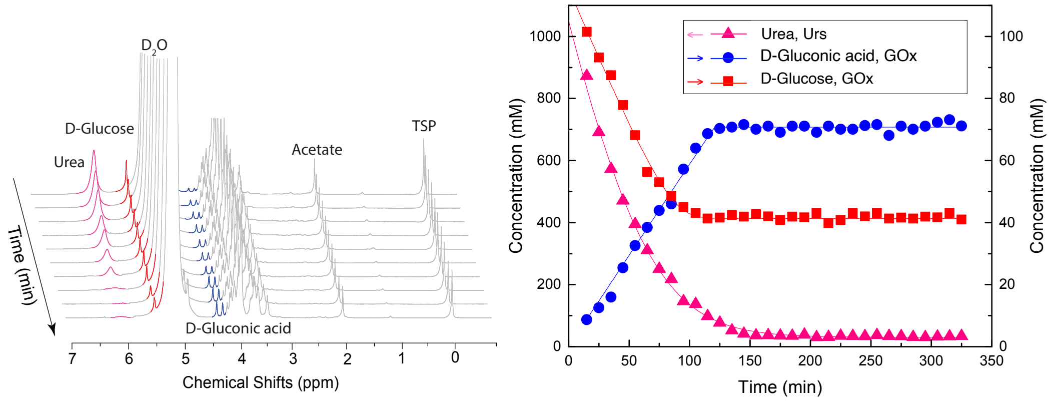

(a) (b)

Figure D.14 – ^{1}H NMR spectra of multiplex enzymes with 100 mM of D-glucose, 1000 mM and 50 mM of TSP as a reference and (c) extracted NMR result from condition of (a) and (b).

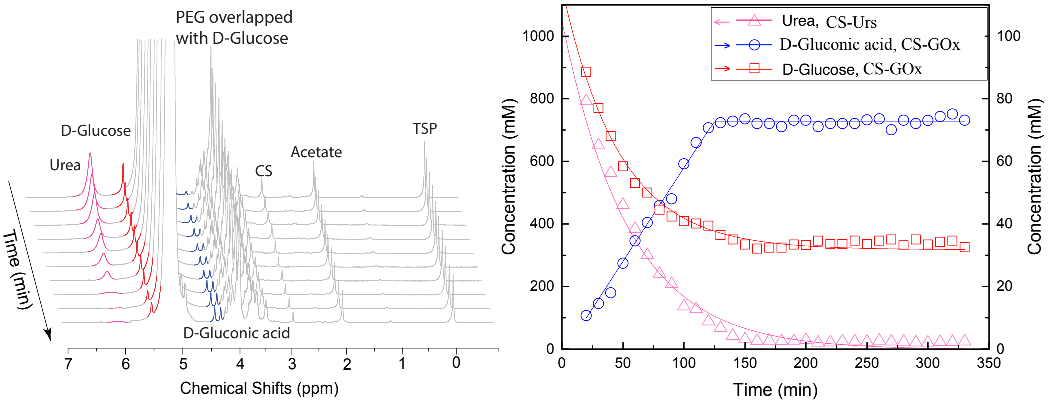

(a) (b)

Figure D.15 – ^{1}H NMR spectra of multiplex enzymes coupled to polymer, CSPEG with 100 mM of D-glucose, 1000 mM and 50 mM of TSP as a reference and (c) extracted NMR result from condition of (a) and (b).

Appendix E

Estimation volume of hydrogels

Figure E.1 shows the estimated volume of each hydrogel layer for the two electrode configurations; (a) planar electrode and (b) sidewall electrode. For the planar electrode (Figure E.1a), thickness was determined for both the Multilayered Assembly and Individual Layer configurations. The thickness of the hydrogel (t_{gel}) was determined using the profile measurement method, performed by removing the upper glass of the channel. The values of t_{gel} are the thicknesses of the individual hydrogel layers (i.e. not the cumulative thickness).

For the sidewall electrode (Figure E.1b), the thickness of the hydrogel layers was estimated by light microscopy. The thickness was measured after preparing the multilayered CS-Urs / CS-Cat / CS-GOx hydrogel assembly, using the same current density and deposition time as in the planar electrode case. The values of t_{gel} are the thicknesses of the individual hydrogel layers (i.e. not the cumulative thickness).

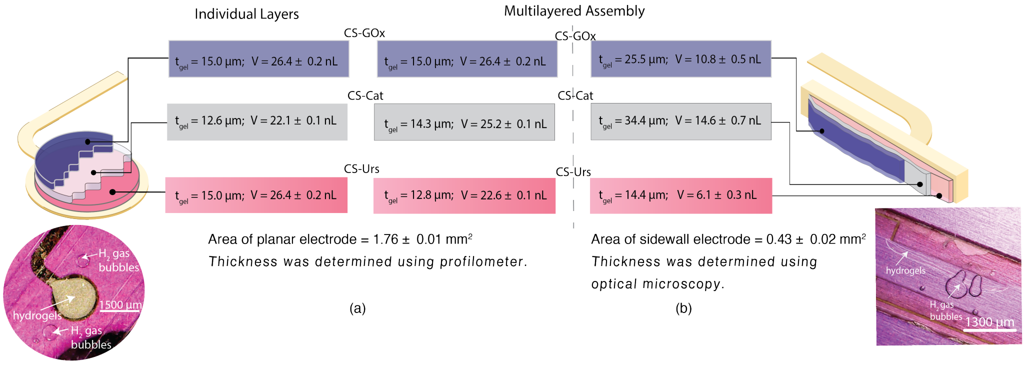
Individual Layers
Multilayered Assembly
CS-GOx
t_{gel} = 15.0 μm; V = 26.4 ± 0.2 nL
t_{gel} = 15.0 μm; V = 26.4 ± 0.2 nL
CS-GOx
t_{gel} = 25.5 μm; V = 10.8 ± 0.5 nL
CS-Cat
t_{gel} = 12.6 μm; V = 22.1 ± 0.1 nL
t_{gel} = 14.3 μm; V = 25.2 ± 0.1 nL
CS-Cat
t_{gel} = 34.4 μm; V = 14.6 ± 0.7 nL
CS-Urs
t_{gel} = 15.0 μm; V = 26.4 ± 0.2 nL
t_{gel} = 12.8 μm; V = 22.6 ± 0.1 nL
CS-Urs
t_{gel} = 14.4 μm; V = 6.1 ± 0.3 nL
Area of planar electrode = 1.76 ± 0.01 mm^2
Thickness was determined using profilometer.
Area of sidewall electrode = 0.43 ± 0.02 mm^2
Thickness was determined using optical microscopy.
(a)
(b)
H_2 gas bubbles
hydrogels
1500 μm
H_2 gas bubbles
hydrogels
H_2 gas bubbles
1300 μm

Figure E.1 – Schematic of the hydrogel layers for individual enzyme deposition and multiplex deposition conditions using (a) planar electrode geometry and (b) sidewall electrode geometry

Publications

- **Nordin, N.**, Bordonali, L., Badilita, V., & MacKinnon, N. Spatial and Temporal Control Over Multilayer Bio-Polymer Film Assembly and Composition. Macromolecular bioscience, 19(4), 1800372 (2019)

- **Nordin, N.**, Bordonali, L., Korvink, J. G., Badilita, V., & MacKinnon, N. Towards 3D Compositional Control of Addressable Bio functional Sites Within a Microfluidic Environment. Proceedings of Miniaturized Systems for Chemistry and Life Sciences, (MicroTAS), pp. 1358 (2017)

- **Nordin, N.**, Bordonali, L., Korvink, J. G., Badilita, V., & MacKinnon, N. Monitoring in-situ electrodeposition of chitosan in a compact microfluidic channel with NMR Spectroscopy. Proceedings of Miniaturized Systems for Chemistry and Life Sciences, (MicroTAS), pp. 2160 (2018).

- Bordonali, L.,**Nordin, N.**, Führer, E., MacKinnon, N., & Korvink, J. G. Parahydrogen based NMR hyperpolarisation goes micro: an alveolus for small molecule chemosensing. Lab on a Chip, 19(3), 503-512 (2019)

- Mamleyev, E. R., Stefan H., Alexei N., Peter G. W., **Nordin, N.**, Vladislav V. K., Länge K., MacKinnon N., & Sharma S. Laser-induced hierarchical carbon patterns on polyimide substrates for flexible urea sensors. npj Flexible Electronics, 3(1), 2 (2019)

- Mamleyev, E. R., **Nordin, N.**, Heissler, S., Länge, K., MacKinnon, N., & Sharma, S. Flexible Carbon-based Urea Sensor by Laser Induced Carbonisation of Polyimide. Proceedings in 2018 International Flexible Electronics Technology Conference (IFETC), pp. 1. IEEE (2018).

- Davoodi, H., **Nordin, N.**, Bordonali, L., Korvink, J. G., MacKinnon, N. & Badilita, V. An enabling technology for a simple electrochemistry featuring NMR spectroscopy. Lab on a Chip(2020) (*Published*)

- **Nordin, N.**, Bordonali, L.,Davoodi, H., Korvink, J. G., Badilita, V., & MacKinnon, N. Multiplexed sensing of metabolic activity in a customizable compositional microfluidic platform.(*in preparation*)

- Davoodi, H., **Nordin, N.**, Munakata, H., Korvink, J. G., MacKinnon, N., & Badilita, V. Untuned broadband spiral micro-coils achievesensitive multi-nuclear NMR TX/TR from microfluidicsamples.(*in preparation*)

Conferences

- **Nordin, N.**, Bordonali, L., Korvink, J. G., Badilita, V., & MacKinnon, N. Towards 3D Compositional Control of Addressable Bio functional Sites Within a Microfluidic Environment. The Twenty First International Conference on Miniaturized Systems for Chemistry and Life Sciences, (MicroTAS), Savannah, Georgia, US. (October, 22nd-26th 2017)

- **Nordin, N.**, Bordonali, L., Korvink, J. G., Badilita, V., & MacKinnon, N. Monitoring in-situ electrodeposition of chitosan in a compact microfluidic channel with NMR Spectroscopy. The Twenty Second International Conference on Miniaturized Systems for Chemistry and Life Sciences, (MicroTAS), Kaohsiung, Taiwan (November, 11th-15th 2018).

- **Nordin, N.**, Bordonali, L., Korvink, J. G., Badilita, V., & MacKinnon, N. Microcoil NMR to Monitor in-situ Electrodeposition of Chitosan in a Microfluidic Platform with Integrated Electrodes. Experimental Nuclear Magnetic Resonance, California, US (April, 7th-12th 2019)

- Mamleyev, E. R., **Nordin, N.**, Heissler, S., Länge, K., MacKinnon, N., & Sharma, S. Flexible Carbon-based Urea Sensor by Laser Induced Carbonisation of Polyimide. International Flexible Electronics Technology Conference (IFETC), Ottawa, Ontario Canada (August, 7h-9th 2018).

- Bordonali, L., **Nordin, N.**, Führer, E., MacKinnon, N., & Korvink, J. G. Parahydrogen based NMR hyperpolarisation goes micro: an alveolus for small molecule chemosensing. Experimental Nuclear Magnetic Resonance, California, US (April, 7th-12th 2019)

Activities

- **Nordin, N.**, Bordonali, L., Korvink, J. G., Badilita, V., & MacKinnon, N. Developmemt of a microfluidic platform with integrated microdetector for NMR analysis of biological samples. 15th International School of Biological Magnetic Resonance at Ettore Majorana Centre, Erice, Sicily (Italy),
  May 19th – 28th 2017 (Oral presentation)

- **Nordin, N.**, Bordonali, L., Korvink, J. G., Badilita, V., & MacKinnon, N. 3D compositional control of addressable biofunctional sites within a microfluidic channel featuring NMR spectroscopy. BioInterfaces International Graduate School (BIF-IGS), 2017, Hotel Rappen, Rothenburg ob der Tauber (Germany).
  June 12th-14th 2018 (poster presentation)

- **Nordin, N.**, Bordonali, L., Korvink, J. G., Badilita, V., & MacKinnon, N. Developmemt of a microfluidic platform with integrated microdetector for NMR analysis of biological samples. Kyoto Winter School 2019 "Quantifying Dynamics of Life", Center for Integrative Medicine and Physics, Institute for Advance Study, Kyoto University (Japan),
  March 11th-20th 2019 (Oral and poster presentation)

- **Nordin, N.**, Bordonali, L., Korvink, J. G., Badilita, V., & MacKinnon, N. 3D compositional control of addressable biofunctional sites within a microfluidic channel featuring NMR spectroscopy. BioInterfaces International Graduate School (BIF-IGS), 2017, Hotel Deutscher Hof, Trier (Germany).
  June 11th-13th 2019 (oral presentation)

Acknowledgments

بسم الله الرحمن الرحيم

In the name of God, most Gracious, most Compassionate

Alhamdulillah, all praises to the Almighty that give me an opportunity to embark on my PhD and for completing this long and challenging journey successfully.

My gratitude and thanks go to my supervisor **Dr. Neil MacKinnon** for the knowledge, fruitful discussion, motivation and support during my PhD journey. I am nothing without your guidance and I am grateful that he is an understanding supervisor and never get tired to correct my mistakes. Even though, your schedule is always tight, but you still consider to spent some time to have a retreat together and playing badminton together. I have picked my favourite line, “a good teacher is like a candle, it consumes itself to provide others” and you are not just a SV to me but a teacher too.

Also, to my co-supervisor, **Dr. Vlad Badilita**. Thank you for the support, patience and ideas in assisting me with this project. Thank you for being friendly to me and spending your time playing badminton with me. My favourite line for you is: “A good teacher is merely a catalyst”, and you are a “catalyst” to encourage me to speed it up in writing.

Many thanks also to **Prof. Korvink** and **Prof. Andreas Guber** for their support and fruitful discussions during the monthly and TAC meeting. Thank you for always encouraging me in a motivational way.

The manufacturing process for the micro fabrication of electrode arrays and planar electrodes inside microfluidic channel compatible with NMR was carried out in collaboration with **Dr. Lorenzo Bordonali**. We worked together in a clean room to produce microfluidic chips. All processes were demonstrated by him, and then I replicate the experiment according to the same protocol, except for the part for which I have no authority to do it myself, such as the exposure and bonding processes. In the meantime, the micro fabrication of the sidewall electrode has been done by **Hossein Davoodi**, one of the Bio-Price collaborators. Protocol on the manufacturing process for sidewalls electrode microfluidic channel was described by him in one of our joint journal article collaborations.

My deepest appreciation goes to my best partner, my best friend, my mentor and my supporter, **Dr. Lorenzo Bordonali**. You are my true “abang”. Whenever my day rises or falls, you are there to cheer me up, motivate me and always be a good listener. Thank you for being a "consoler" to relieve my stress. Thank you for being my math teacher. Thank you for being my "breakfast, coffee and lunch buddy". These Malay words suit you well: *bersama sentiasa seperti belangkas.* Our common line: *When the moon hits my eyes and the pie hits your eyes, that's ...* (you know it!).

A 'pantun' for you:

Berbaju merah si anak teruna,
lagak dan gaya seorang lelaki,
Terima kasih untuk semua,
InshaAllah, ada rezeki jumpa lagi.

Special thanks to my officemates, **Hossein Davoodi, Shyam Adhikari, Mohammad Abdo and Albina Julius** for helping me with this journey. Being with all of you has always brightened my day. The laughter, the fights and the sad part were the best experience I will remember.

Many thanks also to my master student, **Novindi Dwi Ratnawati** for your help in preparing the samples. Thank you for your support, your delicious and spicy foods and your laughter, which always cheers me up when I feel down.

I also would like to express my gratitude to the staff of the Institute of Microstructure of Technology (IMT), especially **Ms. Nina Giraud, Mr. Roth, Mr. Matthias Gramlich, Mr. Heckele Mattias, Mr. Benz, Dr. Markus Guttman, Dr. Kerstin Länge, Mr. Dinglereiter, Mr. and Mrs. Klein, and Mr Frisman Terrero** for providing the facilities, software and assistance.

To my lovely brothers (**Ahmad, Azaam, Amran, Anuar and Azizi**), my sister-in-laws (**Halina, Faridah, Noorazlina, Maizan and Linda**), my nephews (**Aiman, Afwan, Hariz, Afnan, Azaim, Amnan, Akmal, Azfar, Hadif, Amzar, Arman, Rayyan**), my nieces (**Adlina, Kaisah, Alisha, Faqiha, Arina, Damia, Dhiya, Afrina, Dynas, Amani, Hana, Annur, Naura**) and my best friend, **Huda Salah Kareem** who always support me and encourage me to return with a piece of victory. Your spirits are with me always.

Finally, this thesis is dedicated to the loving memory of my very dear late father, **Nordin B. Mohd Saat** and also to my lovely mother, **Maimon Haji Mahmood** for the vision, the prayer and determination to educate me. Without your blessing I might not have been able to achieve this little piece of knowledge. This piece of victory is dedicated to both of you. Alhamdulillah.